

BOSTON UNIV MA DEPT OF ASTRONOMY  
RADIO STUDIES OF CORONAL HOLES. (U)  
MAR 81 M D PAPAGIANNIS, K B BAKER

F/G 3/2

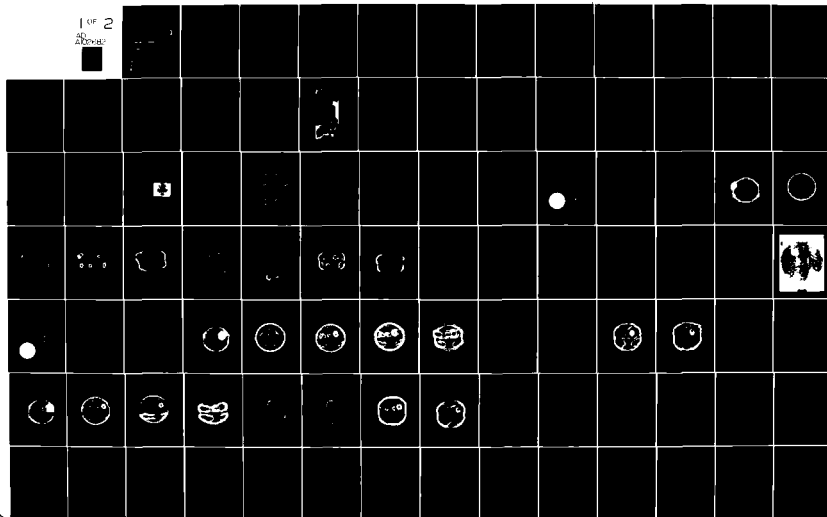
F19628-77-C-0189

UNCLASSIFIED

AFGL-TR-81-0053

NL

1 OF 2



AD A102682

18 AFGL TR-81-0053

LEVEL

7

6 RADIO STUDIES OF CORONAL HOLES.

10 Michael D./Papagiannis  
Kile B./Baker

Department of Astronomy  
Boston University  
725 Commonwealth Avenue  
Boston, Massachusetts 02215

DTIC  
ELECTE  
AUG 11 1981

C

9 FINAL REPORT. 1 Jul 77 -  
34 Sep 1980

11 Mar 1981

12 139

Approved for public release; distribution unlimited

15 F19628-77-C-0189

16 2311

AIR FORCE GEOPHYSICS LABORATORY  
AIR FORCE SYSTEMS COMMAND  
UNITED STATES AIR FORCE  
HANSCOM AFB, MASSACHUSETTS 01731

17 G3BB

FILE COPY

81 8 10 039  
406311

Qualified requestors may obtain additional copies from the Defense Technical Information Center. All others should apply to the National Technical Information Service.

UNCLASSIFIED

SECURITY CLASSIFICATION OF THIS PAGE (When Data Entered)

REPORT DOCUMENTATION PAGE		READ INSTRUCTIONS BEFORE COMPLETING FORM
1. REPORT NUMBER AFGL-TR-81-0053	2. GOVT ACCESSION NO. AD-A102682	3. RECIPIENT'S CATALOG NUMBER
4. TITLE (and Subtitle)  Radio Studies of Coronal Holes		5. TYPE OF REPORT & PERIOD COVERED Scientific Final 1 July 1977 - 30 Sept. 1980
		6. PERFORMING ORG. REPORT NUMBER
7. AUTHOR(s) Michael D. Papagiannis Kile B. Baker		8. CONTRACT OR GRANT NUMBER(s)  F-19628-77-C-0189
9. PERFORMING ORGANIZATION NAME AND ADDRESS Department of Astronomy Boston University 725 Commonwealth Ave., Boston, MA 02215		10. PROGRAM ELEMENT, PROJECT, TASK AREA & WORK UNIT NUMBERS  2311G3BB
11. CONTROLLING OFFICE NAME AND ADDRESS Air Force Geophysics Laboratory Hanscom AFB, MA 01731 Contract Monitor: Donald Guidice/PHP		12. REPORT DATE March 1981
		13. NUMBER OF PAGES 138
14. MONITORING AGENCY NAME & ADDRESS (if different from Controlling Office)		15. SECURITY CLASS. (of this report)  Unclassified
		15a. DECLASSIFICATION/DOWNGRADING SCHEDULE
16. DISTRIBUTION STATEMENT (of this Report)  Approved for public release; distribution unlimited.		
17. DISTRIBUTION STATEMENT (of the abstract entered in Block 20, if different from Report)		
18. SUPPLEMENTARY NOTES		
19. KEY WORDS (Continue on reverse side if necessary and identify by block number) Coronal Holes                      Solar Atmosphere Models Solar Radio Maps                  Solar Wind Streams Radio Spectra                      Interplanetary Scintillation		
20. ABSTRACT (Continue on reverse side if necessary and identify by block number) This final report describes all the projects undertaken during the entire period of the above contract, the scope of which was to study coronal holes at radio wavelengths. Chapters 1, 2 and 3 summarize work that has already been described in our previous scientific reports and published papers. Chapters 4 and 5 are comprehensive descriptions of the more recent work that has not been previously published. Chapter 1 describes the determination of the radio spectrum (relative changes in the brightness temperatures at different radio wavelengths) of Coronal Hole 1		

DD FORM 1 JAN 73 1473 EDITION OF 1 NOV 65 IS OBSOLETE

UNCLASSIFIED

SECURITY CLASSIFICATION OF THIS PAGE (When Data Entered)

SECURITY CLASSIFICATION OF THIS PAGE (When Data Entered)

Chapter 2 summarizes our efforts to identify individual high latitude coronal holes with high speed solar wind streams far above or below the ecliptic. The coronal holes were identified from the Kitt Peak 10830 Å synoptic maps, while the high speed solar wind streams were identified from the interplanetary scintillation measurements made at UCSD and at the Toyokawa Observatory in Japan.

Chapter 4 describes the international effort we organized in the summer of 1978 to obtain solar radio maps over a wide range of wavelengths. These radio maps were made on the same days at a number of radio observatories around the world. During the first observing period, July 6-10, 1978 there were no coronal holes present. During the second period, July 15-18, 1978, there were two sizable coronal holes, one in the northern hemisphere and the other in the southern hemisphere. Unfortunately there were also several active regions, which made it difficult to establish the quiet sun level and introduced some uncertainty in the radio spectra obtained for these two coronal holes.

The results of this analysis indicate that inside coronal holes the following changes occur: The chromosphere expands in height by about a factor of 2, while the temperatures and electron and neutral particle densities decrease to about 80% of their quiet sun values. The critical transition zone expands by a factor of about 5-6, while the temperatures decrease to about 50% and the electron densities to about 20% of their quiet sun values. Finally, the corona shows no substantial expansion, but the temperatures and electron densities decrease to about 80% of their quiet sun values.

Accession For	
NTIS GRA&I	<input checked="" type="checkbox"/>
DTIC TAB	<input type="checkbox"/>
Unannounced	<input type="checkbox"/>
Justification	
By	
Distribution/	
Availability Codes	
Avail and/or	
Special	
A	

SECURITY CLASSIFICATION OF THIS PAGE(When Data Entered)

TABLE OF CONTENTS

DD 1473 FORM (including ABSTRACT).....	1
INTRODUCTION.....	5
PUBLICATIONS.....	8
CHAPTER 1. Radio Observations of Coronal Holes From the Skylab Period.....	11
1.1 The Radio Spectrum of Coronal Hole 1.....	11
1.2 Identification of Coronal Holes on the Stanford 9.1 cm Synoptic Charts.....	14
CHAPTER 2. High Latitude Coronal Holes and Their Correlation to High Latitude Interplanetary Scintillation.....	18
2.1 The Correlation of IPS and Coronal Hole Data.....	18
CHAPTER 3. Observations of Coronal Holes at Arecibo and Haystack in September of 1977.....	25
3.1 Coronal Hole Observations at 11.5 and 21 cm with the Arecibo Radio Telescope in 1977.....	25
3.2 Coronal Hole Observations at Haystack and La Posta in 1977.....	28
3.3 The Radio Spectrum of the September 1977 Coronal Hole..	28
CHAPTER 4. Coronal Hole Radio Observations during July 1978.....	31
4.1 International Effort.....	31
4.2 First Period Observations.....	32
4.3 Second Period Observations.....	49
4.4 The Spectra of the Second Period Coronal Holes.....	79
CHAPTER 5. Spectra and Coronal Hole Models.....	89
5.1 The Spectra of Coronal Holes.....	89
5.2 Modeling Procedures.....	90
5.3 Modeling Results.....	98
5.4 Conclusions.....	119

ACKNOWLEDGEMENTS.....	120
REFERENCES.....	122
APPENDIX I. Standard Solar Atmosphere Model.....	125
APPENDIX II. Ray Tracing Program.....	127

## INTRODUCTION

### 1. Scientific Objectives

The purpose of this contract was to study coronal holes at radio wavelengths and to use these radio observations to:

- 1) Identify coronal holes in solar radio maps at different wavelengths,
- 2) model the structure of a coronal hole,
- 3) compare different coronal holes in order to see if there were observable differences at radio wavelengths, and
- 4) correlate the coronal hole observations with high speed solar wind streams.

The structure of coronal holes is still not well understood. Efforts to model coronal holes have been made by several authors (Withbroe and Wang, 1972; Mariska, 1978; Mariska and Withbroe, 1978) using EUV data. In addition, Chiuderi-Drago (Chiuderi-Drago, et al., 1977; Chiuderi-Drago and Poletto, 1977; Chiuderi-Drago, 1980) has made several attempts to model coronal holes based on radio observations. Finally, Dulk and his co-workers (Dulk, et al., 1977) have attempted to match the models deduced from EUV and radio data. Unfortunately, the models derived from EUV data are in substantial disagreement with those derived from radio data. It is important to resolve these differences and much of our work has been aimed toward this problem.

A clear understanding of the transition zone is of great importance to our understanding of the coronal hole phenomenon. As Withbroe (1978) has pointed out, "The



transport of energy by thermal conduction into the transition zone is a primary coronal cooling mechanism." Thus, the temperature and particle density gradients in the transition zone are of critical importance in understanding the energy balance of a coronal hole.

The link between large equatorial coronal holes and high speed solar wind streams observed at the earth has been well established (Newpert and Pizzo, 1976; Nolte et al., 1976, 1978; Broussard, et al., 1978). Smaller coronal holes and coronal holes at high solar latitudes have also been related to high speed solar wind streams (Coles and Rickett, 1976; Rickett, et al. 1976; Sime and Rickett, 1973; Baker and Papagiannis, 1980), although the correlation is less clear for these cases. A qualitative understanding of the relationship between a coronal hole and high speed wind streams emanating from the coronal hole has been provided by Kopp and Orrall (1977), but a quantitative understanding requires a detailed knowledge of the energy balance in the coronal hole. Thus we are again brought back to the conclusion that consistent models of coronal holes are required to complete our understanding of the solar wind streams.

This final report provides a complete summary of our work on coronal holes, using radio observations as well as interplanetary scintillation and coronal hole maps made from EUV data, X-Ray data, and the Helium 10830 Å spectroheliograms made at Kitt Peak. Chapter 1 describes the identification of coronal holes on the synoptic solar radio

maps made for other purposes at Stanford during the Skylab period in 1973, as well as the determination of a coronal hole radio spectrum from different observations made during the same period. Chapter 2 describes the work we have done on the correlation between high latitude coronal holes and high speed solar wind streams observed far above or below the ecliptic by interplanetary scintillation measurements.

Chapter 3 is devoted to our observations made at the Haystack Radio Observatory and at the Arecibo Radio Observatory during 1977. The work described in Chapters 1 - 3 has been described in detail in our three previous Scientific Reports (AFGL-TR-77-0292, AFGL-TR-78-0284, AFGL-TR-80-0123).

Chapter 4 is devoted to the presentation and analysis of the solar radio maps made during the month of July, 1978. These maps were made as part of an international co-operative effort organized by us to provide solar maps over a wide range of radio wavelengths. Finally, Chapter 5 describes the modeling process we have used in analyzing the radio spectra we have obtained. This modeling process provides us with a vertical profile of temperature and electron density inside a coronal hole.

In addition, there are two appendices. Appendix I gives the electron density, neutral particle density, and temperature profiles of the photosphere, chromosphere, transition zone and corona that we have used as a standard model of the quiet solar atmosphere. Appendix II gives a listing of the computer program that was used to modify the

standard solar atmosphere model and then trace ray paths through the atmosphere to determine radio brightness temperatures at different wavelengths. In addition to the program itself, we have included a sample input and output of this program.

## 2. Personnel

The period covered by this contract extended from July 1, 1977 to September 30, 1980. The principal investigator was Prof. Michael D. Papagiannis. From July, 1977 to September, 1978, Dr. Fred Wefer worked on the project as a post-doctoral research associate, while from January 1, 1979 to the end of the contract period, this position was held by Dr. Kile Baker. At various times during the period covered by the contract, three students (Terry Varner, Michael Van Steenberg, and Michele de la Pena) worked on various tasks of the project.

## 3. Publications

During the period covered by the contract, two papers, four scientific reports including this final report, and five abstracts have been published pertaining to the work of the contract. These publications are listed below:

### Papers

"Coronal Holes at 11.5 and 21 cm observed with the Arecibo Radio Telescope", M.D. Papagiannis and F.L. Wefer; Nature, 273, 520, 1978.

"Synoptic Charts of Solar 9.1 cm and Coronal Hole Data", F.L. Wefer and M.D. Papagiannis; Solar Physics, 67, 13, 1980.

#### Scientific Reports

"The Radio Spectrum of Coronal Hole 1", F.L. Wefer and M.D. Papagiannis; AFGL-TR-77-0292, Boston Univ., Ser. II, No. 65, 1977.

"Synoptic Charts of Coronal Holes and 9.1 cm Solar Data from May Through August 1973", F.L. Wefer, M.D. Papagiannis, M.E. Van Steenberg, T.M. Varner; AFGL-TR-78-0234, Boston Univ., Ser. II, No. 68, 1979.

"Correlation of High Latitude Coronal Holes with Solar Wind Streams High Above or Below the Ecliptic", K.B. Baker and M.D. Papagiannis; AFGL-TR-80-0123, Boston Univ., Ser. II, No. 71, 1980.

"Radio Studies of Coronal Holes", M.D. Papagiannis and K.B. Baker; AFGL-TR-81-0053, Boston Univ., Ser. II, No. 72, 1981.

#### Abstracts

"Coronal Hole Observations at 1420 and 2600 MHz with the Arecibo Radio Telescope", M.D. Papagiannis and F.L. Wefer; Bull. AAS, 9, 617, 1977.

"Observations of Enhanced Radio Emission at 15 GHz from a Coronal Hole Region", F.L. Wefer and M.D. Papagiannis; Bull. AAS, 9, 617, 1977.

"The Radio Spectrum of Coronal Holes", M.D. Papagiannis and F.L. Wefer; EOS, 59, 367, 1978.

"Synoptic Charts of Coronal Holes and 9.1 cm Data from  
May Through August 1973", F.L. Wefer, M.D.  
Papagiannis, H.E. Van Steenberg, and T.M. Varner;  
Bull. AAS, 10, 684, 1978.

"Solar Wind Streams at High Solar Latitudes and Their  
Correlation to Coronal Holes", M.D. Papagiannis  
and K.B. Baker, EOS, 61, 1095, 1980.

## Chapter 1

### RADIO OBSERVATIONS OF CORONAL HOLES FROM THE SKYLAB PERIOD

#### 1.1. The Radio Spectrum of Coronal Hole 1

Although by 1977 a number of groups had observed coronal holes at radio wavelengths (Dulk and Sheridan, 1974; Furst and Hirth, 1975; Wefer, et al., 1976; Wefer and Bleiweiss, 1976; Kundu and Liu, 1976; Chiuderi-Drago, 1974; Lantos and Avignnon, 1975; Covington, 1976), no one had analysed a single coronal hole at many different wavelengths covering a wide range of the radio spectrum. During the eight day period from June 25, 1973 to July 2, 1973 the coronal hole designated by the Skylab Workshop on coronal holes as CH1 was visible on the solar disk. On June 28, 1973 solar radio maps were made independently by several groups at several different radio observatories and different radio wavelengths: 8.6 mm and 2.0 cm - La Posta Observatory, 3.8 cm - NEROC Haystack Observatory, 9.1 cm - Stanford Radio Astronomy Institute, 21 cm - University of Sydney La Fleurs Radio Astronomy Field Station. On subsequent passages of the coronal hole, it was observed at three additional wavelengths: 2.8 cm - Bonn 100-m radio telescope, 1.8 m and 3.75 m - Culgoora radioheliograph.

Wefer and Papagiannis (1977) analysed these radio maps in detail and presented a radio spectrum of this hole by choosing a point inside the coronal hole and normalizing the brightness temperatures at each radio wavelength with the corresponding brightness temperatures of the solar disk

outside the coronal hole at the same radial distance from the center of the disk. The combined observations were used to produce the radio spectrum shown in Figure 1. This analysis indicated an enhancement of approximately 2% in the radio emission around 2.0 cm, which was consistent with the previous observations by Wefer, et al. (1976). At 2.8 cm the brightness temperature of the coronal hole is beginning to be clearly less than the solar disk value, and by 21 cm the brightness temperature has decreased to about 30% below the normal disk value. The minimum of the spectrum, i.e. the lowest value of the brightness temperature inside the coronal hole relative to the brightness temperature outside the coronal hole, appears to occur somewhere between 21 cm and 1 m.

The small enhancement (about 2%) at 2.0 cm was then and still remains a controversial point. The enhancement appears to be quite definite in the 1973 observations. The question of a possible enhancement at 2.0 cm in other coronal holes will be discussed in more detail in Chapter 4 when we consider the 1978 observations.

One other important feature of our analysis of CH1 radio data was the discovery that the coronal hole could indeed be observed in the 9.1 cm radio maps from Stanford. The Stanford people themselves had claimed to be unable to see coronal holes in their data. The fact that our radio spectrum indicates that one ought to be able to see coronal holes around 9 cm as 10-20% depressions in the brightness temperature relative to the solar disk background lead us to

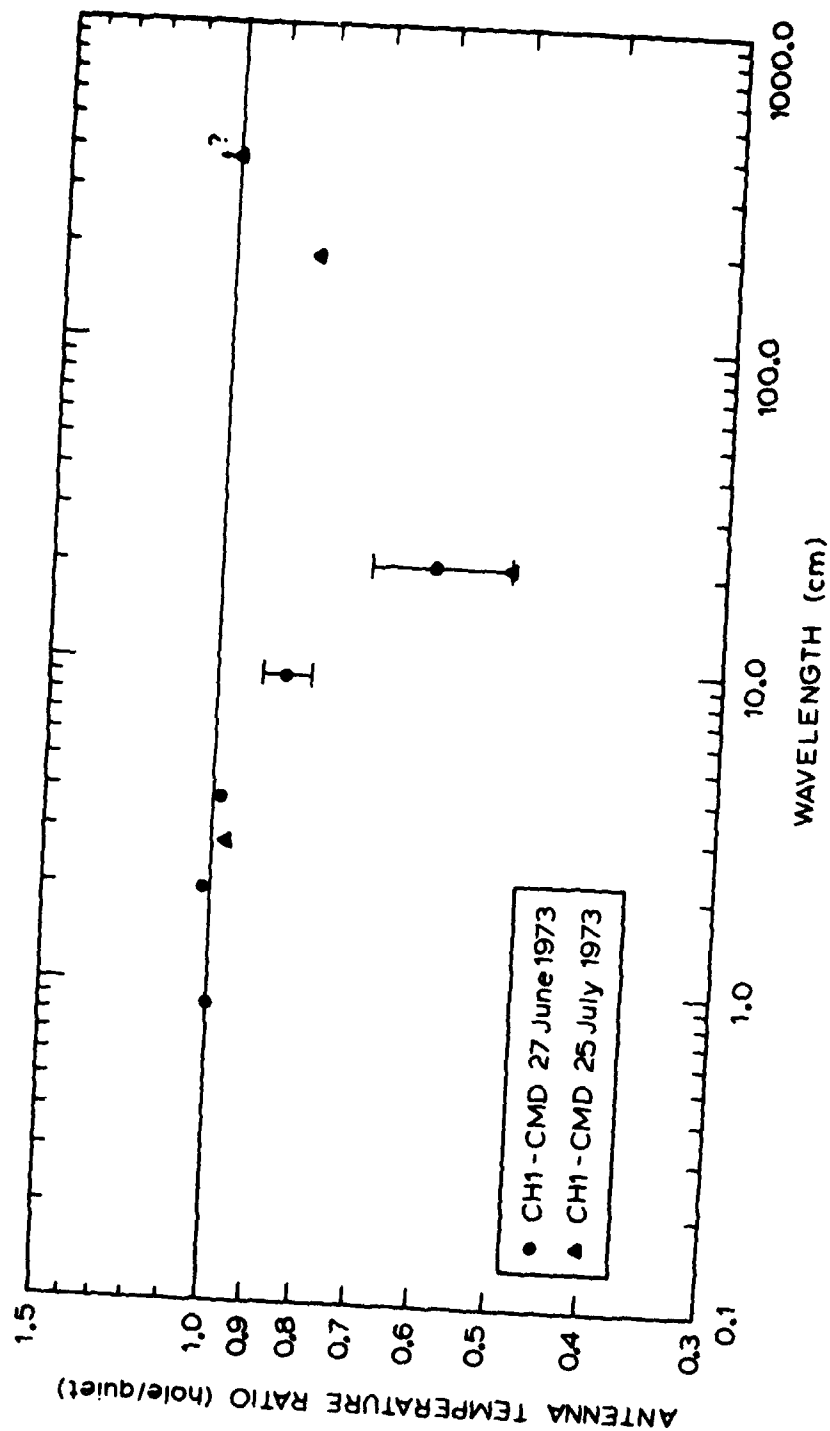


FIGURE 1



go back through all the 9.1 cm Stanford maps that were available during the Skylab period in a search for coronal holes. The results of that search are presented in the next section.

A detailed description of our work on CH1 is available in our Scientific Report No. 1, AFGL-TR-77-0292, Dec. 1977 by F.L. Wefer and M.D. Papagiannis.

#### 1.2. Identification of Coronal Holes on the Stanford 9.1 cm Synoptic Charts

The period from May 28, 1973 to August 11, 1973 was an ideal period for the study of coronal holes because it was the only time at which solar X-Ray data from ATM-Skylab and 9.1 cm radio maps from the Stanford Radio Astronomy Institute were simultaneously available. In addition, it was a period near solar minimum when large transequatorial coronal holes were present on the sun.

Our study of the radio spectrum of coronal hole CH1 (Wefer and Papagiannis, 1977) had demonstrated that a coronal hole could easily be seen at 9.1 cm. Graf and Bracewell (1975) had produced synoptic charts of the 9.1 cm data for each solar rotation from June, 1962 up to August, 1973, when the 9.1 cm system was shut down. In their charts the emphasis was placed on active regions and the lowest contoured level was at a brightness temperature of 40,000 K. The central disk brightness temperature for the quiet sun at

9.1 cm is approximately 30,000 K, and since at this wavelength coronal holes manifest themselves as 10-20% depressions in the brightness temperature relative to the quiet sun background, it is understandable why the synoptic charts produced by Graf and Bracewell did not show any coronal holes.

Graf and Bracewell kindly provided us with the computer tapes of the daily data of their 9.1 cm observations, and from these data, we produced our own synoptic charts, emphasizing contours near and below the quiet sun level. The basic procedure was a simple one. On each day, we extracted the data corresponding to the central meridian and collected 30 days worth of data to form a grid from which a synoptic contour map was drawn covering slightly more than one Carrington rotation. Since this method produced charts based only on central meridian data, they are suitable only for studying long-lived coronal holes. As a check on the results obtained in this fashion, we also constructed a few charts using data just to the left or right of the central meridian. These charts showed the same general features as the central meridian charts, but differed somewhat in the finer (and shorter-lived) details.

A typical synoptic chart is shown in Figure 2. The shaded areas show the positions of coronal holes as determined from the ATM-Skylab data (Nolte, et al., 1976b) for rotation 1602. In this chart, CH1 (near longitude zero) and CH5 (near longitude 260°) are clearly manifested as depressions in the 9.1 cm emission. Coronal hole CH3, as

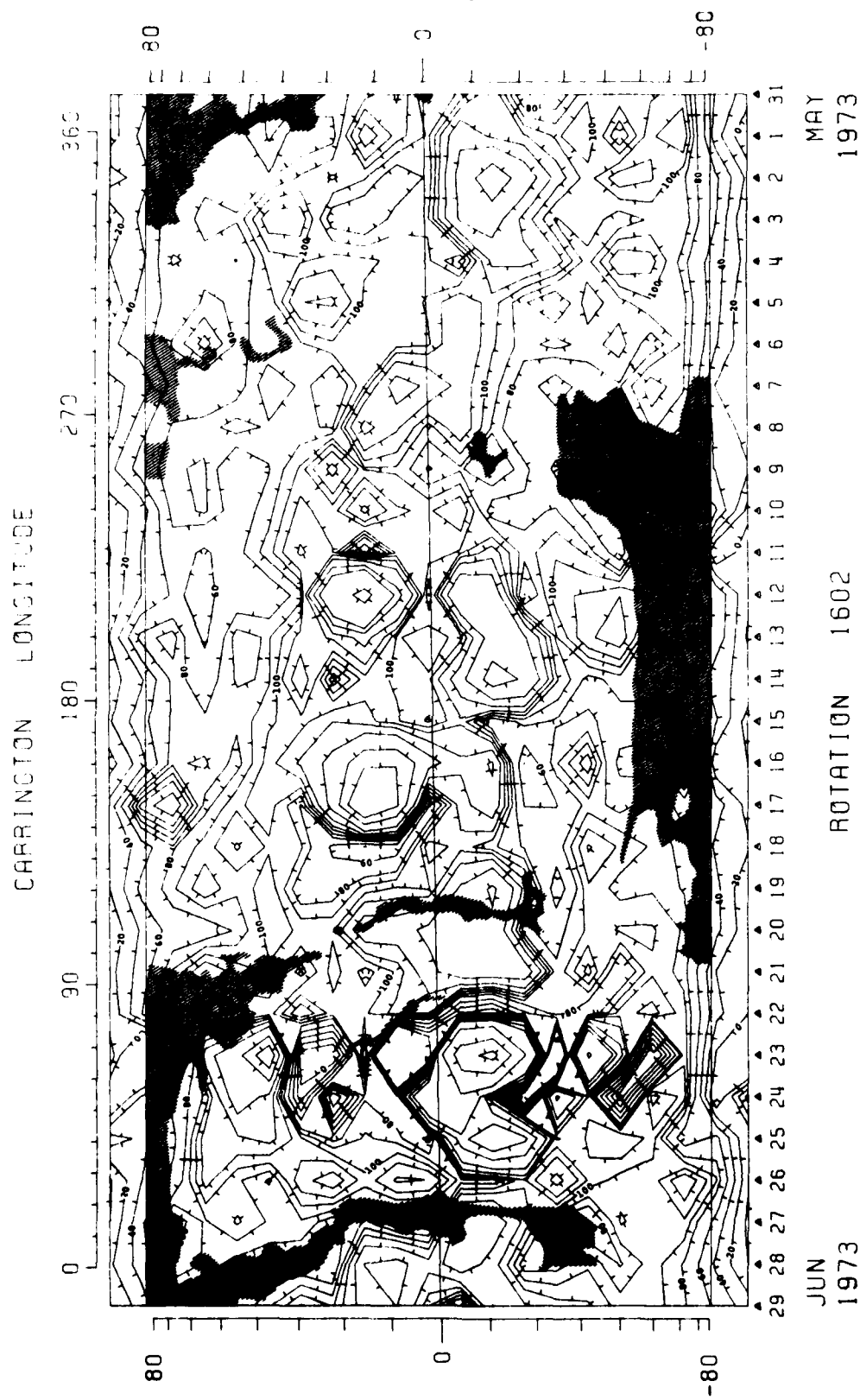


FIGURE 2

well as several smaller coronal holes, did not show up in the 9.1 cm chart, probably because their sizes are smaller than the beamwidth of the Stanford antenna and the additional side-lobe interference from nearby active regions.

A complete description of this work is included in our Scientific Report No. 2, AFGL-TR-78-0284, January 1979 by F.L. Wefer, M.D. Papagiannis, T. Varner and M. Van Steenberg, and in the paper, "Synoptic Charts of Solar 9.1 cm and Coronal Hole Data" by F.L. Wefer and M.D. Papagiannis (1980).

## Chapter 2

### HIGH LATITUDE CORONAL HOLES AND THEIR CORRELATION TO HIGH LATITUDE INTERPLANETARY SCINTILLATION

#### 2.1. The Correlation of IPS and Coronal Hole Data

Although the correlation between large equatorial coronal holes and high speed solar wind streams observed near the earth has been well established (Krieger, et al., 1973; Kopp and Orrall, 1977; Hundhausen, 1977), the generalization that all coronal holes are sources of high speed solar wind streams is not well established. In fact, Hundhausen (1977) has suggested that the correlation may not hold true for smaller coronal holes.

A general correlation between large coronal holes and high solar wind velocities, derived from interplanetary scintillation (IPS) measurements, was obtained in the 70's at the University of California, San Diego by Rickett, et al. (1976). They found that about half of the large coronal hole passages seen over several solar rotations were associated with high speed solar wind streams.

Recently, Coles, et al. (1980) have correlated the average solar wind speed observed at high solar latitudes with the size of the polar coronal hole. They have shown that as the solar cycle approaches maximum, the polar coronal hole decreases in size and the average solar wind speed at high solar latitudes diminishes.

Nevertheless, a definitive correlation showing a connection between specific high latitude coronal holes and

high speed solar wind streams corresponding to similar high solar latitudes had not been attempted. To this end we made a more detailed correlation analysis between the velocities of solar wind streams high above or below the ecliptic obtained from IPS data, and the positions and shapes of high solar latitude coronal holes obtained from coronal hole synoptic maps constructed from the  $10330 \text{ \AA}$  Helium spectroheliograms.

For the past several years there have been only two groups making daily interplanetary scintillation measurements, namely, the group headed by Coles at UCSD and the group headed by Watanabe and Kakinuma at the Toyokawa Observatory in Japan. We utilized both sets of data in our correlation in order to provide as complete a coverage in time as possible and whenever possible to provide a check of one set against the other. Our study covered the two and a half year period from January 1, 1977 to June 30, 1979. For the first year and a half (Jan. 1, 1977 to June 30, 1978) we had IPS data from both UCSD and Toyokawa. For the last year, however, we only had data from UCSD because the Toyokawa data had not yet been processed and published.

The position and shapes of coronal holes were determined from the published monthly synoptic charts (Solar Geophysical Data Prompt Reports) made by Dr. J. Harvey from the Kitt Peak Helium  $10830 \text{ \AA}$  spectroheliograms. It should be noted, however, that because of the difficulties involved in interpreting these spectroheliograms, there is some uncertainty in the details and exact boundaries of the

coronal holes shown in the monthly synoptic charts. In addition, for the coronal holes present in July, 1978, we have also made use of our radio observations to determine the structure and boundaries of the coronal holes. This work is discussed in detail in Chapter 4 and the radio maps are shown in Figures 23 - 44.

The method of analysis was a simple one. If the point of maximum scintillation, P, for a particular radio source (see Figure 3) corresponded to a solar latitude that would intersect the boundaries of a coronal hole, we looked at the IPS data to determine if a high speed solar wind stream was present. We would expect the coronal hole to produce a scintillation effect (a high speed wind stream) when it is pointed toward the point of maximum scintillation. The actual effect, however, would be delayed by approximately one day, which is the time it would take for the high speed wind stream to advance from the coronal hole to the scintillation point. The actual magnitude of the delay is a function of the solar wind speed and the distance of the scintillation point from the sun and can be computed through an iterative procedure.

To determine the correlation we had to define a set of criteria for determining how good a particular correlation was. We defined four categories for the correlation:

- 1) Very Good - High speed solar wind streams were observed on the expected dates. The increase in wind speed was significant (25% or more). If the boundary of the coronal hole was such that the





scintillation point passed in and out of the coronal hole area more than once, this should be reflected in the IPS data.

- 2) Good - A significant increase in the solar wind, followed by a corresponding decrease, must have occurred within 2 days of the expected dates.
- 3) Fair - The solar wind speed must have been higher than average during most of the expected period (with a tolerance of 2 days).
- 4) Poor - The solar wind speed stayed near the average value or decreased during the dates of expected high speed solar wind.

Utilizing these criteria, we were able to analyse a total of 26 cases and classify them in one of the above four categories. We were unable to classify seven other cases due to a lack of all the needed data. As can be seen from the histogram of the 26 cases analysed (Figure 4), the correlation in about 50% of the cases was either "Very Good" or "Good", while in fewer than 25% of the cases the correlation was "Poor".

Considering the assumptions (radial propagation of solar wind streams, constant solar wind velocity along the radial path, etc.) involved in this analysis, the sizable uncertainties in the solar wind speeds deduced from IPS measurements, as well as the uncertainties in the positions and boundaries of coronal holes deduced from the 10830 Å synoptic charts, the overall correlation is surprisingly good. We conclude that it is certainly true that a

# HISTOGRAM OF THE CORRELATIONS

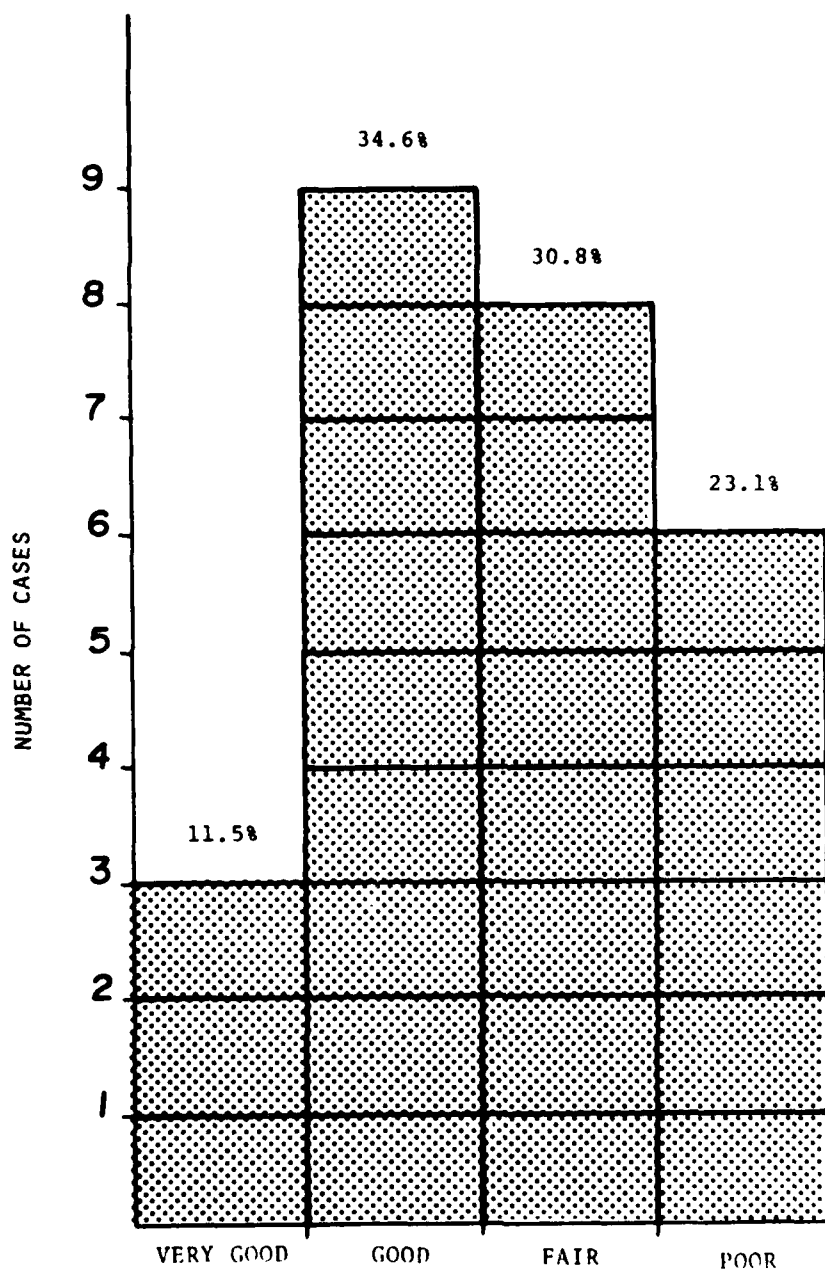


FIGURE 4

significant fraction (probably most) of the high solar latitude coronal holes are sources of high speed solar wind streams. Nevertheless, it is also quite possible that, like the equatorial coronal holes, some high latitude coronal holes do not produce high speed solar wind streams on a continuous basis, although at various stages in their evolution, they may do so. It is also quite evident that the strength of the solar wind streams is related to the size of the coronal hole. It is quite possible therefore that some of the smaller streams are totally missed, either because of their relatively short duration and our limited means of observation, or because they get dissipated or diverted in interplanetary space before they reach the expected point P of maximum scintillation.

A complete description of this study, along with the data used is given in our Scientific Report No. 3, AFGL-TR-80-0123, April, 1980 by K.B. Baker and M.D. Papagiannis.

Chapter 3

OBSERVATIONS OF CORONAL HOLES AT ARECIBO AND HAYSTACK

IN SEPTEMBER OF 1977

3.1. Coronal Hole Observations at 11.5 and 21 cm with the Arecibo Radio Telescope in 1977

During the five day period from August 31 to September 4, 1977, we obtained seven maps of the sun at 11.5 cm and 21 cm using the Arecibo radio telescope. These solar maps were made by two different methods. In the drift scan method the telescope remained stationary and the sun was allowed to drift past the beam of the antenna. Each scan took about 4 minutes and the total map, consisting of 21 scans, took about 1.5 hours. In the second method the antenna was driven at twice the siderial rate while executing a boustrophedonic raster. This method made it possible to cut the time required for each map in half and allowed us to make maps at both 11.5 cm and 21 cm during the approximately two hour period around local noon that the sun can be observed with the Arecibo radio telescope at this time of the year. We were thus able to make seven solar maps during this five day observing period.

This was the first time that the Arecibo radio telescope was used to make solar maps. The Arecibo dish was of unique value for this project because of its high sensitivity (~1% of solar disk background) and its high

angular resolution (3-4 arcmin) at decimeter (11.5 and 21 cm) wavelengths. The discovery that coronal holes become clearly visible at these wavelengths confirmed the importance of the Arecibo radio telescope for decimetric solar observations.

The results of this project are shown in Figure 5, which shows five of the solar maps made during this five day period. The coronal hole boundaries indicated on each map were obtained from the Kitt Peak 10830 Å spectroheliograms, which were provided by Dr. J. Harvey of the Kitt Peak Observatory. These spectroheliograms are used for an optical identification of coronal holes in the absence of X-ray or UV observations. The 10830 Å spectroheliogram for September 2, 1977 is also shown in Figure 5.

The coronal hole in the southern hemisphere is very obvious and is very similar in shape and position to the coronal hole seen in the 10830 Å spectroheliogram. The coronal hole in the northern hemisphere was much narrower and was therefore more difficult to observe at radio wavelengths. Nevertheless, a depression in radio emission is clearly visible in the region of the north pole. Unfortunately, the picture in the north is confused by the presence of several filaments (indicated by dark wiggly lines) which also show up as depressions at radio wavelengths (Straka, Papagiannis and Kogut, 1975).

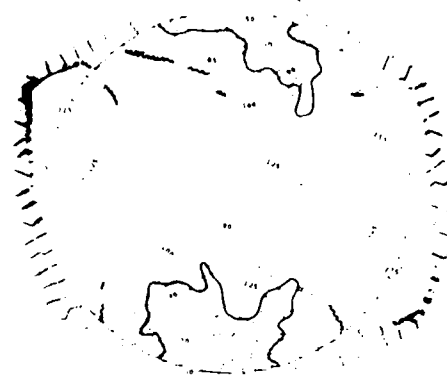
This work is more fully reported in the article, "Coronal holes at 11.5 and 21 cm observed with the Arecibo radio telescope", in Nature by M.D. Papagiannis and F.L. Wefer, 1978.



31 August

1530 UT

11.5 cm



1640 UT

21.1 cm



2 September

1610 UT

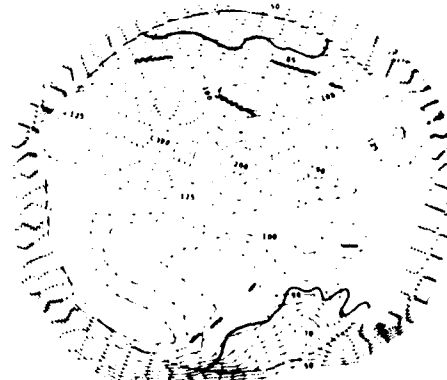
11.5 cm



4 September

1630 UT

11.5 cm



1534 UT

21.1 cm

FIGURE 5

### 3.2. Coronal Hole Observations at Haystack and La Posta in 1977

In addition to the Arecibo radio maps, we were also able during the same period to make radio maps at 3.81 cm and 1.94 cm using the Haystack Observatory radio telescope. These maps, along with maps at 2.0 cm and 0.36 cm from the La Posta Observatory are shown in Figure 6. The position of the coronal holes and filaments are also indicated on these maps. The coronal holes appear as slight depressions at 3.81 cm. At 2.0 cm and 1.94 cm, the holes appear as slight enhancements. This apparent enhancement will be discussed in more detail in Chapters 4 and 5.

### 3.3. The Radio Spectrum of the September 1977 Coronal Hole

From our observations at Arecibo and Haystack, combined with additional solar radio maps made by the La Posta observatory in California, we were able to determine a partial radio spectrum of this coronal hole (Figure 7). The results are quite consistent with those for CH1 in 1973 (Figure 1 in Chapter 1) particularly with respect to the approximately 2% enhancement around 2 cm.

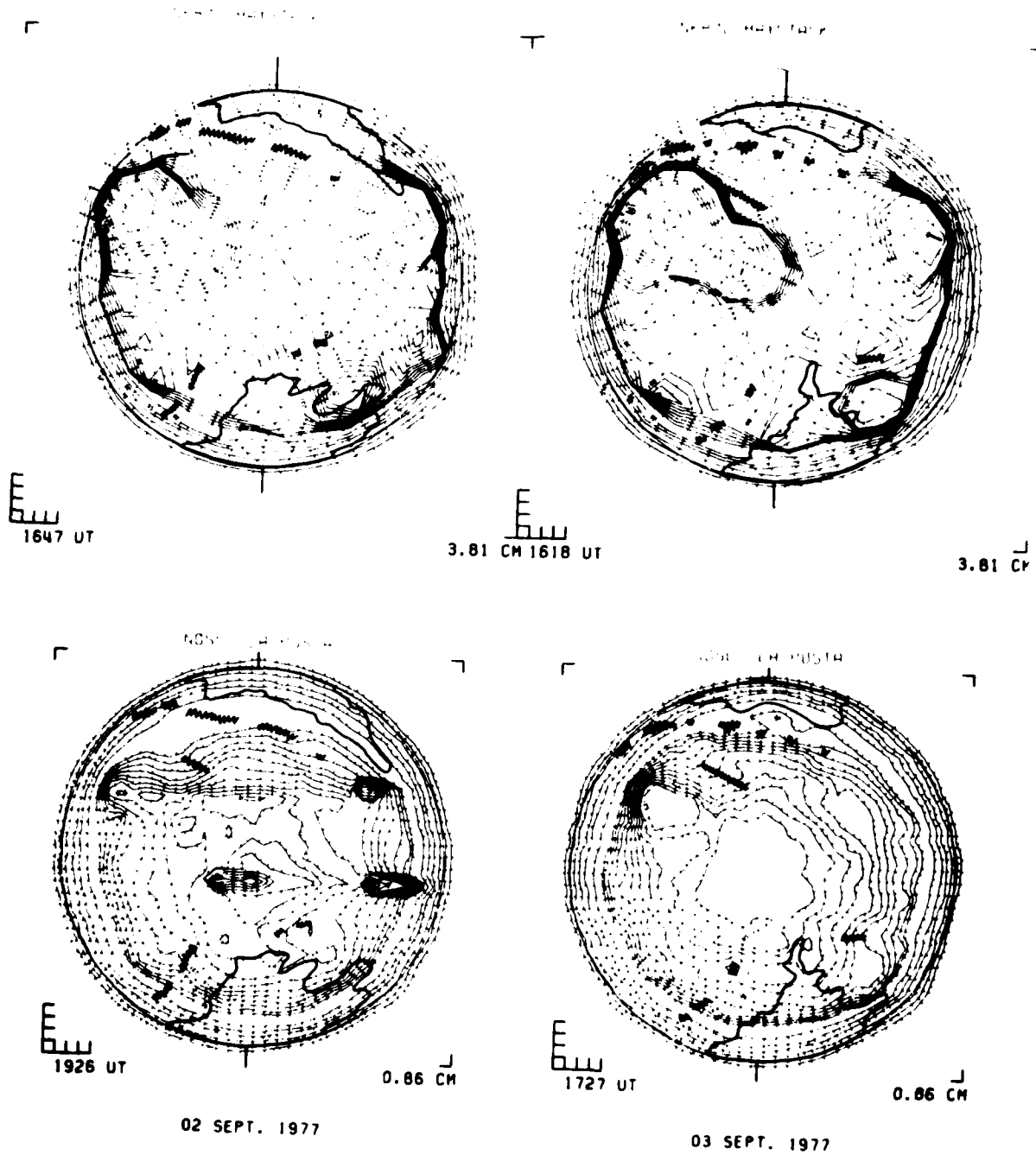


FIGURE 6



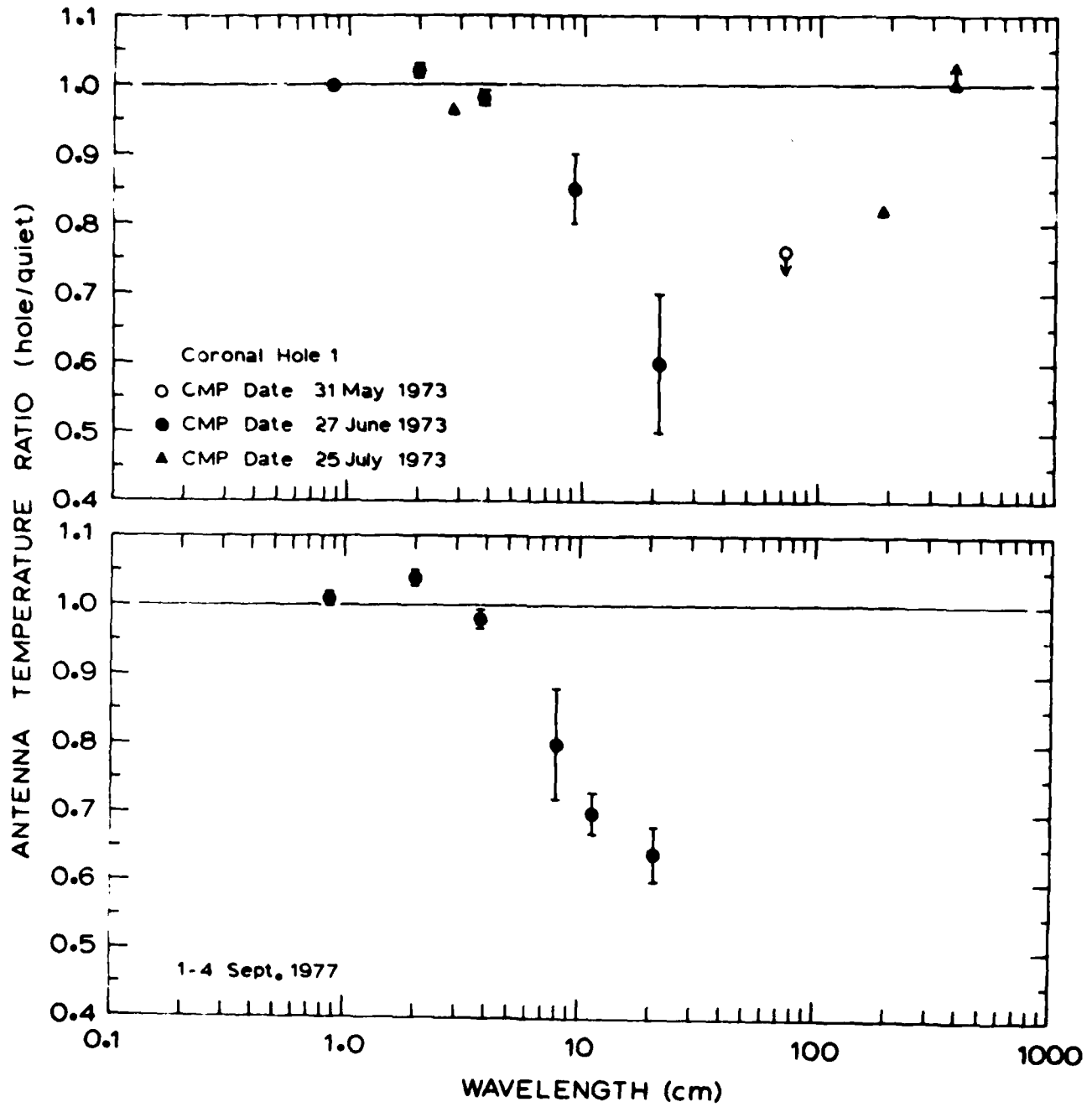


FIGURE 7

Chapter 4

CORONAL HOLE RADIO OBSERVATIONS DURING JULY 1973

4.1. International Effort

From the previous work it had become clear that simultaneous observations of coronal holes over a wide range of radio wavelengths would allow us to determine the radio spectrum of coronal holes, which would be of great value in our effort to understand the internal structure and the physics of coronal holes. It would also be useful to have a certain amount of redundancy in the observations to insure a higher level of dependability on the data.

Starting early in 1978 we began to organize an international co-operative effort to observe coronal holes at many different radio wavelengths. The project was well received by many groups around the world and the time period selected for this combined effort was July of 1973. The month of July was chosen primarily because we wanted to include observations at 21 cm and 11.5 cm from the Arecibo observatory which can observe the sun only during the summer and allows the longest observing time near the summer solstice. In addition, most of the participating observatories were located in the northern hemisphere and would be expected to have better observing conditions during the summer months. In order to increase the probability that a coronal hole would be present on the solar disk during our observations, we decided to use two separate observing periods of about five days each separated by about ten days.

The two periods were July 6-10 and July 15-13, 1978.

TABLE 1

Observatory Location	Size	Wavelengths(cm)	Resolution
U.Brit.Col. Canada	5m	0.41	4.0'
La Posta California	18.3m	2.0, 0.86	4', 2.8'
Haystack Massachusetts	36.6m	3.81, 1.93 1.38, 0.69	4.4', 2.2' 1.6', 0.3'
Itapetinga Brazil	13.7m	1.39, 0.70	4', 2'
Toyokawa Japan	437m	8.0, 3.0	2', 2'
Arecibo Puerto Rico	300m	21.4, 11.5	3.8', 3.3'
Culgoora Australia	2000m	187, 375	4', 3'

The participating groups, the sizes of their radio telescopes, the wavelengths at which they were making solar maps, and the angular resolution of these maps are summarized in Table 1. Unfortunately the radio maps from the Toyokawa observatory and the University of British Columbia had severe sidelobe problems and difficulties with the processing of their radio data which made these maps virtually useless for studying coronal holes. These maps, therefore, were not included in our analysis.

#### 4.2. First Period Observations (July 6-10, 1978)

The first period chosen for the radio observations was from July 6 to July 10, 1978. Not all observatories were able to make observations for the entire period, but there

is nonetheless a reasonable overlap of dates from all observatories. Table 2 lists the solar parameters,  $P$ ,  $B_0$ , and  $L_0$  (Carrington Longitude of the Central Meridian) at 0000 UT for each of the six days of the first period.

TABLE 2  
Solar Parameters at 0000 UT

DATE	$L_0$	$B_0$	$P$
7-6	235	+3.4	-0.6
7-7	272	3.5	-0.1
7-8	259	3.6	+0.3
7-9	246	3.7	+0.8
7-10	232	3.8	+1.2

Table 3 lists the participating observatories and indicates the wavelengths and the days on which each observatory made its observations.

TABLE 3  
Participating Observatories - First Period Observations

Observatory	Wavelength(cm)	July Date				
		6	7	8	9	10
La Posta	0.86	X	X	X	X	X
La Posta	2.00	X	X	X		X
Haystack	0.69			X		X
Haystack	1.38			X	X	X
Haystack	1.93			X	X	X
Haystack	3.81				X	X
Itapetinga	0.70	X	X	X		
Itapetinga	1.39	X	X	X		
Arecibo	11.5	X	X	X		
Arecibo	21.4	X	X			
Culgoora	187		X			
Culgoora	375		X	X		

As is clear from Table 3, July 8 is the date on which the most complete coverage is available.

The first period turned out to be a poor one for the

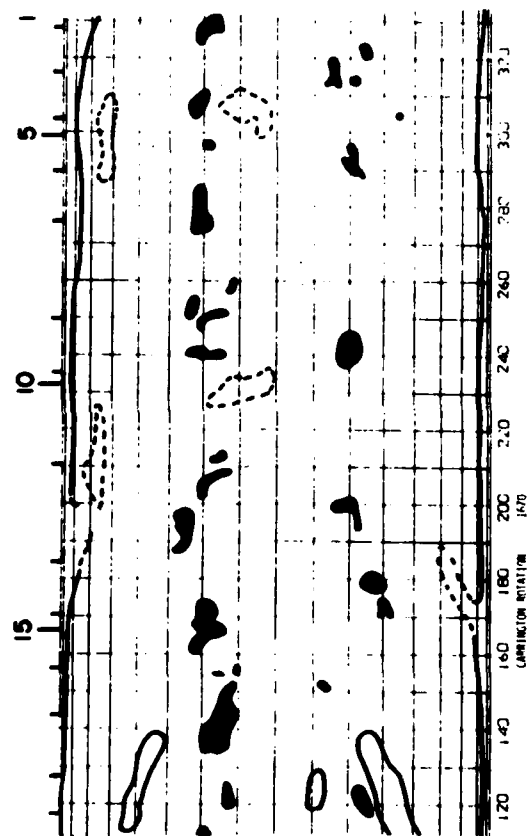
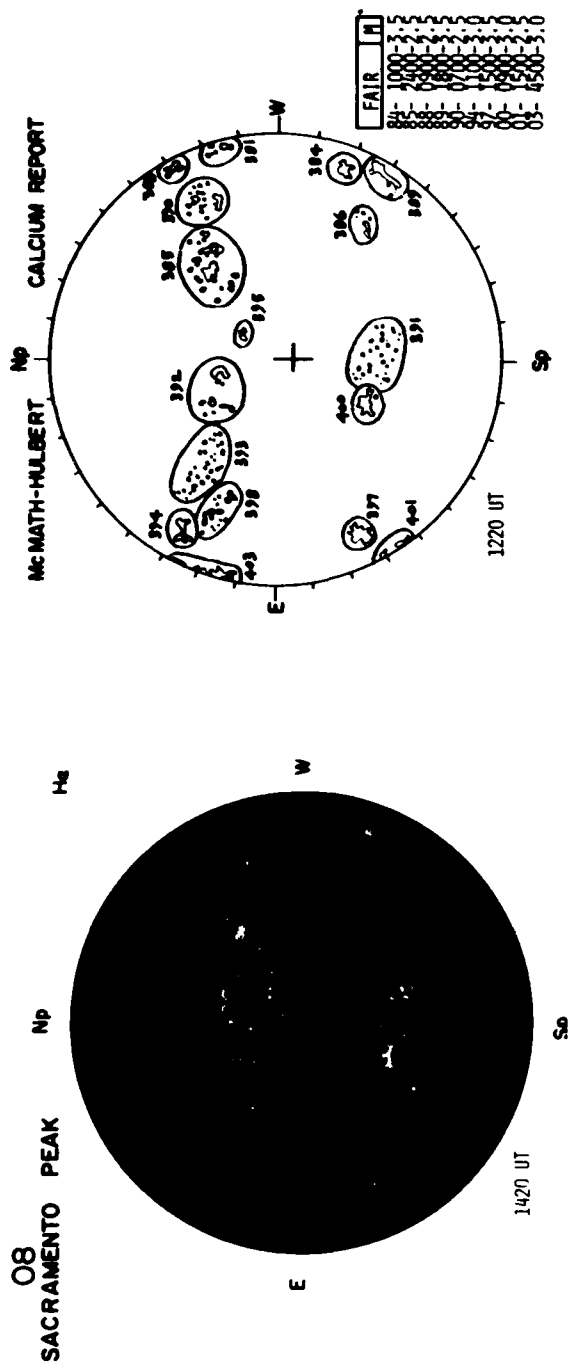


FIGURE 8

purpose of observing coronal holes. The Helium 10830 Å data show only the usual small polar depressions. The helium synoptic map from Kitt Peak for half a Carrington rotation centered approximately on July 7 is shown in Figure 8. There are no coronal holes but there are several active regions present. These active regions can also be clearly seen in the H $\alpha$  and Calcium pictures of the sun for this period. The H $\alpha$  picture from Sacramento Peak and the MacMath-Hulbert Calcium Report for July 8 are also shown in Figure 8. The three largest active regions are McMath 15385, 15391, and 15393. The H $\alpha$  picture shows a very clearly defined filament in the northern hemisphere at an approximate Carrington longitude of 240°. Thus, during the first period this filament is always on the east side of the central meridian. It is important to note the position of this filament, since, as mentioned above, large filaments appear very similar to coronal holes on radio maps.

#### Radio Maps for July 6-10, 1978

Figures 9 - 20 show representative maps from the first period observations. Although some details vary from day to day, the important features are relatively constant over the five day period from July 6 to July 10.

The shortest wavelength data available are the 0.69 cm maps from the Haystack observatory. At this very short wavelength all the information comes from deep in the chromosphere and all solar features, including the active

08 JUN 1979

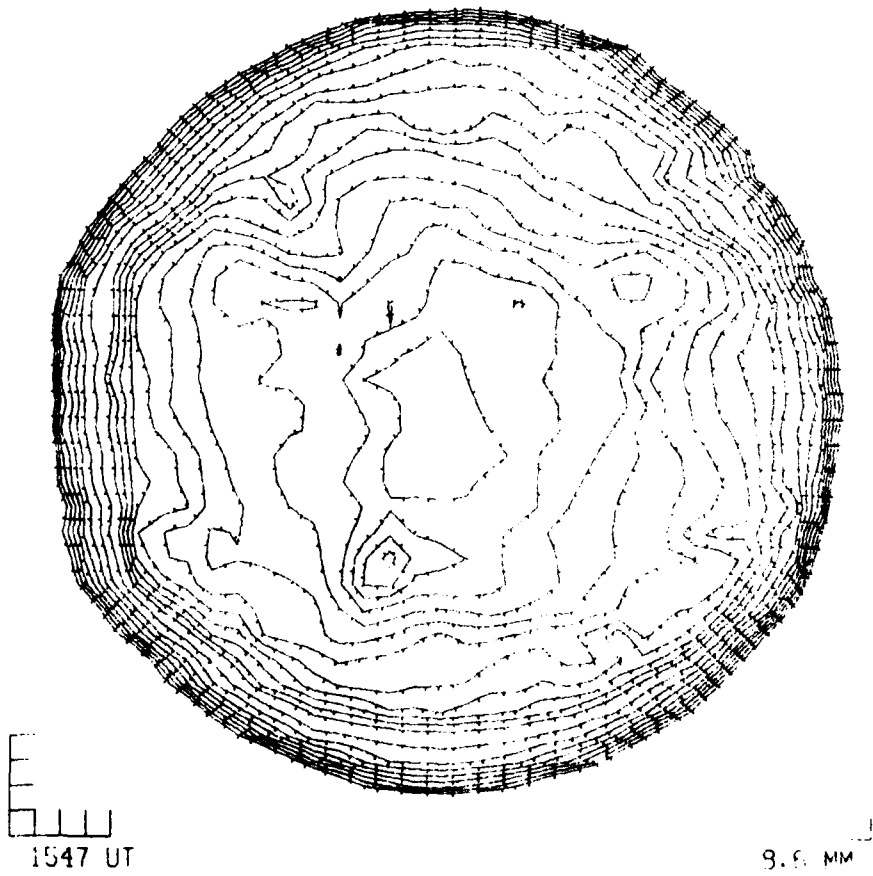
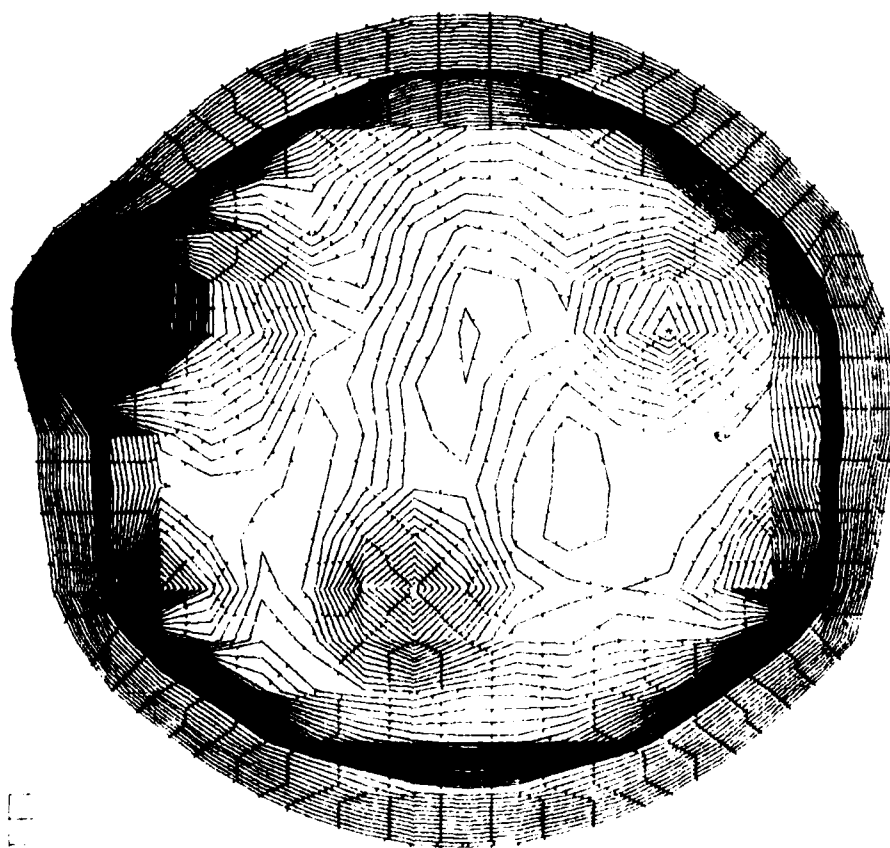


FIGURE 9

08 JULY 1978



1000 FT

2000 FT

FIGURE 10



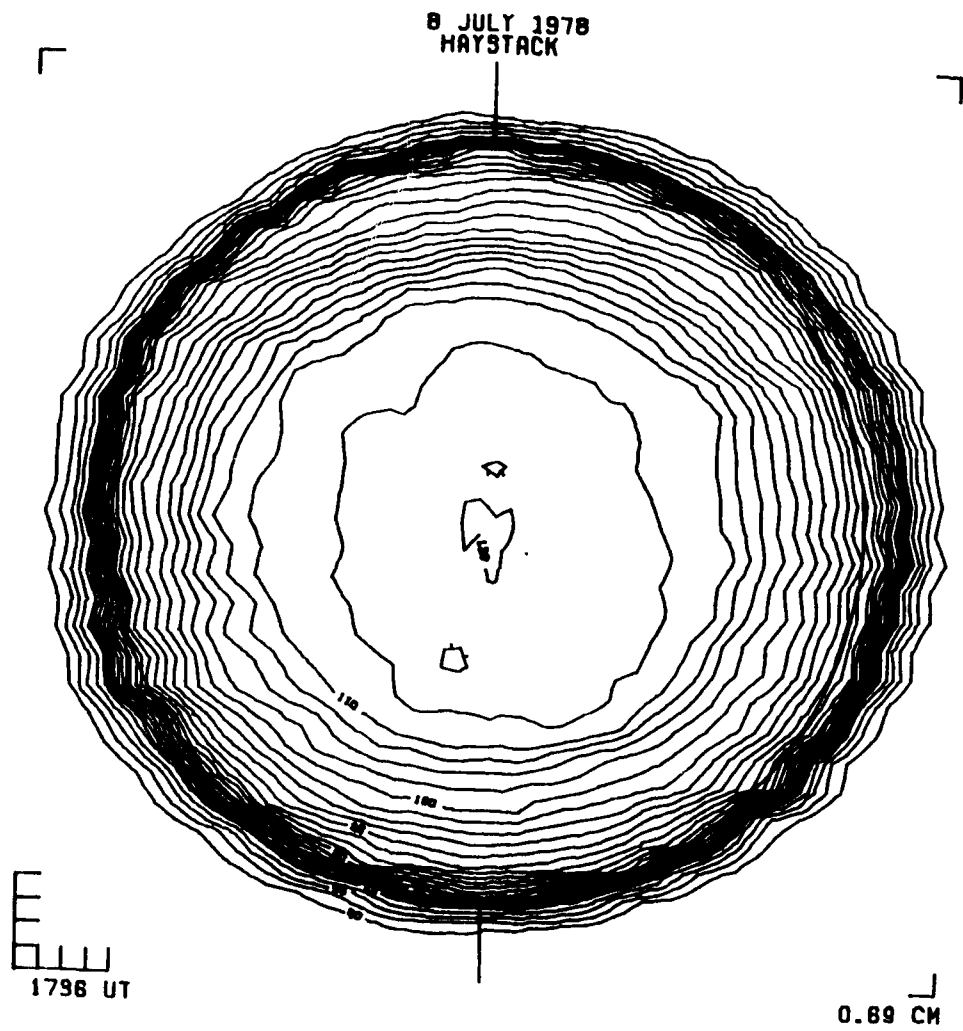


FIGURE 11

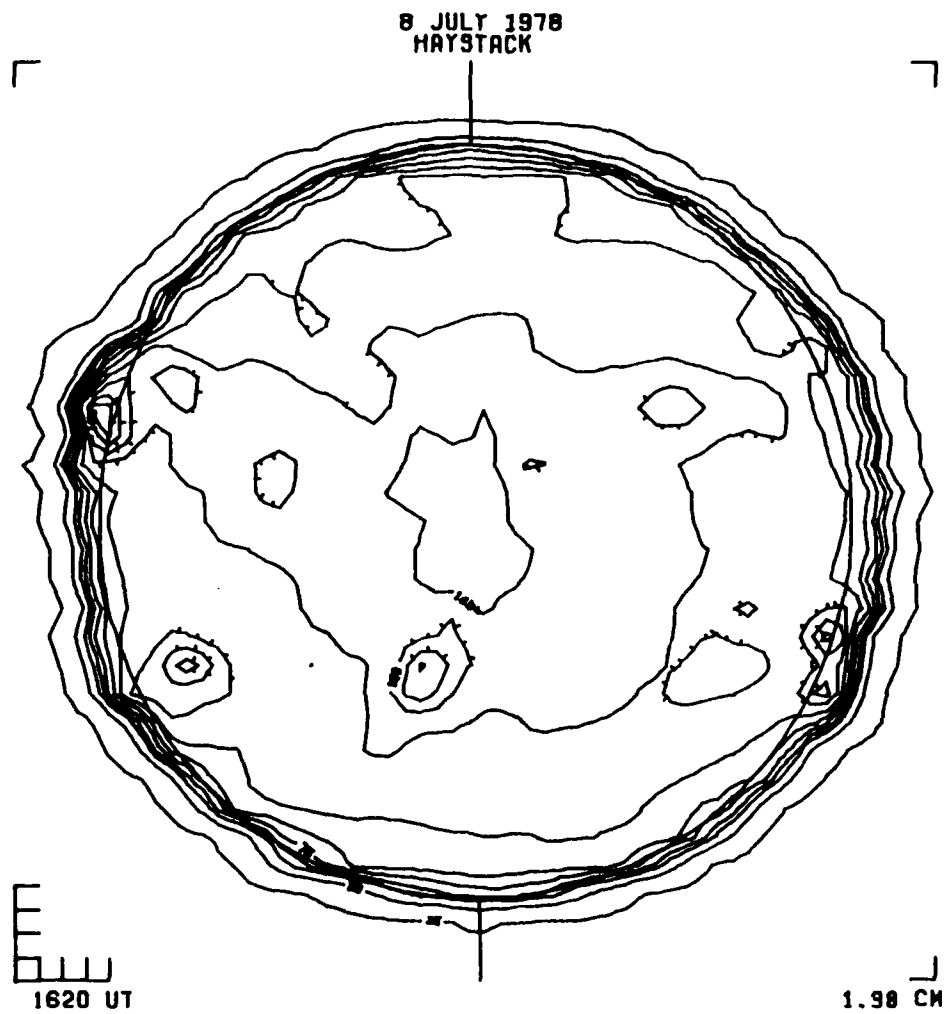


FIGURE 12

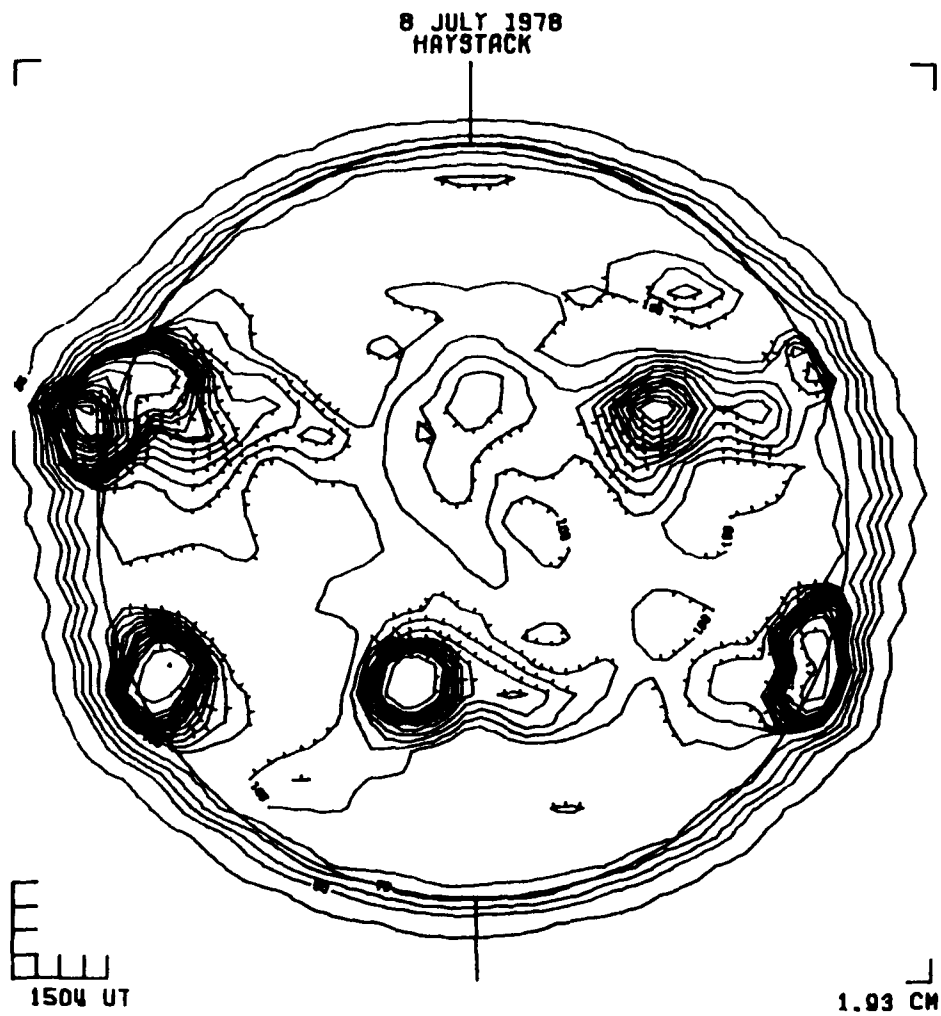


FIGURE 13

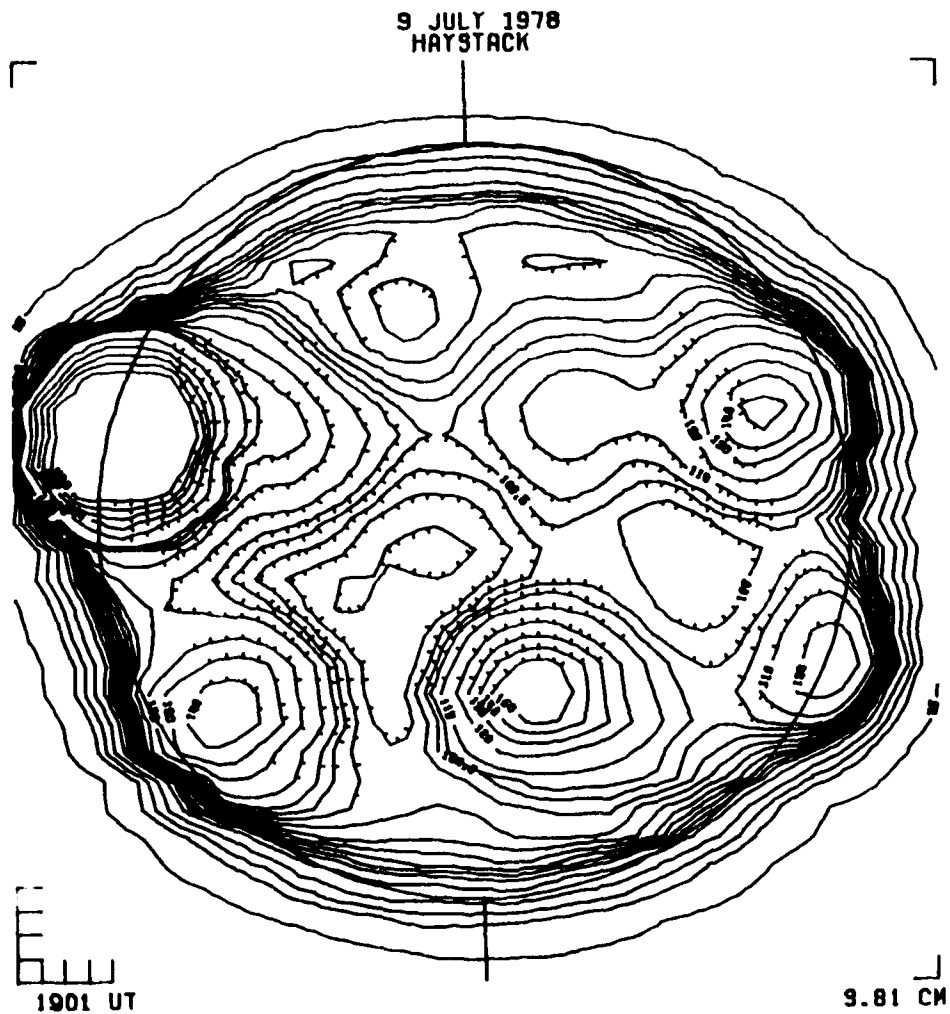


FIGURE 14

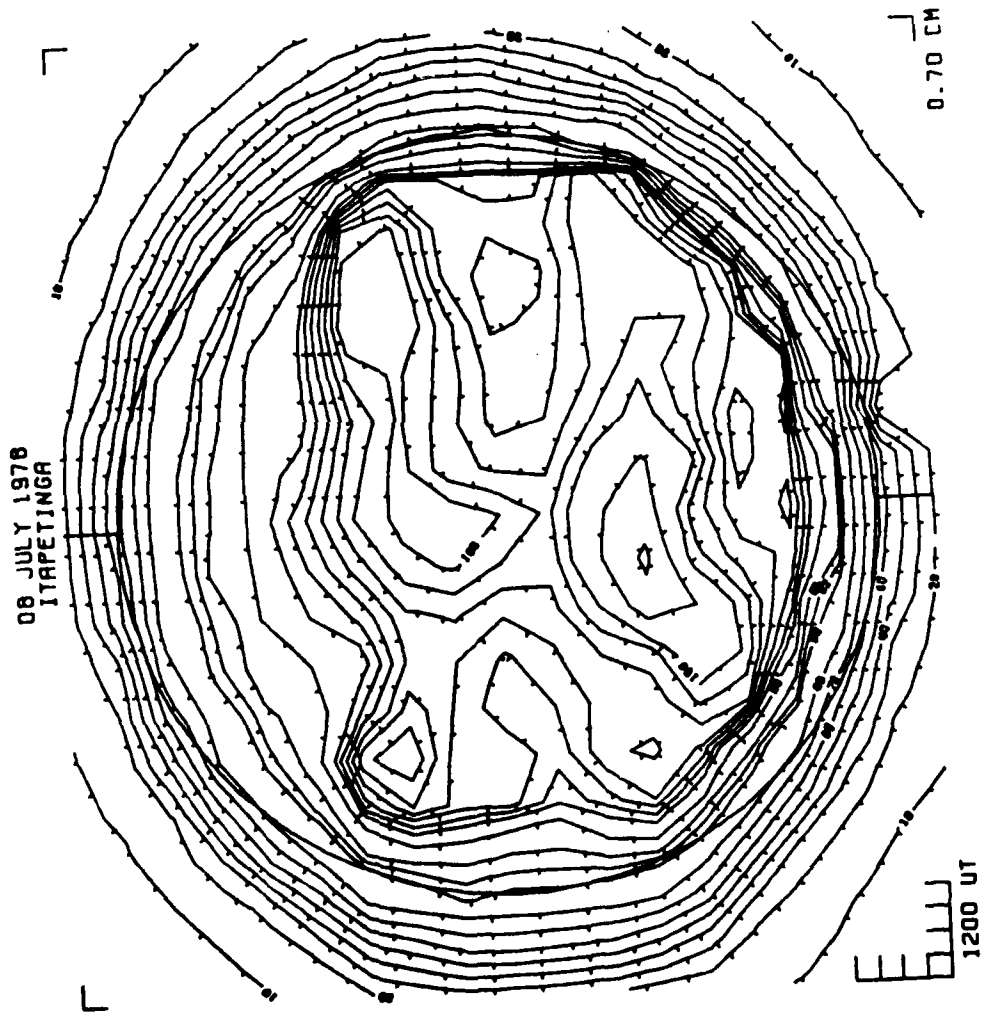


FIGURE 15

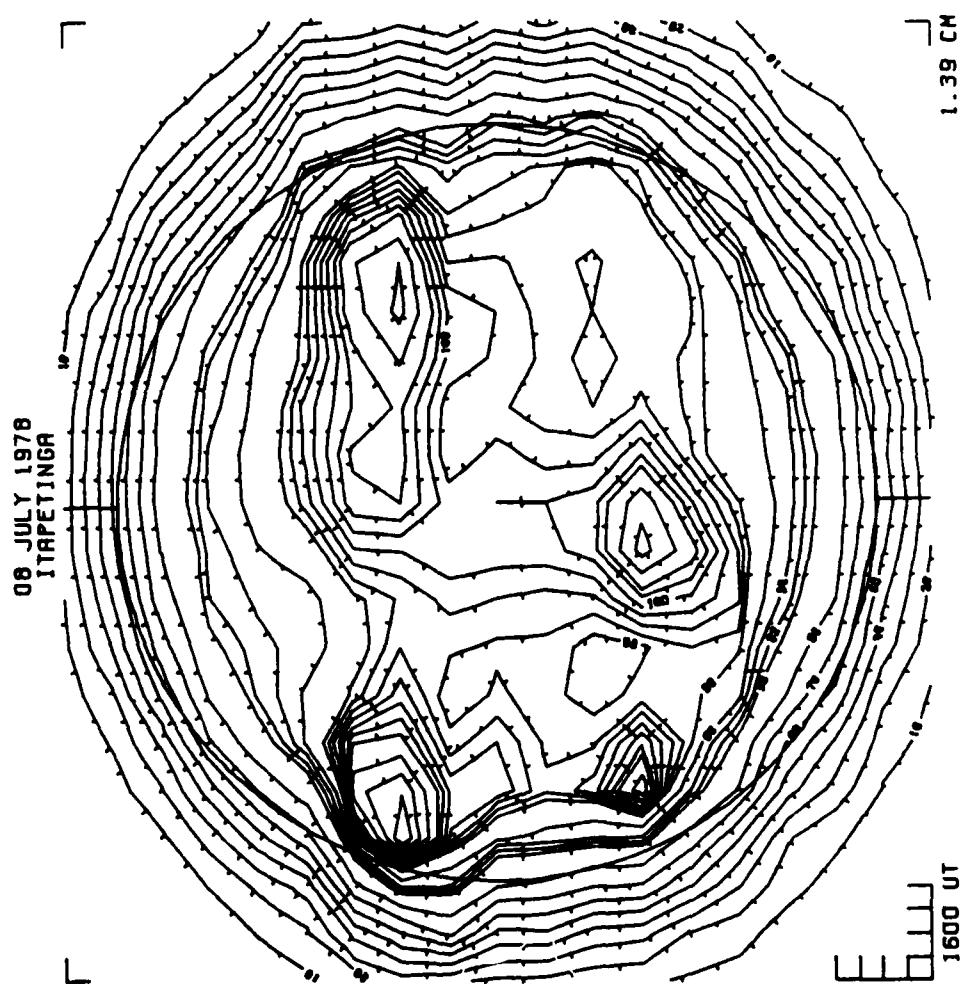


FIGURE 16

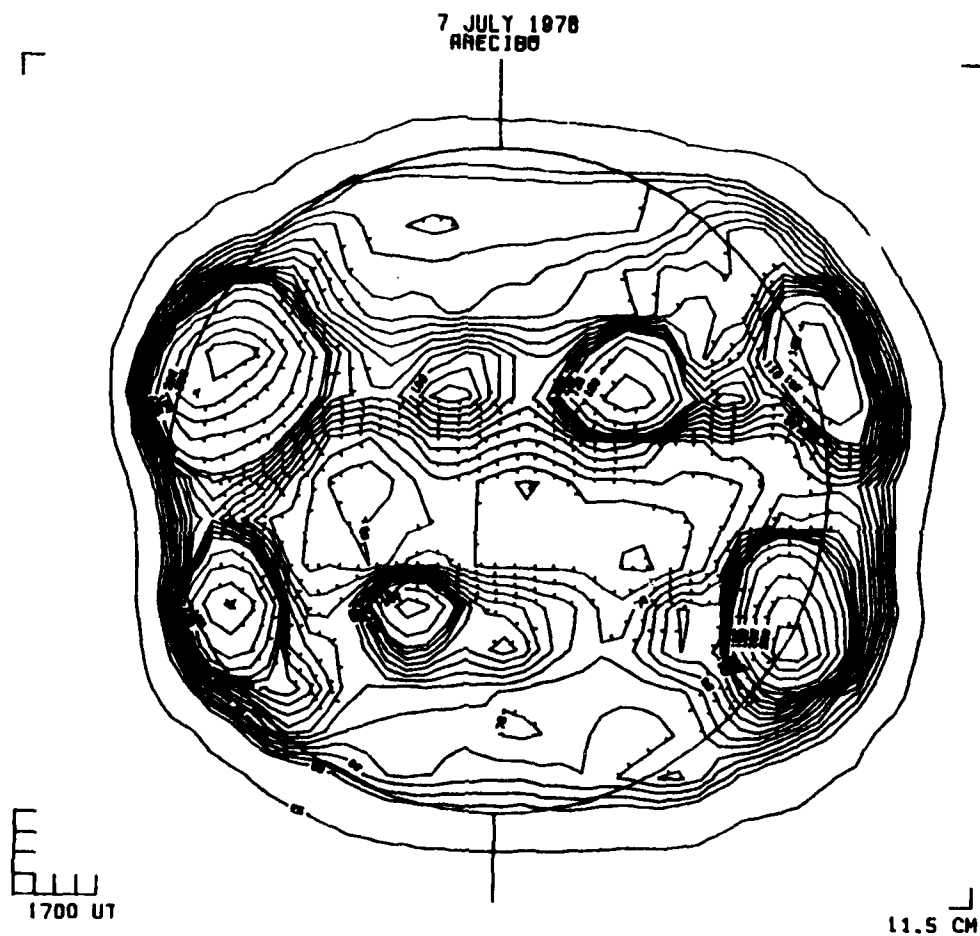


FIGURE 17

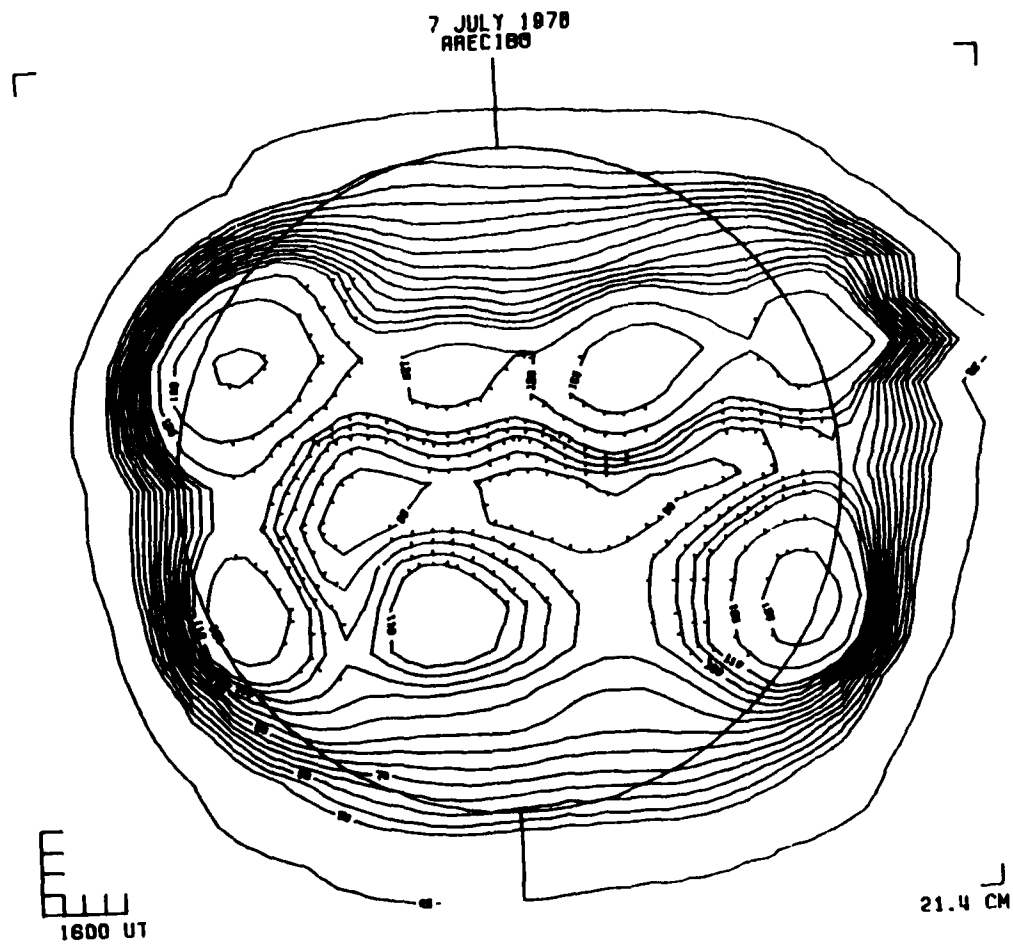


FIGURE 18



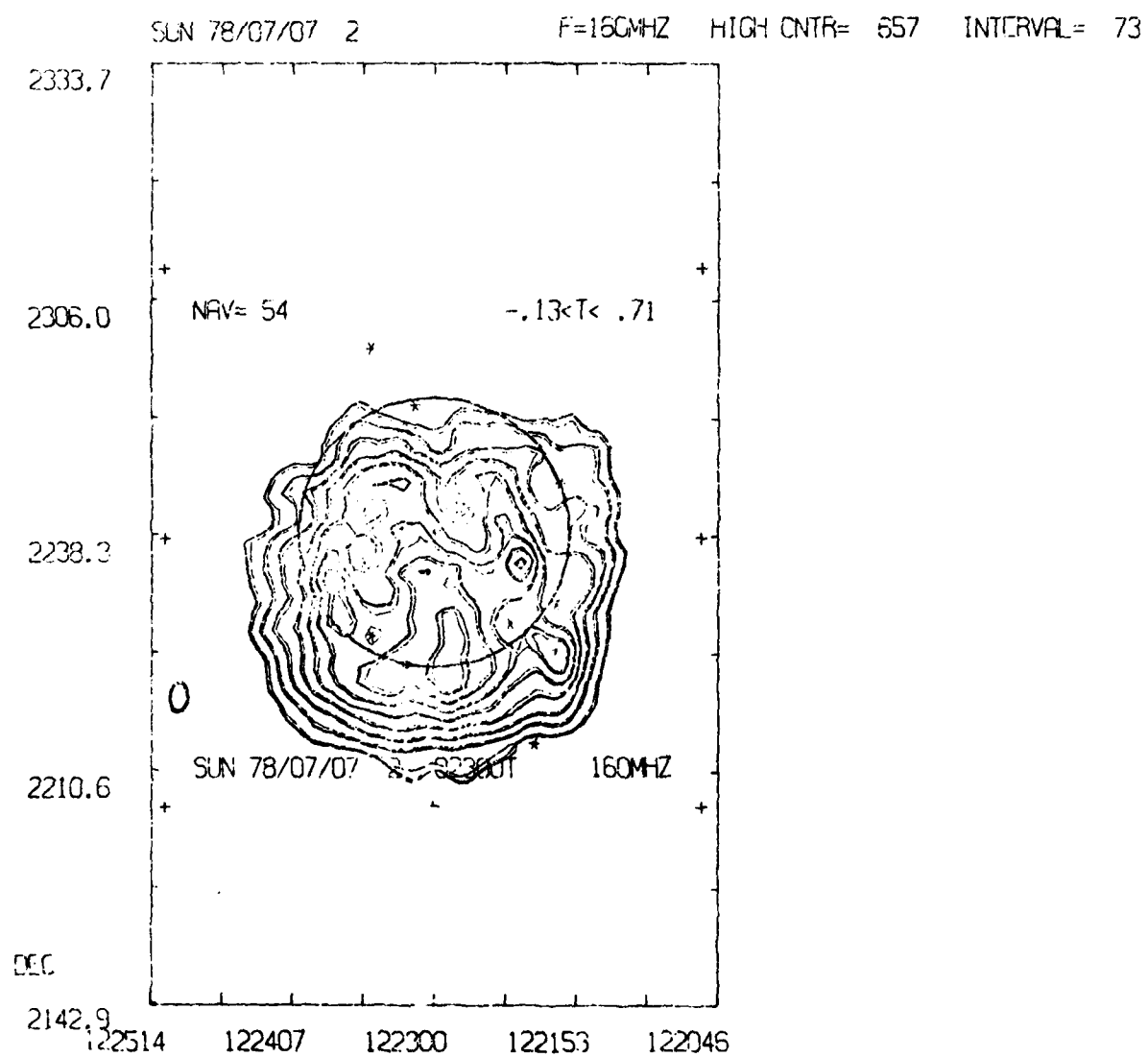
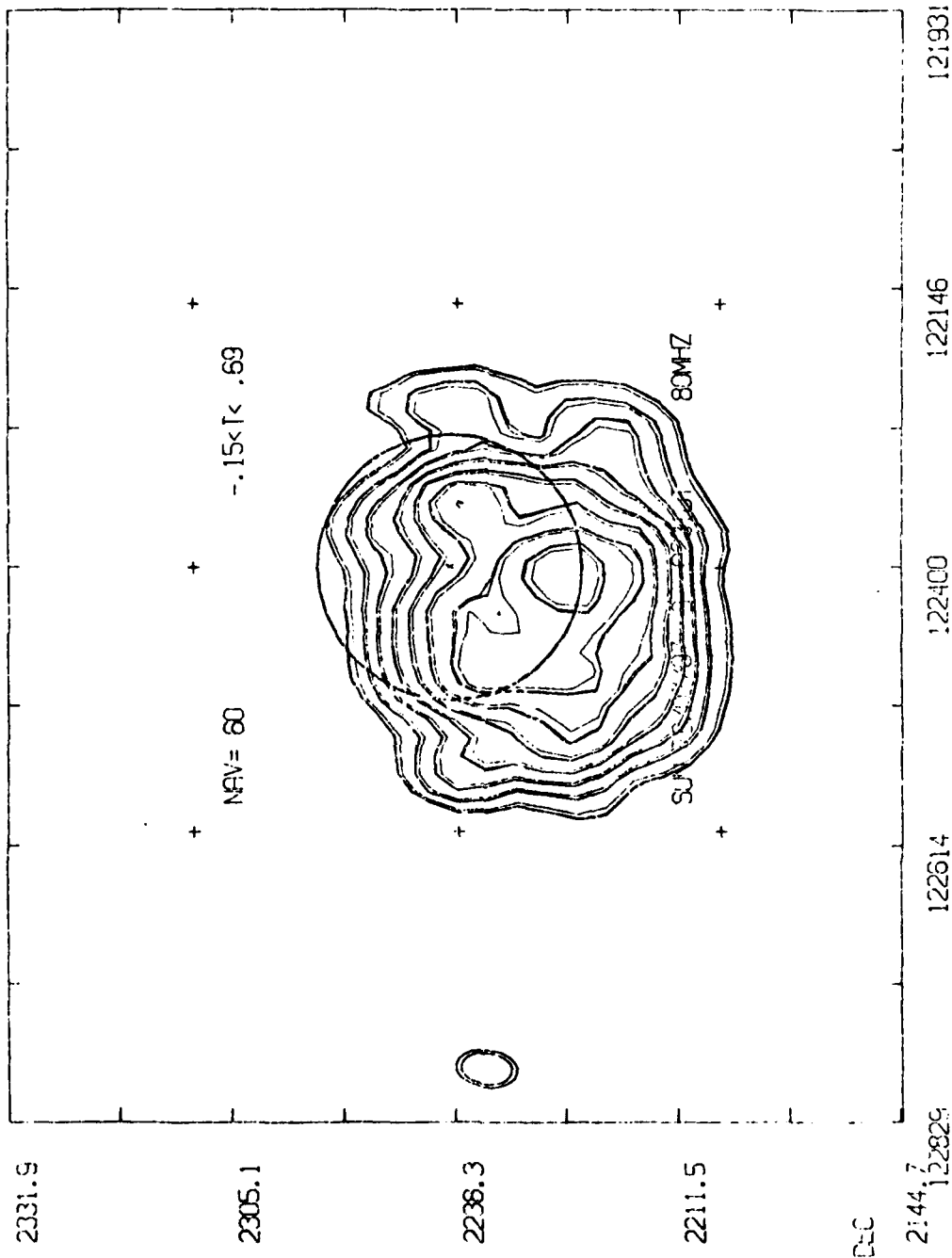


FIGURE 19

SUN 78/07/07 3 F=80MHZ HIGH CNTR= 337 INTERVAL= 37 23/10/76



UT/ST 02 31.59  
PROGRAM VERSION: 1978 JUL 14  
BEAM 7.5 4.5 -7. SPACE 34.0 28.8 -79. IMAX= 694976 (USING SSUN= 1.5 SFU)  
SS 34.4 23.7-77. SM= 375 SO= 488 SI= 20260 NAV= 60

FIGURE 20

regions, show very little contrast with the surrounding quiet area. Still, the active regions can be seen, as well as the suggestion of a slight depression corresponding to the position of the filament in the northeast. The Itapetinga maps at 0.70 cm for the first period were marred by spurious readings. We have cleaned up the map by interpolation to remove the spurious data, but the resultant maps show few features.

The Haystack 1.33 cm maps and the Itapetinga 1.39 cm maps both clearly show the active regions and the filament in the northeast. The Itapetinga maps were again marred by spurious data, but in regions where we can be sure the Itapetinga maps are reasonably clean, the features are quite consistent with the Haystack maps.

The La Posta 2.0 cm maps and the Haystack 1.93 cm maps are also quite consistent. Both show the active regions as strong enhancements and the filament as a slight depression. The Haystack maps also have a suggestion of a depression slightly east of the central meridian in the far south. The Sac Peak 10 map indicates the presence of a small filament in this region, which is probably the source of this depression.

The Arecibo maps at 11.5 cm and 21.4 cm show the active regions and the filament in the northeast quite clearly.

The long wavelength maps from the Culgoora Observatory (1.37 m and 3.75 m) show much less detail than the other radio maps. The active regions can be seen at both wavelengths, but at the shorter wavelength the maps are

confused by negative sidelobes from these active regions. An additional complication in interpreting these maps is that the sun was very low in the sky during these July observations at Culgoora. Refraction of these long wavelength radio waves through the earth's atmosphere displaces the radio image of the sun from the ephemeris position, making it difficult to determine the precise position of the observed features on the solar disk. Unfortunately these maps were only available in the form of finished contour maps and not in the form of data points. This made it impossible for us to re-contour the maps with emphasis on contours near the quiet sun level.

#### 4.3. Second Period Observations (July 15-18, 1978)

The coverage of the radio spectrum during the second period was more complete than for the first period. Table 4 lists the solar parameters for the four days of the second period and Table 5 lists the participating observatories, wavelengths, and the days each observatory made its observations. July 16 and 17 are the dates with the best coverage.

TABLE 4

##### Solar Parameters at 0000 UT

<u>DATE</u>	<u>L<sub>0</sub></u>	<u>B<sub>0</sub></u>	<u>P</u>
7-15	156	4.3	3.4
7-16	153	4.4	3.9
7-17	140	4.5	4.4
7-18	127	4.6	4.8

The Helium 10830 Å spectroheliogram for July 16 is shown

in Figure 21, and the Helium synoptic chart for the half Carrington rotation centered approximately on July 16 is shown in Figure 22. The outlines of the coronal holes are also shown as they were drawn by Jack Harvey, of the Kitt Peak Observatory, who kindly provided us with these maps. The helium data show a large coronal hole extending from the south pole toward the equator, a small hole at latitude  $10^{\circ}\text{S}$  and a somewhat larger hole at latitude  $40^{\circ}\text{N}$ . A number of active regions are also present.

TABLE 5

Participating Observatories - Second Period Observations

Observatory	Wavelength(cm)	July Date			
		15	16	17	18
La Posta	0.86	X	X	X	X
La Posta	2.00	X	X	X	X
Haystack	0.69	X	X	X	
Haystack	1.38	X	X	X	
Haystack	1.93	X	X	X	
Haystack	3.81	X	X	X	
Itapetinga	0.70	X	X	X	
Itapetinga	1.39	X	X	X	
Arecibo	11.5		X	X	X
Arecibo	21.4		X	X	X
Culgoora	187	X		X	
Culgoora	375	X	X	X	

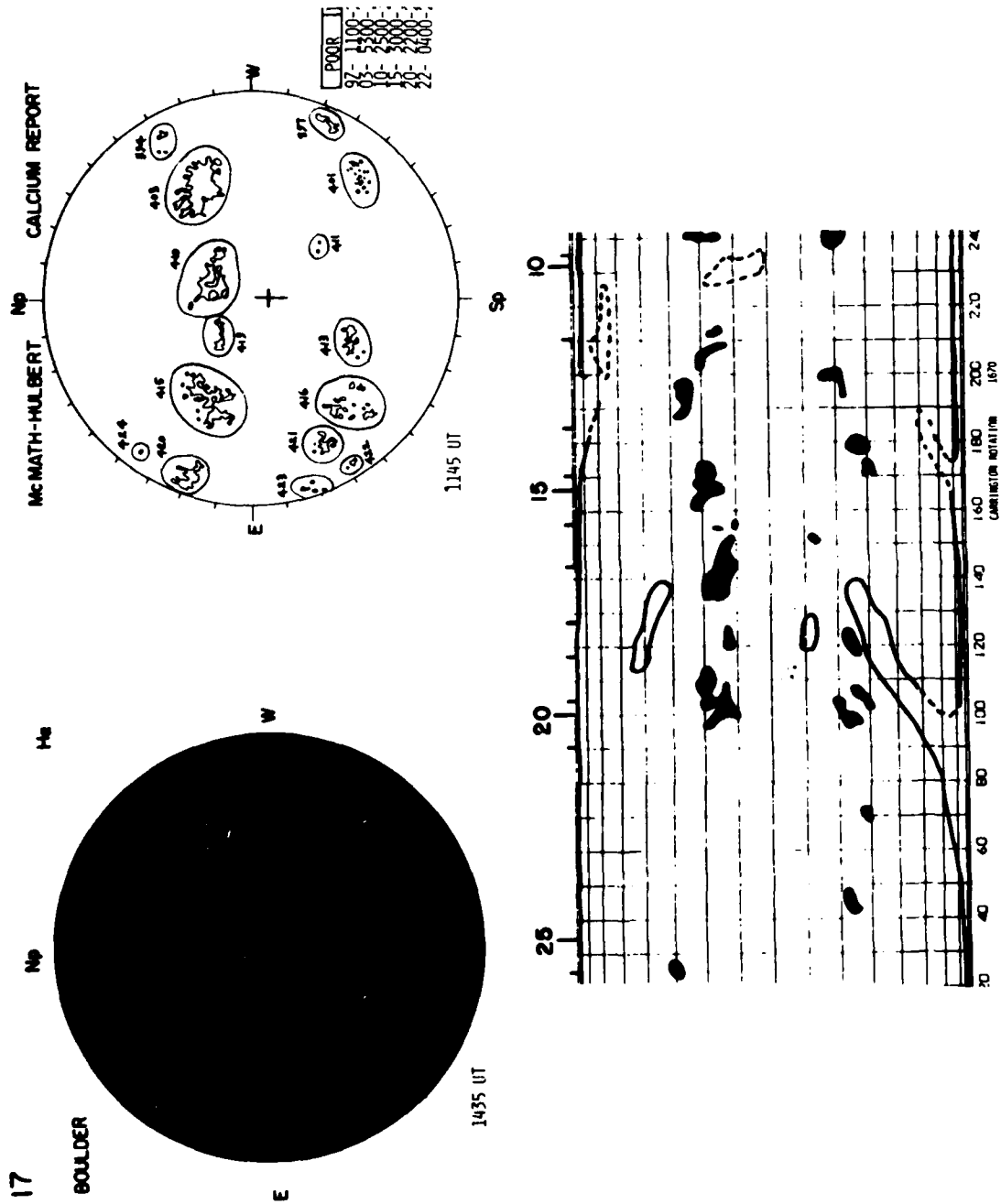
The Sac Peak  $H_{\alpha}$  picture (Figure 22) for July 16 also shows several strong active regions as well as several filaments. Also shown in Figure 22 is the McMath-Hulbert Calcium Report. The most prominent active region is McMath 15403.

The coronal hole in the south lies in a relatively quiet area of the sun which should make it easily detectable

at radio wavelengths. On the other hand, the coronal hole in the northern hemisphere lies very close to the large filament between McMath 15410 and McMath 15415, which makes it difficult to identify the coronal hole at radio wavelengths.



FIGURE 21





Radio Maps for July 15-18, 1978

Figures 23 - 44 show some of the maps for the second period observations. Special emphasis has been placed on the maps for the two days July 16 and July 17, since these two days represent the days for which we have the most complete wavelength coverage.

As with the first period maps, the shortest wavelength maps show little contrast. The Haystack 0.69 cm maps are virtually devoid of features other than the strong active regions. The Itapetinga maps at 0.70 cm show a distinct depression in the southern hemisphere corresponding in position to the coronal hole. In contrast, however, the 0.86 cm maps from La Posta show only the filament and coronal hole in the northeast as depressions.

The Haystack maps at 1.38 cm also show distinct differences from the Itapetinga maps at 1.39 cm. The Haystack maps show clear depressions in both the north and the south. In both cases, however, the position of the depression is shifted to the west of the position of the coronal hole as determined from the Helium 10830 Å charts. This apparent shift in the position had also been noted in previous observations (Wefer and Papagiannis, 1977).

The Haystack maps also show a depression on the east limb in the southern hemisphere. The H $\alpha$  pictures show several small filaments in this region of the east limb which are probably unresolved in the radio maps and show up as a single extended depression. The Itapetinga maps at 1.39 cm show only a slight suggestion of the depression in the

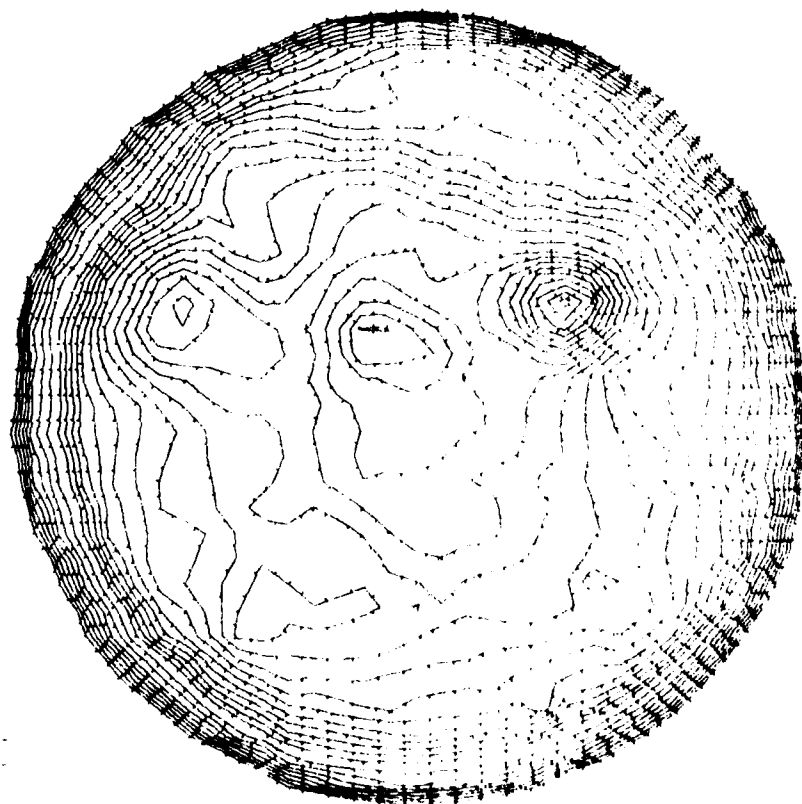


FIGURE 23

10.000.1378

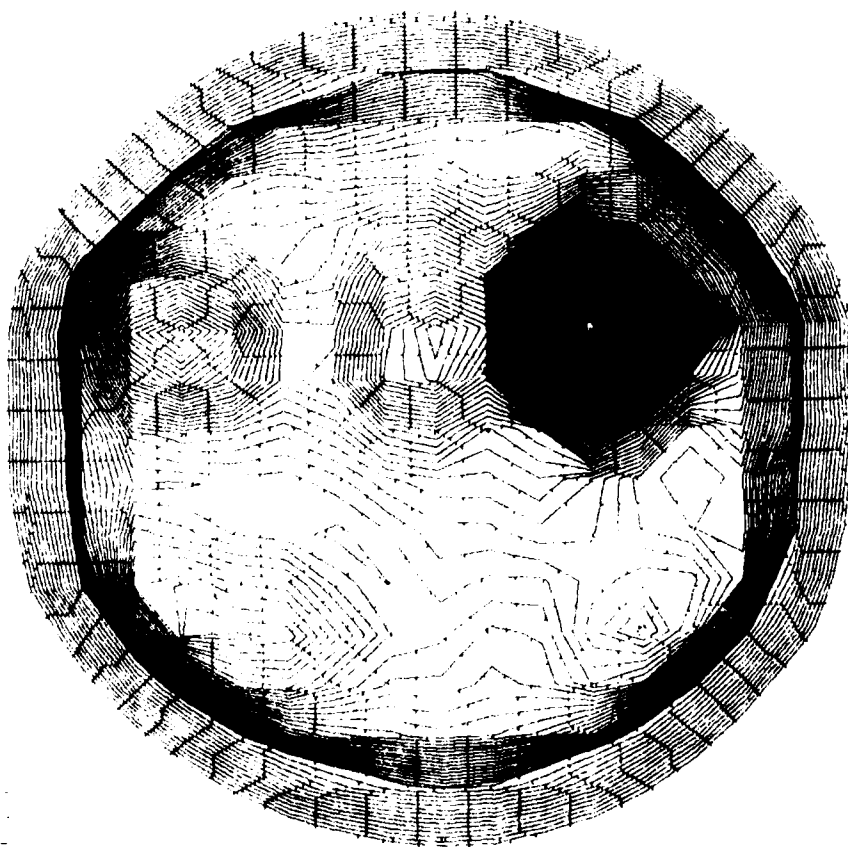


FIGURE 24

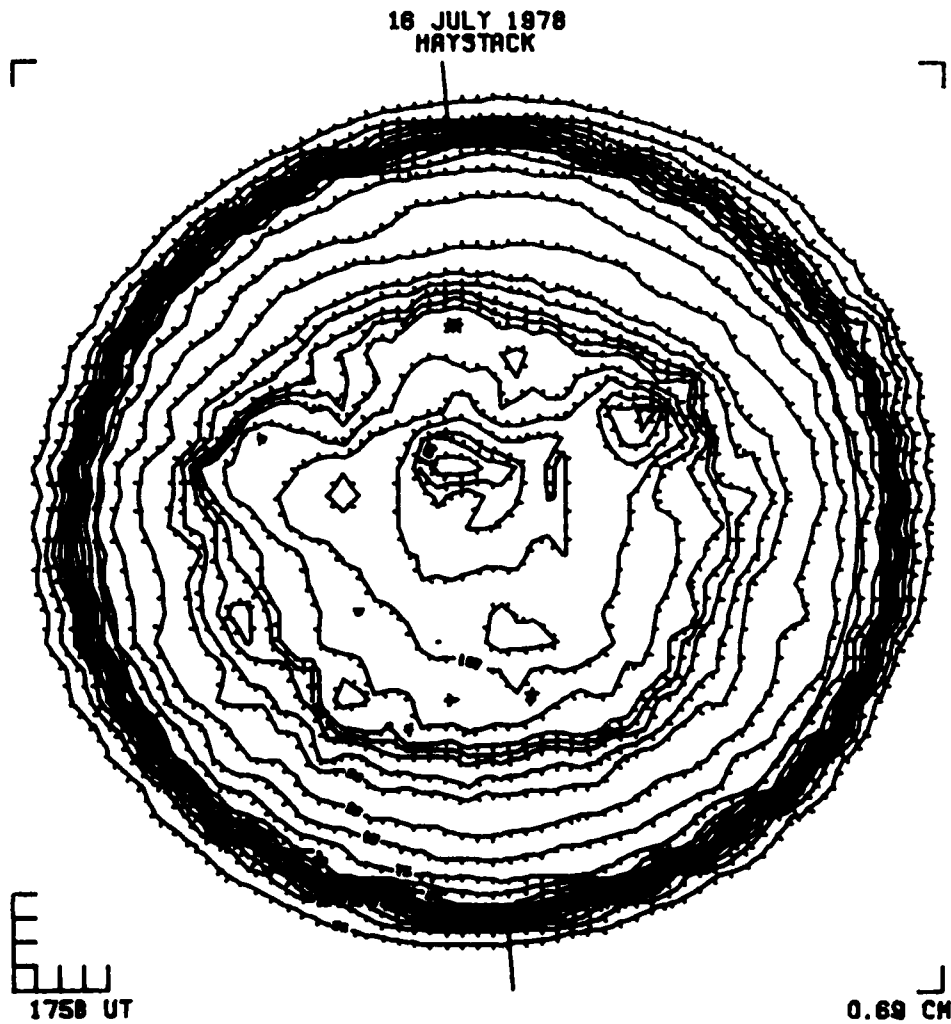


FIGURE 25

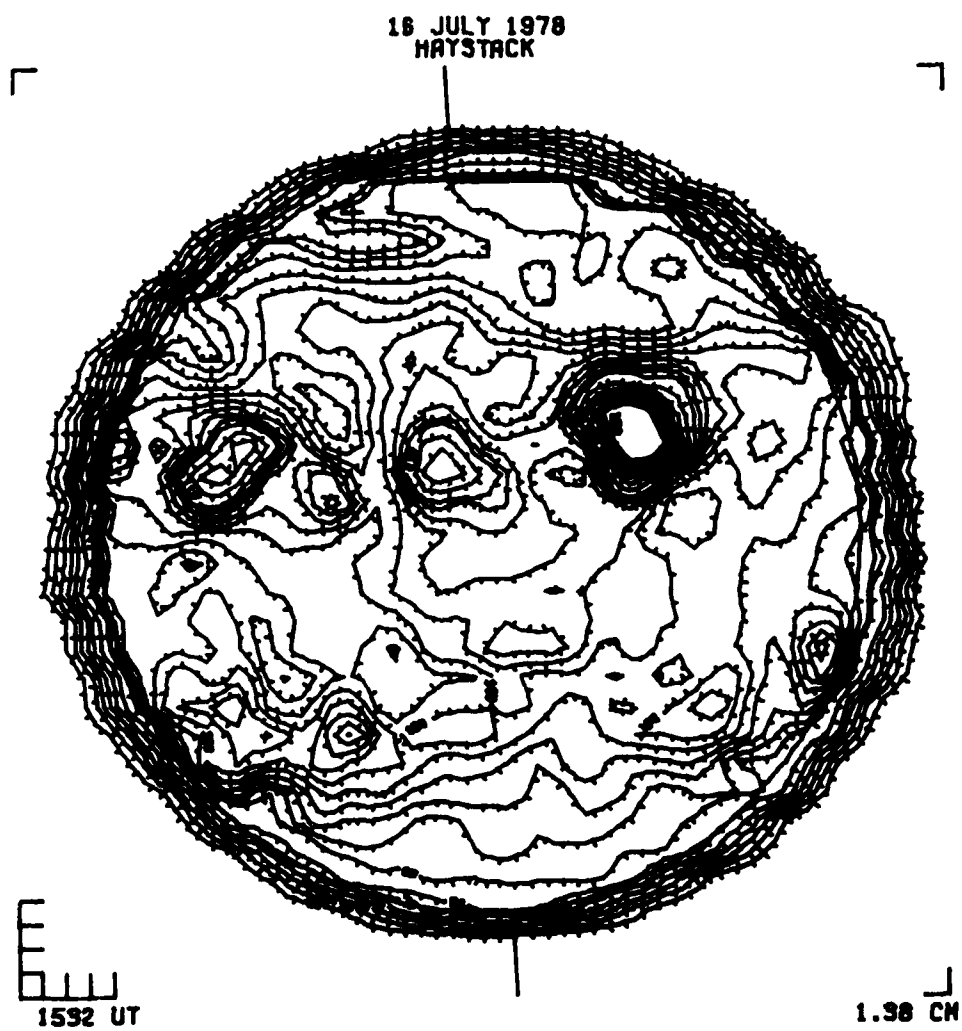


FIGURE 26

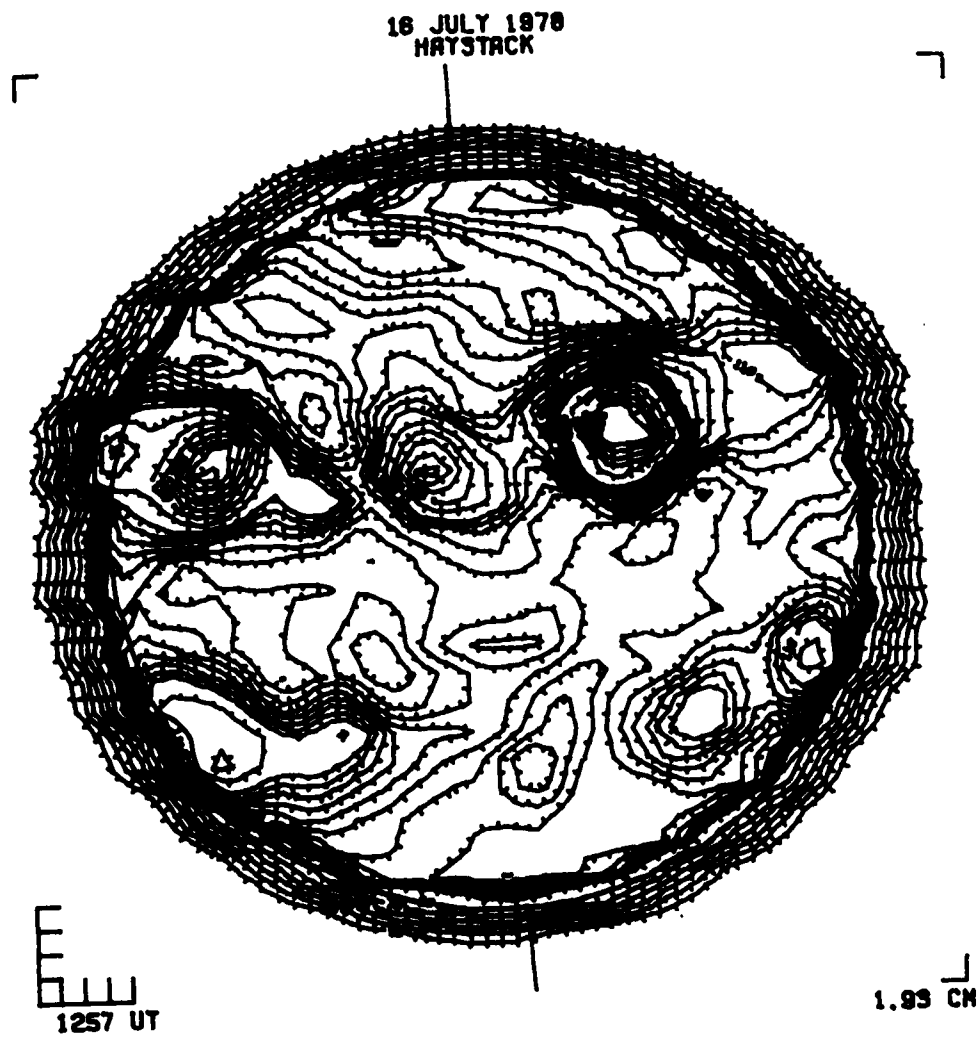


FIGURE 27

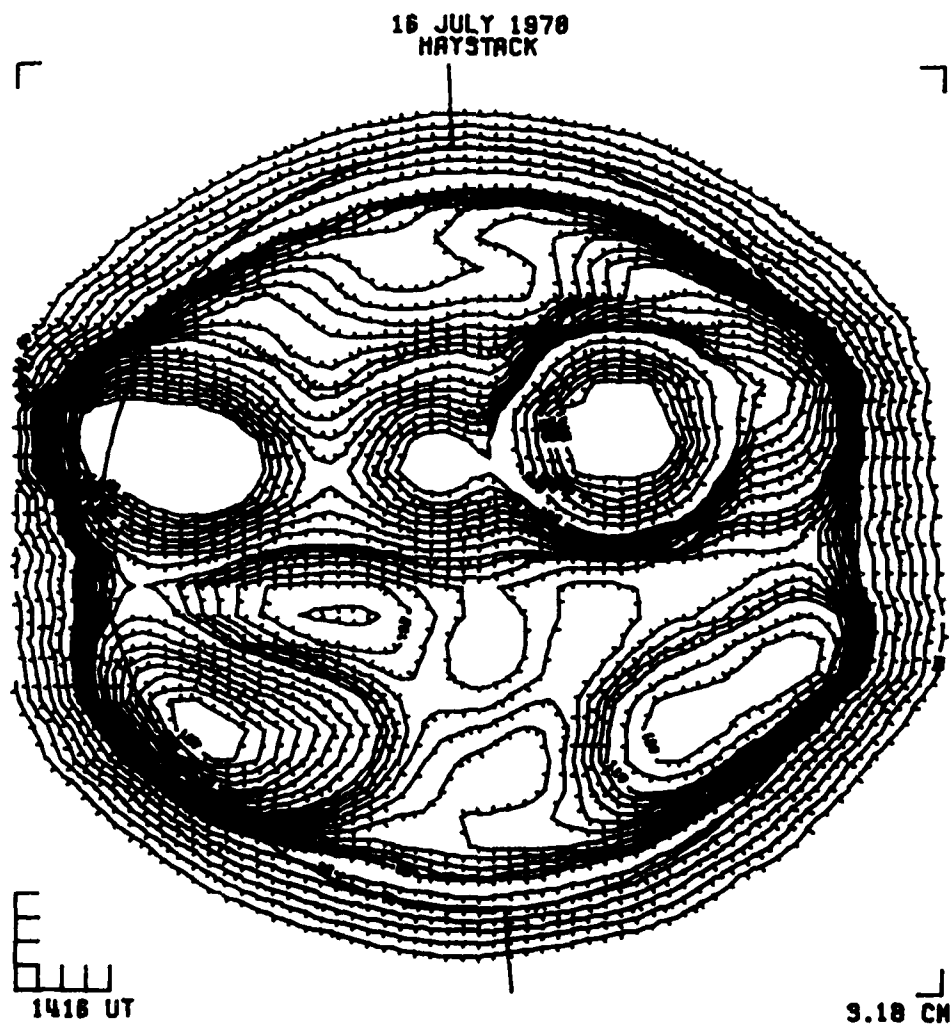


FIGURE 28

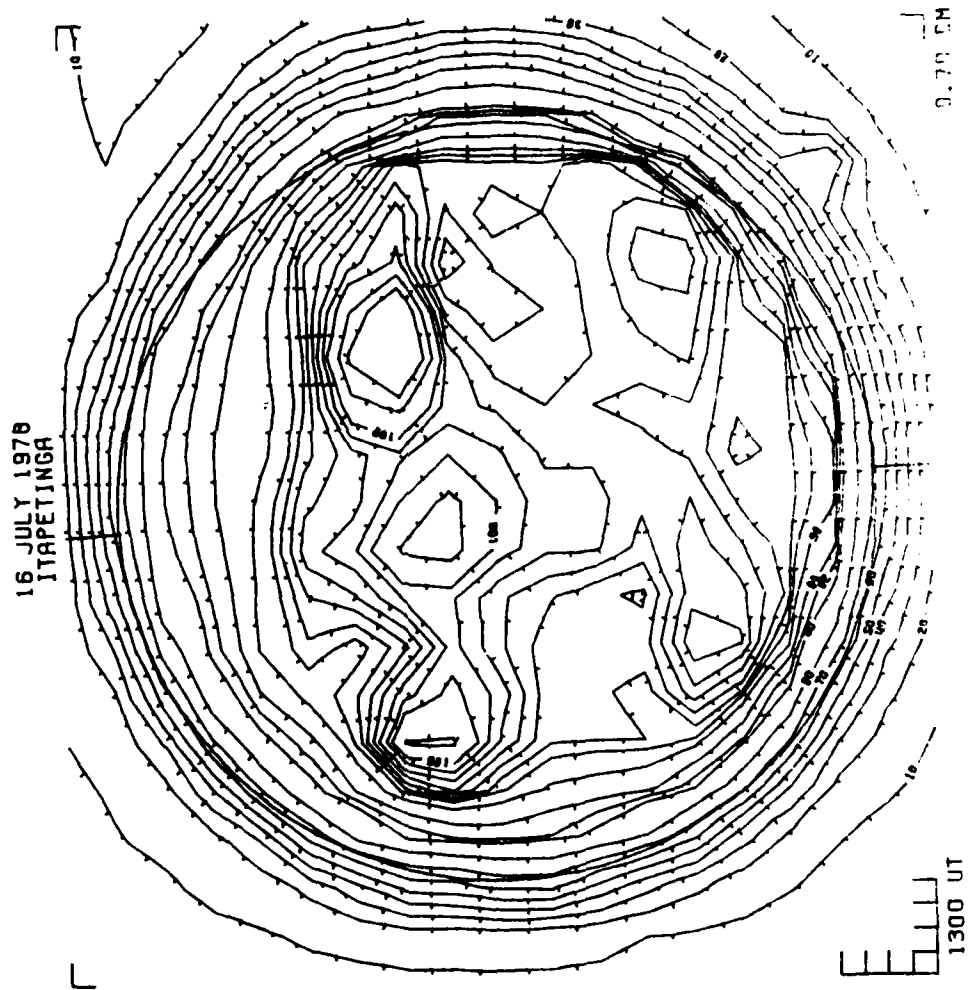


FIGURE 29



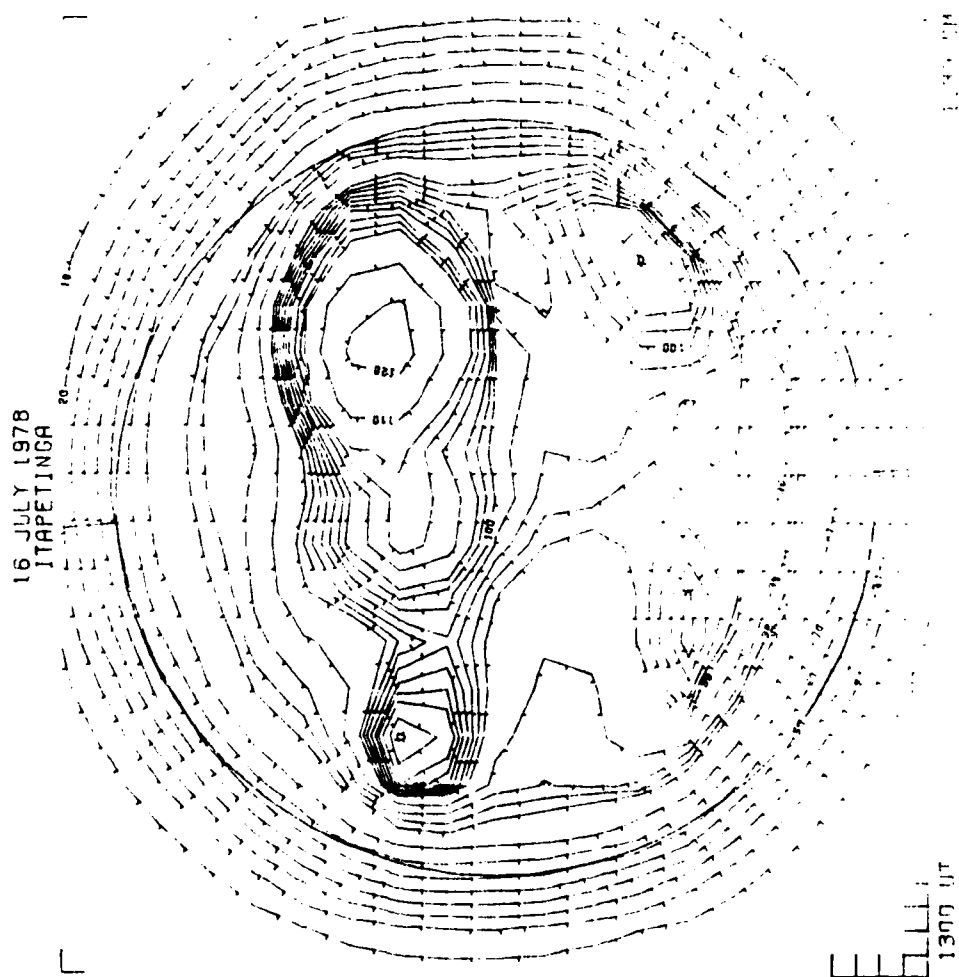


FIGURE 30

18 JULY 1978  
ARECIBO

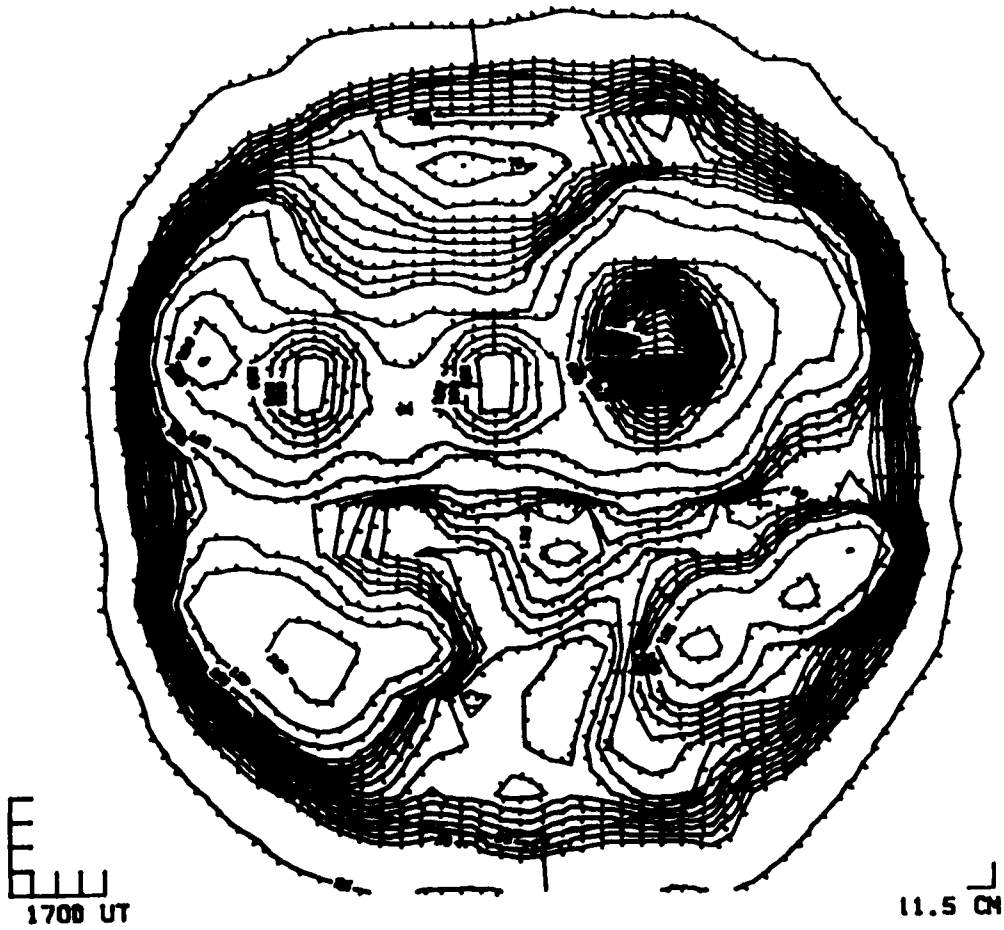


FIGURE 31

16 JULY 1978  
ARECIBO

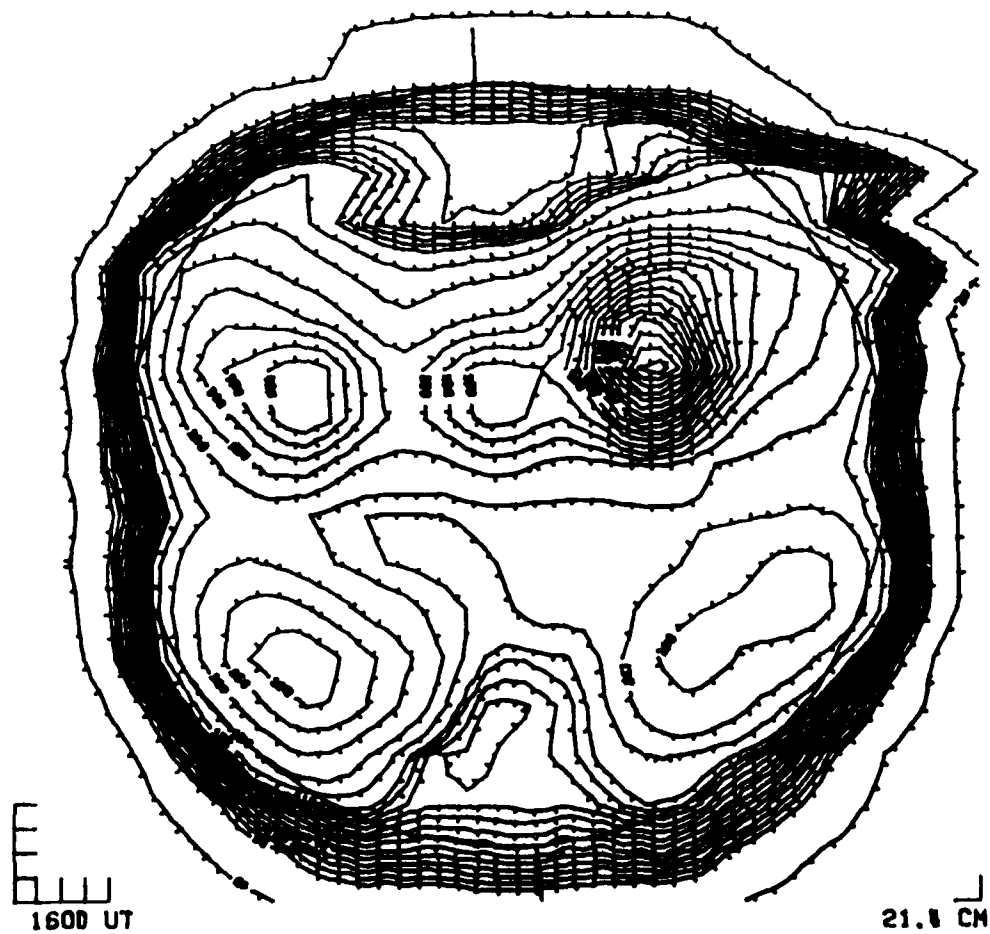


FIGURE 32

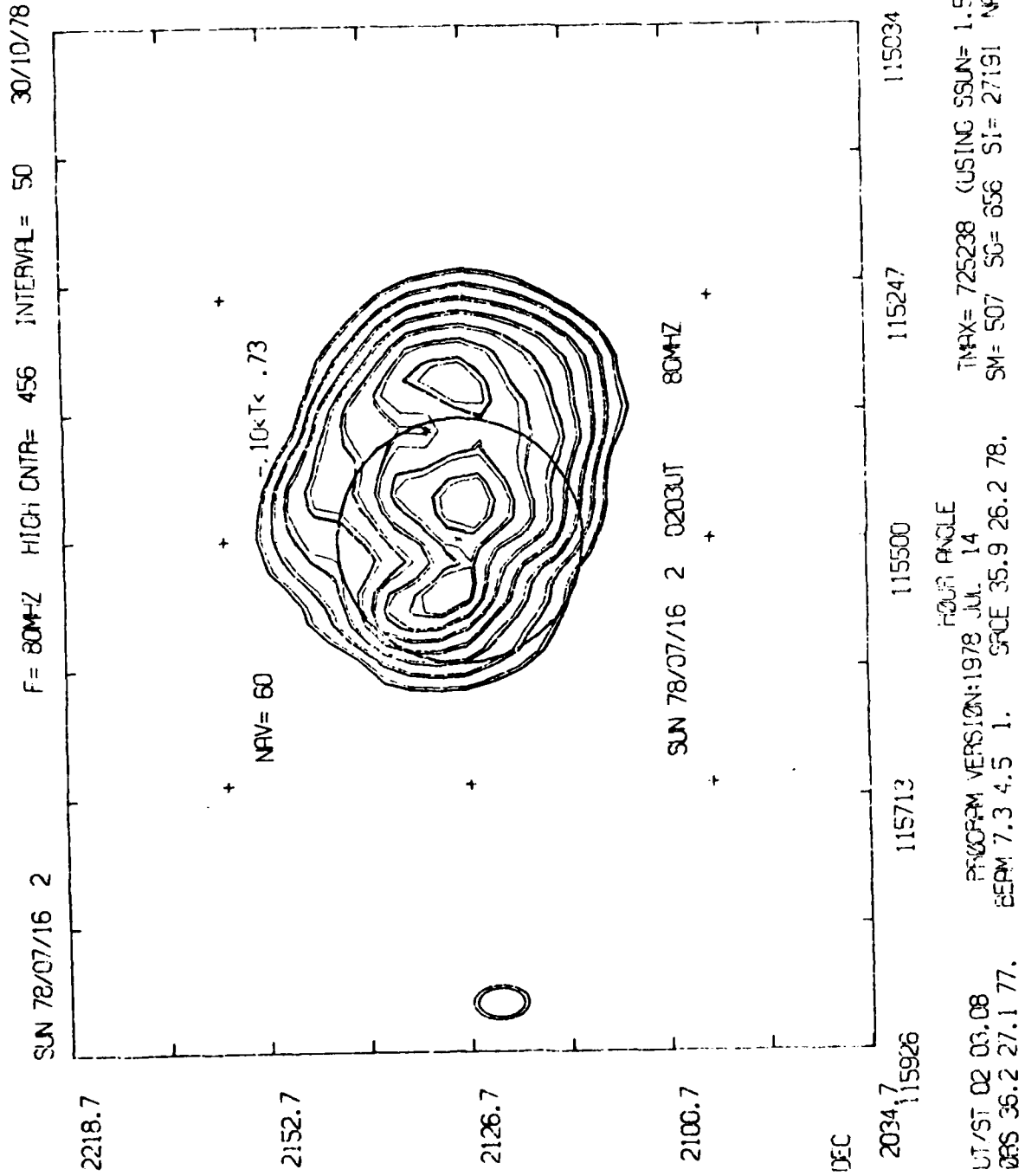
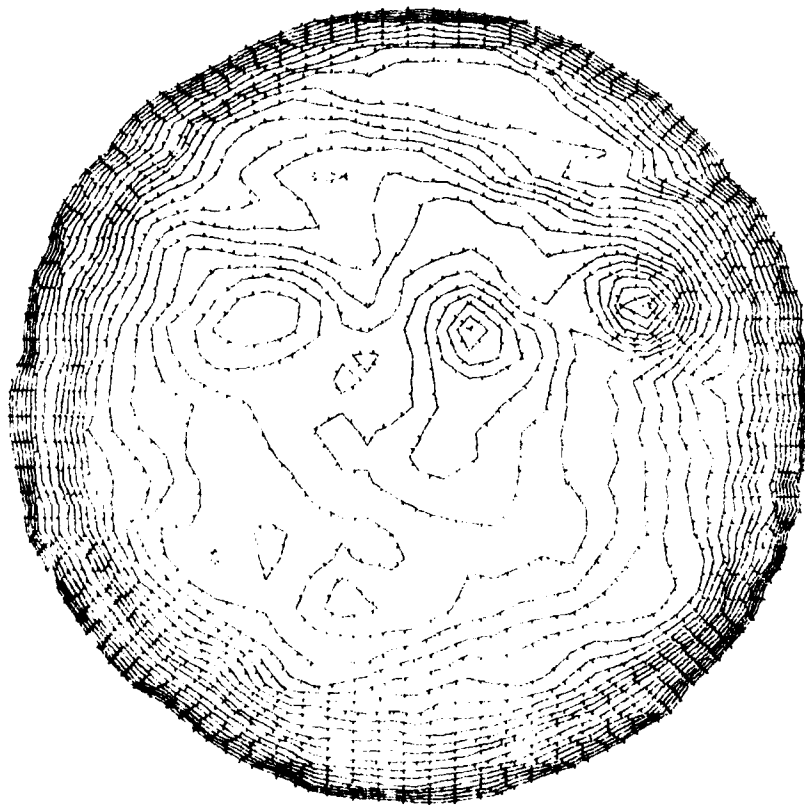


FIGURE 33

17. 10. 1. 74

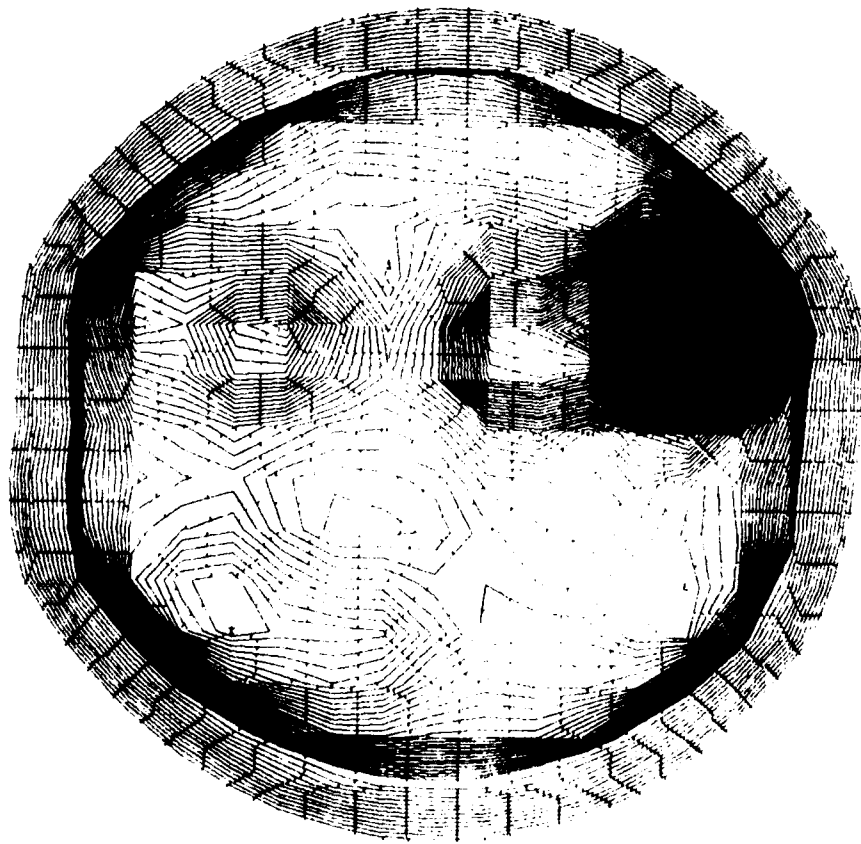


11. 11. 1. 74

9.1 MM

FIGURE 34

10 JUN 1973



10 JUN 1973  
13:24 UT

FIGURE 35

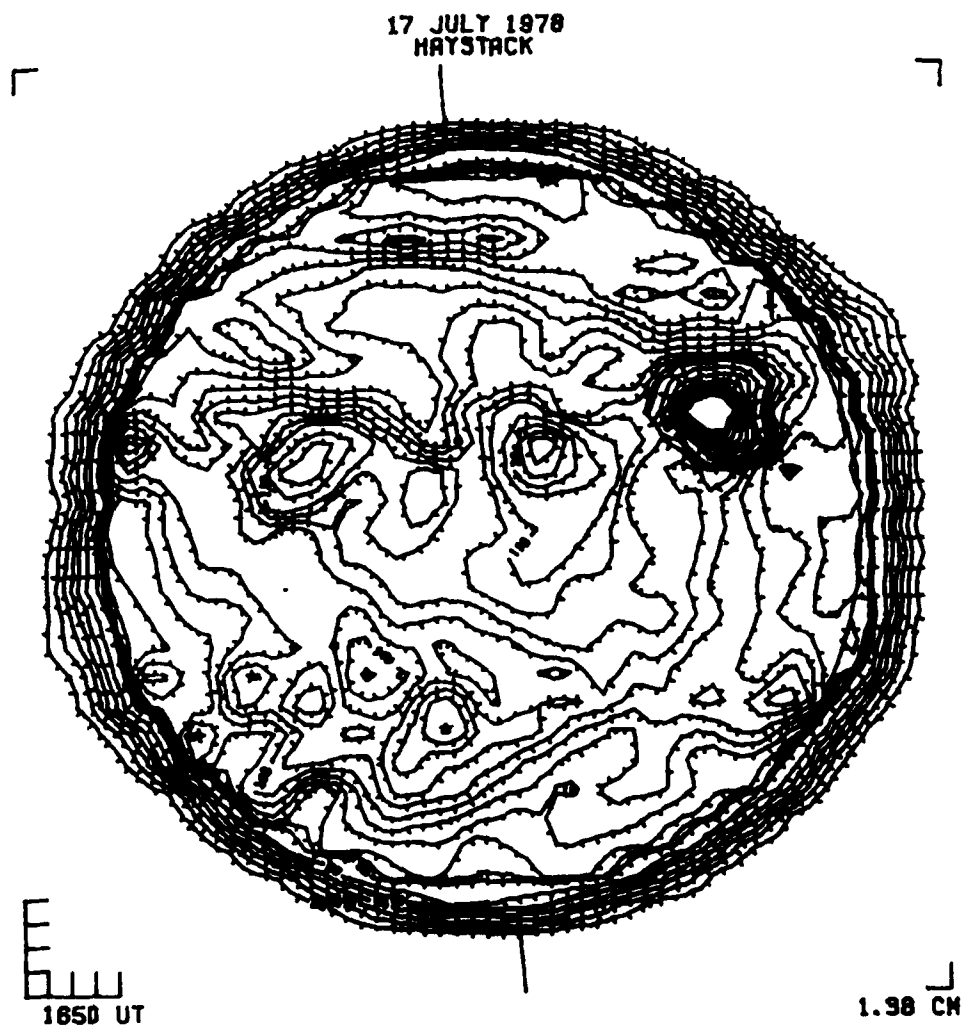


FIGURE 36

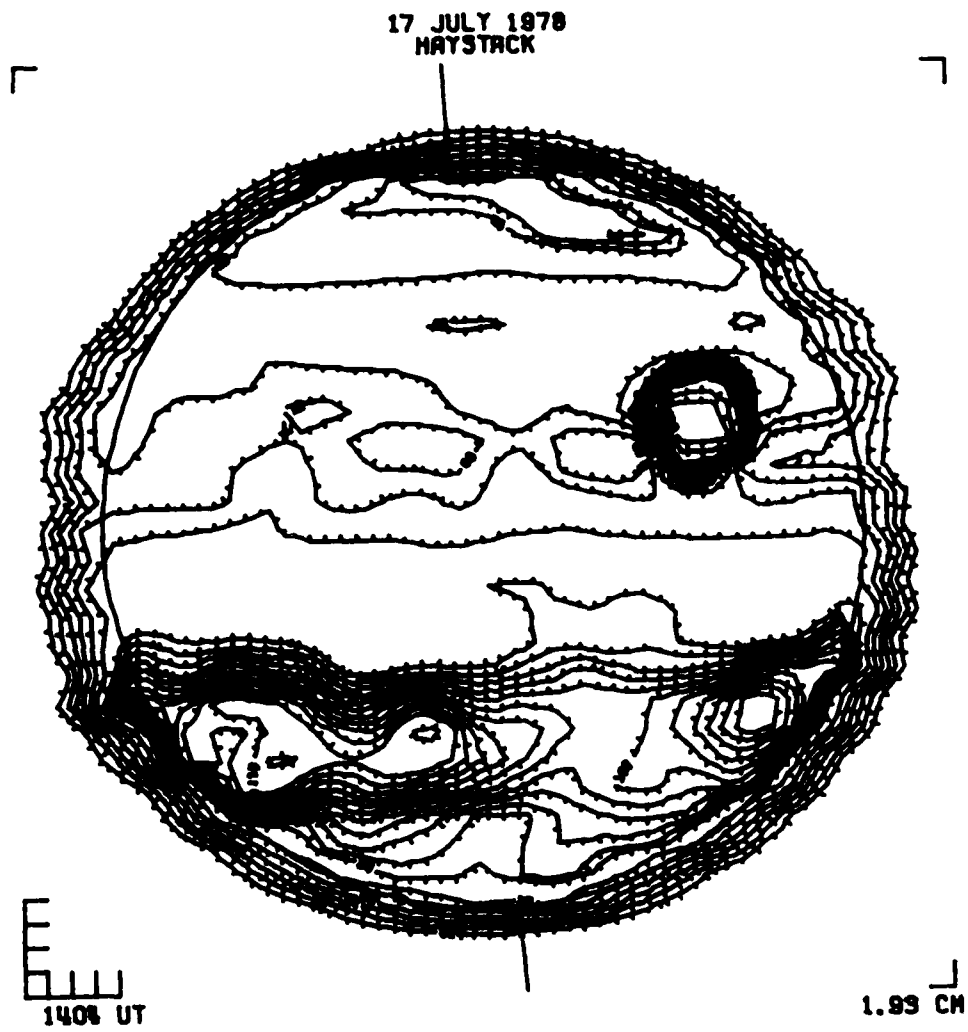


FIGURE 37



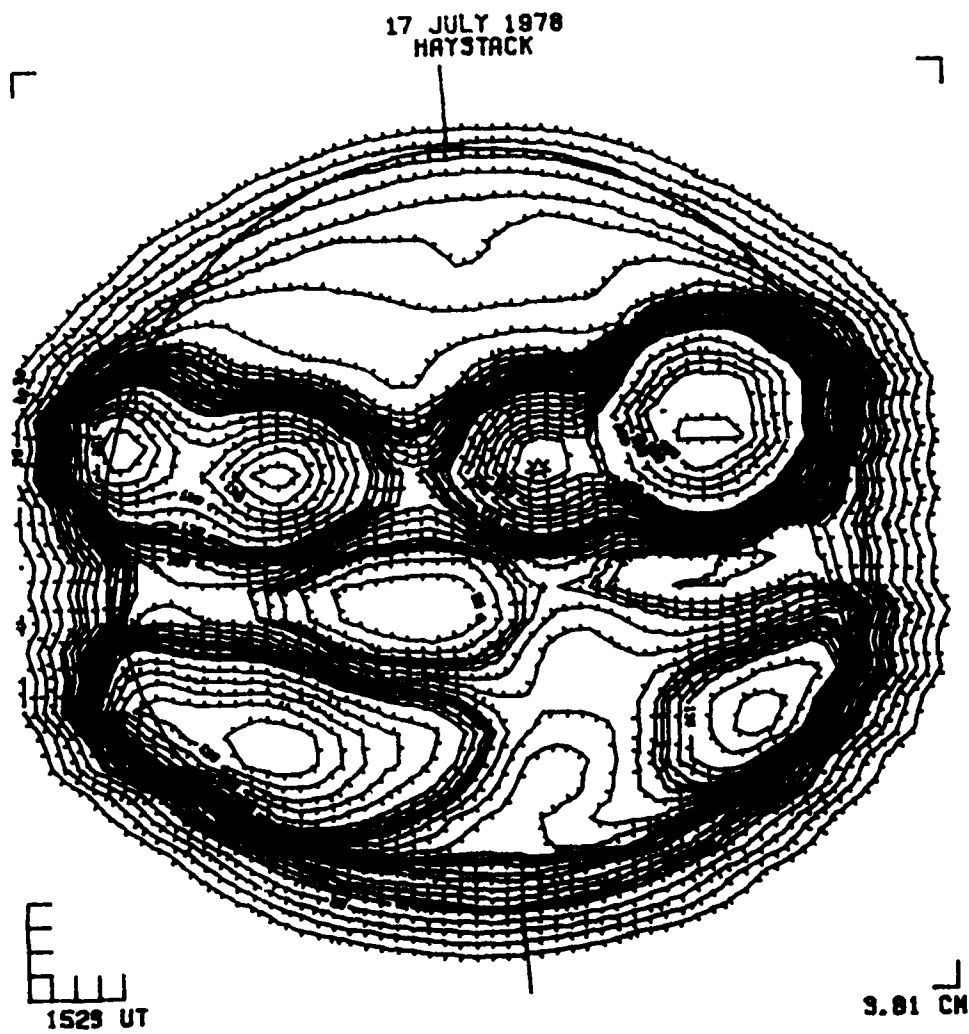


FIGURE 38

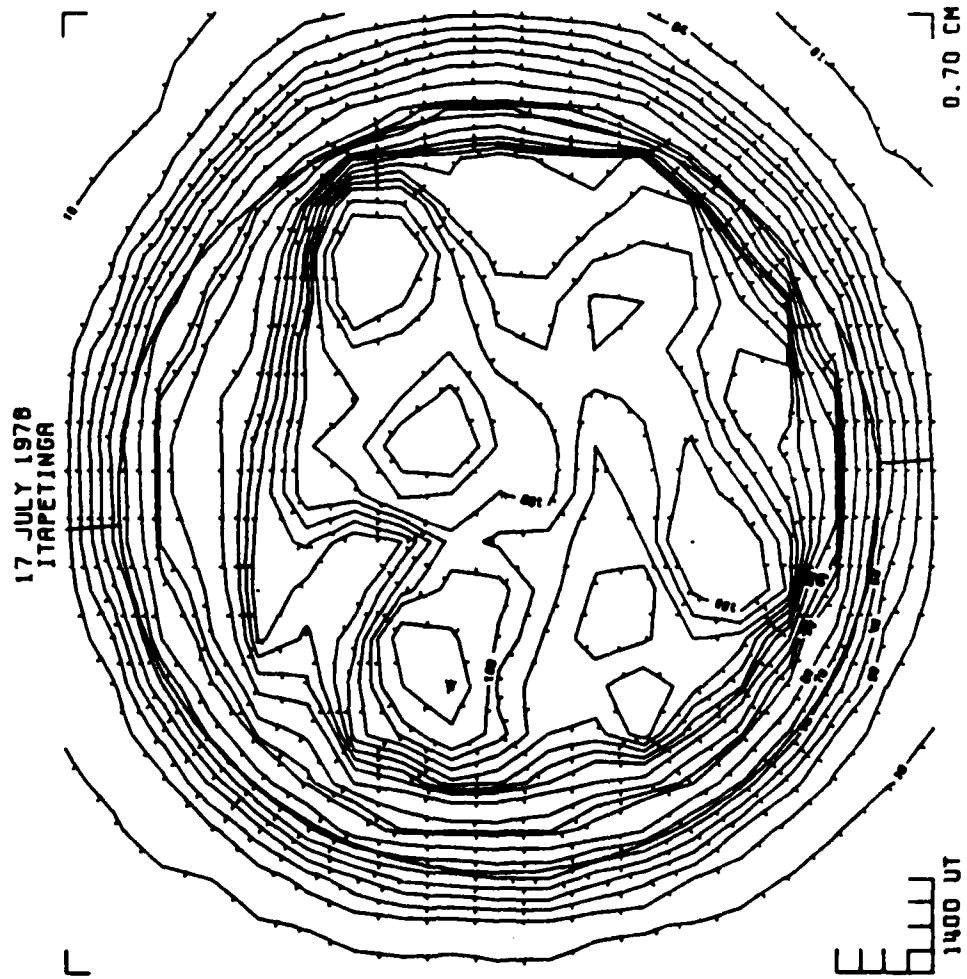


FIGURE 39

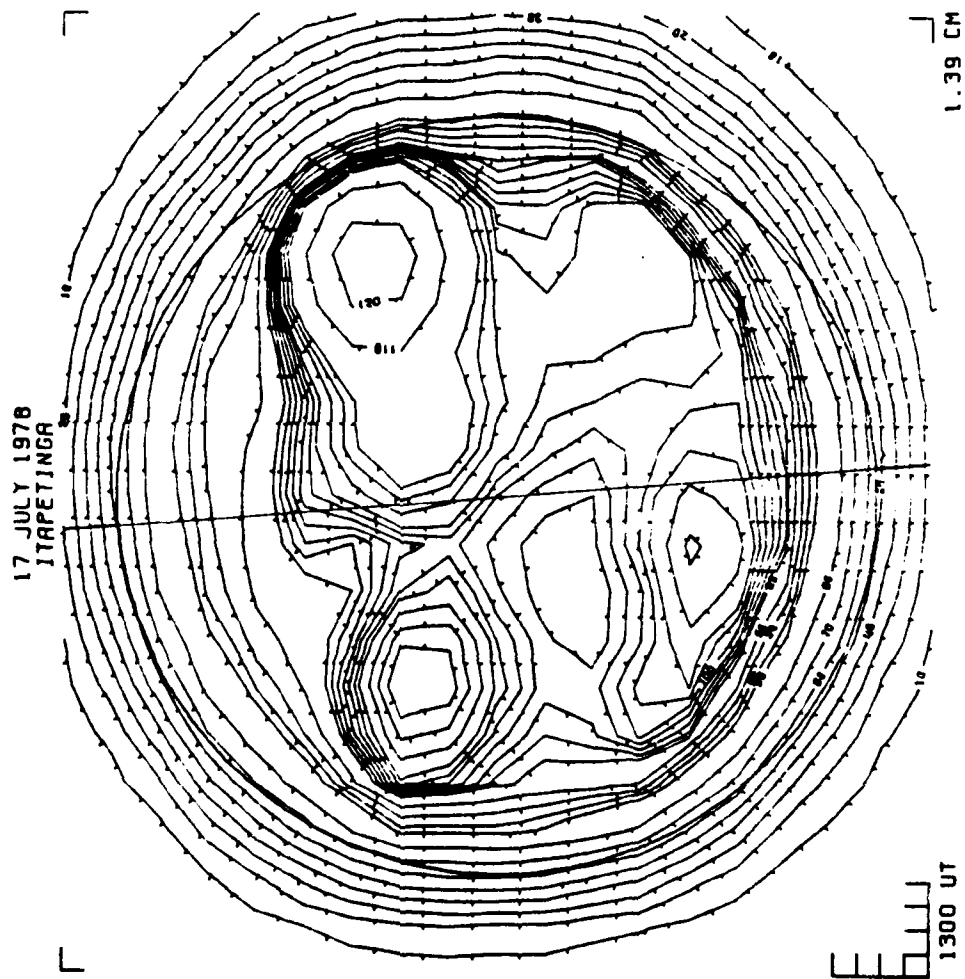


FIGURE 40

17 JULY 1978  
ARECIBO

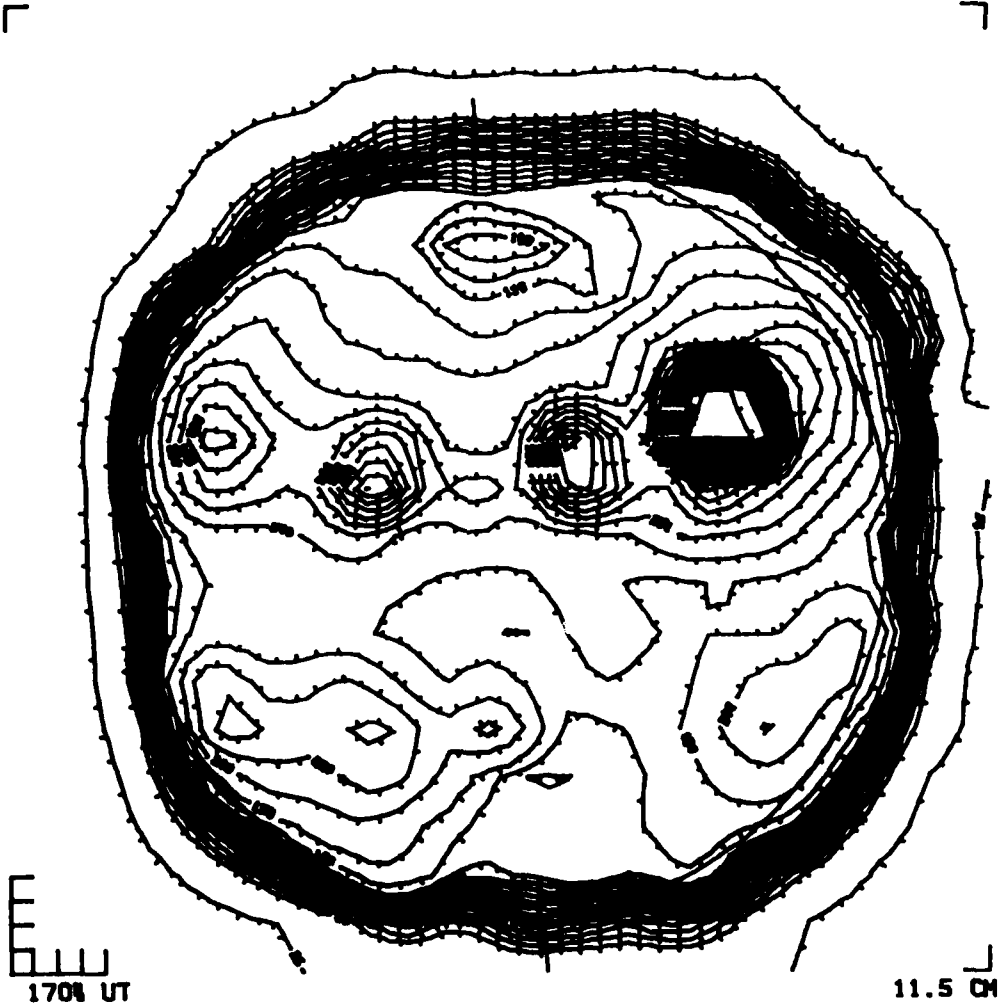


FIGURE 41

17 JULY 1978  
ARECIBO

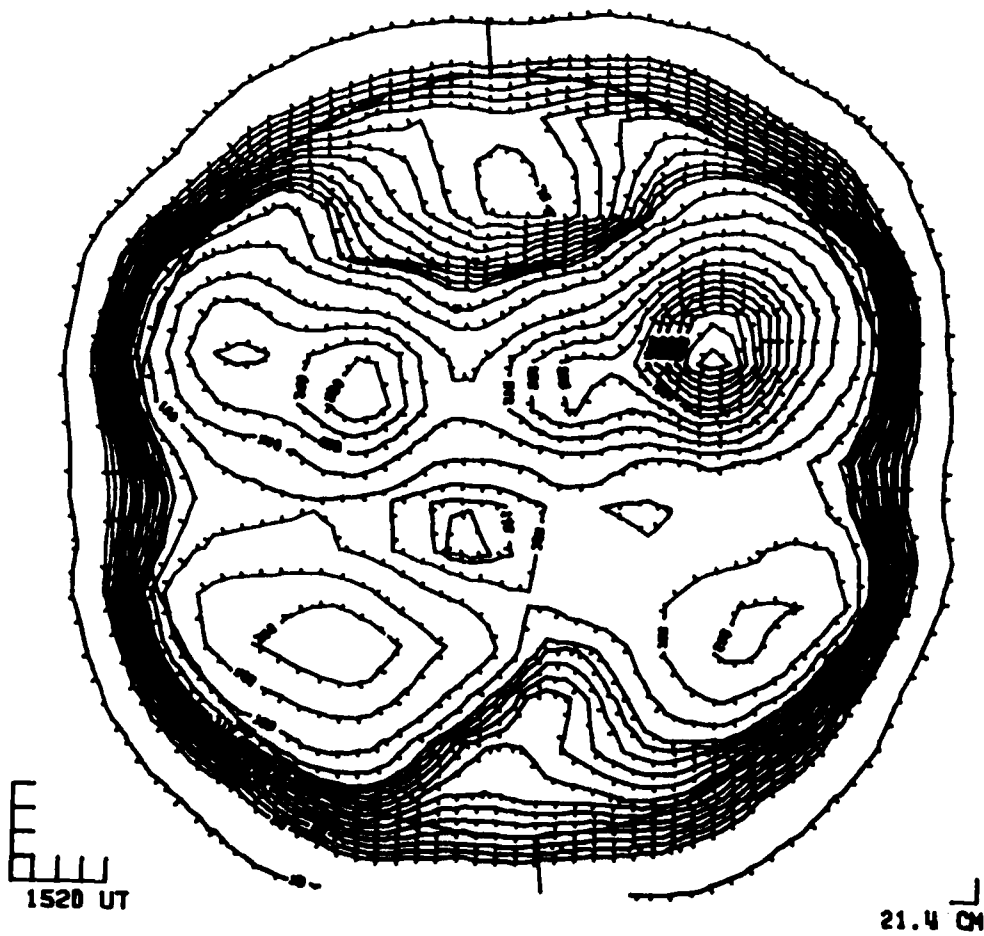


FIGURE 42

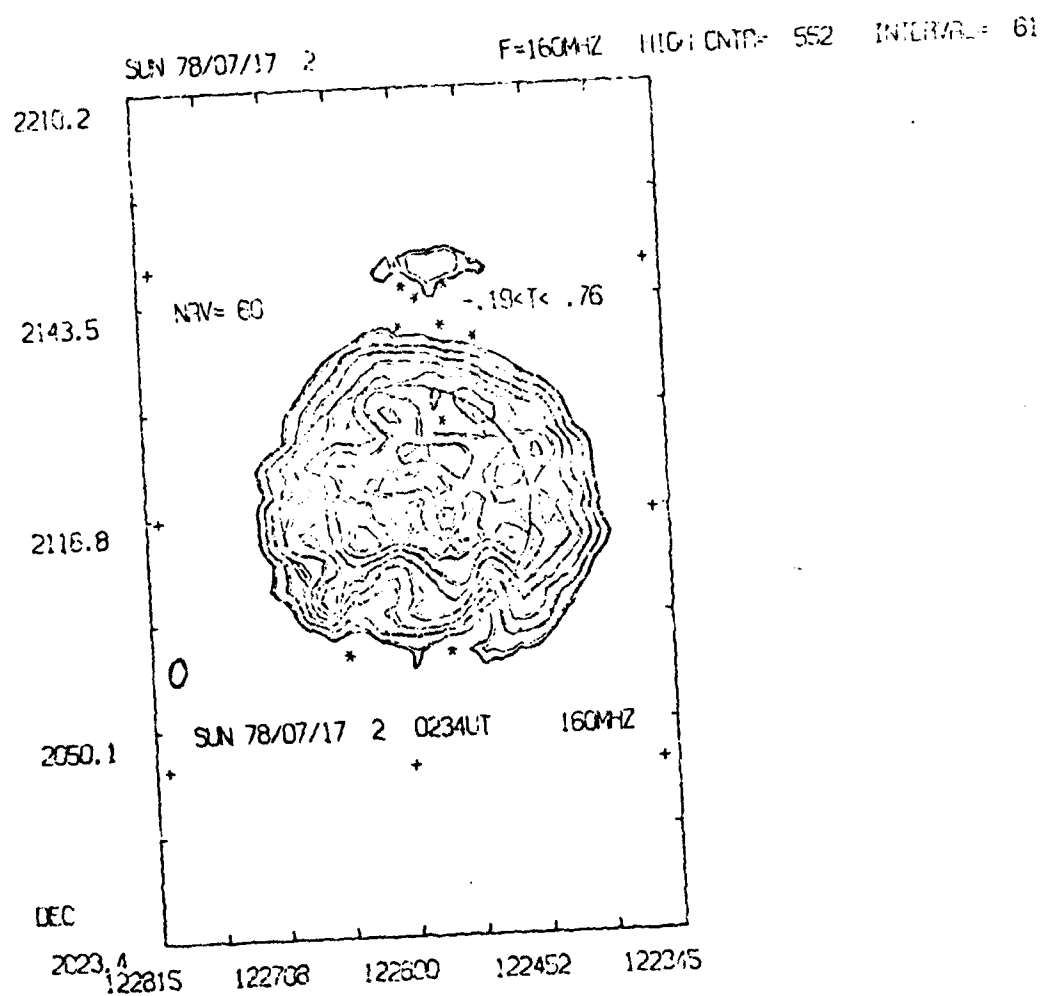


FIGURE 43

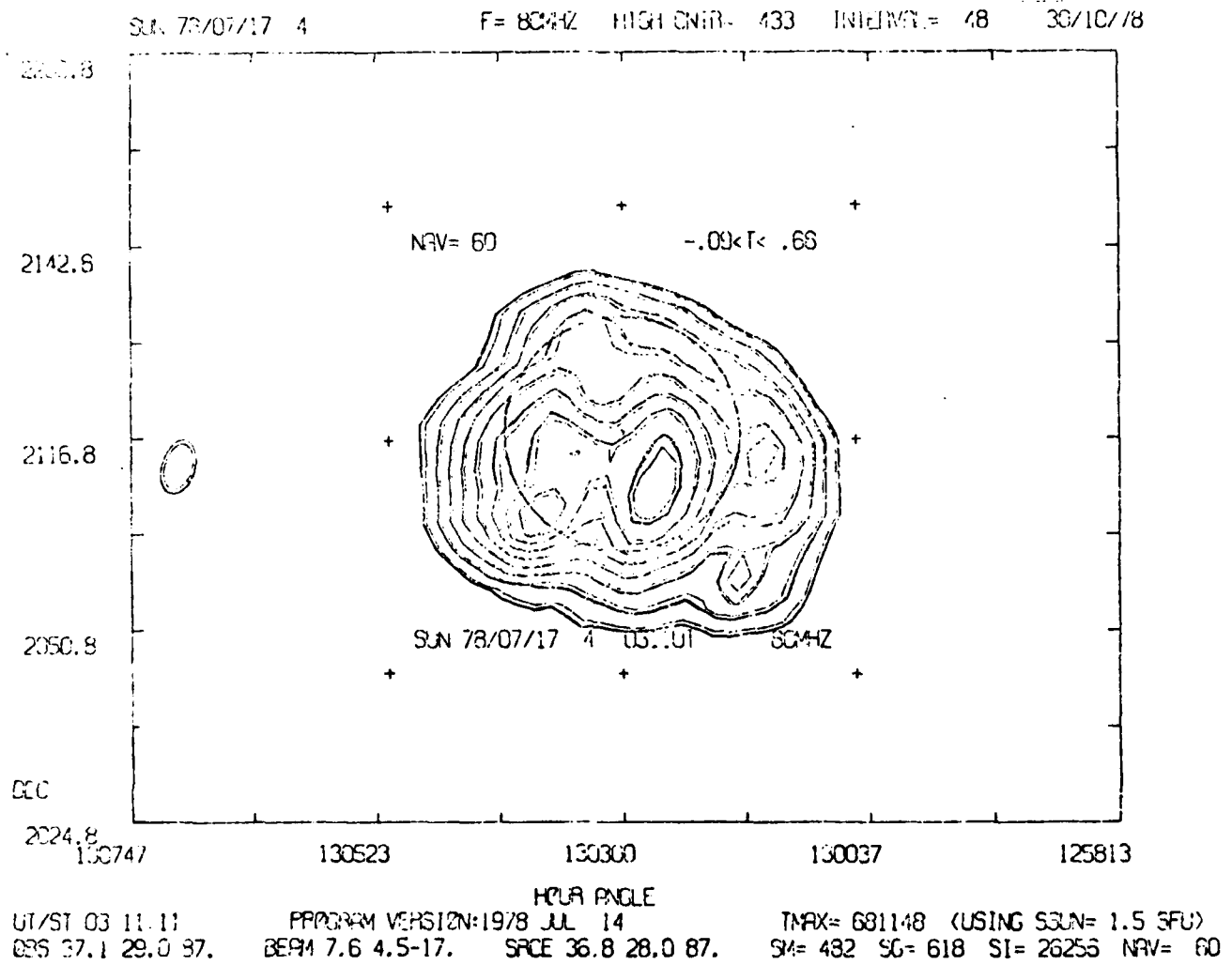


FIGURE 44

north, while the depression in the south appears to be merely an extension of the large depression coming from the east limb. Presumably the differences between the Haystack and Itapetinga maps reflects the difference in angular resolution of the two antennas. At Haystack the resolution is about 1.6 arcmin at 1.38 cm while at Itapetinga the resolution is only about 4 arcmin. Thus, the nearby active regions mask the coronal holes in the Itapetinga maps, whereas the Haystack antenna was able to resolve these as separate features.

The maps at 1.93 cm (Haystack) and 2.0 cm (La Posta) both show slight depressions corresponding to the coronal hole in the south. As with the 1.38 cm maps, the position of the coronal hole appears to be shifted to the west of its position in the Helium 10830 Å maps. Indeed, this westward shift is a consistent feature of the longer wavelength maps. In the north, the Haystack maps show the coronal hole as a distinct depression. Slightly west of the depression, however, is a small region of enhanced emission. This enhancement does not correspond to any clear features in the H $\alpha$  or Calcium spectroheliograms, but it does appear to be real.

The La Posta 2.0 cm maps indicate a slight enhancement in the region of the northern coronal hole. This disagreement between Haystack maps and La Posta maps may be the result of differences in angular resolution. The regions of enhanced emission seen in the Haystack maps as separate features are probably masking the slight depression of the



coronal hole in the La Posta maps. If slight enhancements near the boundary of a coronal hole are common features, this may explain the previous results of Wefer, et al. (1976), Wefer and Bleiweiss (1976), and our own results from 1977 (see Chapter 3), where coronal holes appeared as enhancements of about 1 - 2 % at 2.0 cm.

The Haystack maps at 3.81 cm show the usual active regions as well as the coronal holes in both the north and the south. As with the 1.93 cm maps, these maps show a small region of enhanced emission slightly to the west of the northern coronal hole.

The Arecibo maps at both 21.4 cm and 11.5 cm show both coronal holes quite clearly, including the eastward extension of the southern coronal hole. The depression on the east limb is also clearly visible as a separate feature. As before, the active regions are also prominent features.

As was the case during the first period observations, the Culgoora maps at 1.87 m and 3.75 m are more difficult to interpret than the other maps, due to the uncertainty about the position of the solar disk and the coarse contour intervals in the solar maps provided. At 3.75 m, the most prominent feature is the large bright region near the center, which is probably the strong active region McMath 15403. South of this feature is a slight depression which corresponds in position to the coronal hole. As usual, the 1.87 m maps show many more features than the 3.75 m maps. Again, sidelobes create major difficulties in interpreting these maps. There appear to be two regions of depressed

emission in the south, with the eastern one corresponding more closely in position to the coronal hole.

#### 4.4. The Spectra of the Second Period Coronal Holes

Determining a spectrum for a coronal hole is a rather difficult task when there are many active regions on the solar disk. The spectrum is actually the ratio of the brightness temperature inside the coronal hole at a particular wavelength to the brightness temperature that we would have observed in the same region if the coronal hole had not been present. The best approach for determining the values for the quiet sun is to measure the brightness temperature in a quiet area at the same distance from the center of the solar disk and at the same latitude as the coronal hole. Unfortunately, when there are many active regions present, such quiet areas become difficult to find, especially since the relatively large beamwidths of the antennas increase the area of the solar disk affected by the active regions.

This problem was especially acute during the second period, when two coronal holes, one in the northern and one in the southern hemisphere, were situated near the central meridian at approximately the same distance from the center of the solar disk. In addition, four active regions were nearly symmetrically arranged in the four quadrants of the solar disk. This made it unusually difficult to determine the appropriate quiet solar brightness temperatures, which introduced some additional uncertainty in the determination

of the radio spectra.

In this section we will determine the spectra of the two coronal holes, the one in the south and the one in the north, on two consecutive days, July 16 and 17. The determination of the brightness temperature ratio will be discussed for each map. The Toyokawa maps will not be used because severe sidelobe problems make them completely unreliable.

#### The Spectrum of the Northern Coronal Hole - July 16, 1978

The coronal hole in the north was an isolated hole, not connected to the polar coronal hole. Since this hole does not cover a wide range of latitudes, there is no point in trying to get a spectrum at several different points within the hole. Indeed, such an attempt would probably simply result in misinformation because near the boundary the antenna beams would be seeing as much area outside the area of the coronal hole as inside. We will therefore look for the point of maximum contrast.

In determining the spectrum of a coronal hole when we had two maps at very similar wavelengths we used the map with the higher resolution. Thus, we have chosen the Haystack map at 1.93 cm in preference to the La Posta 2.0 cm map and the Haystack maps at 1.38 cm and 0.69 cm in preference to the Itapetinga maps at 1.39 cm and 0.70 cm.

Table 6 lists the observatories; wavelengths; the quiet sun brightness temperatures,  $T_Q$  in relative units; the coronal hole brightness temperatures,  $T_h$  in the same units;

and the ratios of these two brightness temperatures for the northern coronal hole on July 16, 1978. The Culgoora map is difficult to interpret and the brightness temperature ratio at 375 cm must be treated with caution. The values obtained most likely represent a lower bound, and the spectral value at 375 cm could be considerably closer to 1.

TABLE 6  
Spectrum of the Northern Coronal Hole - July 16

<u>Observatory</u>	<u><math>\lambda</math>(cm)</u>	<u><math>T_q</math></u>	<u><math>T_h</math></u>	<u><math>T_h/T_q</math></u>
Culgoora	375	356	306	0.86
Arecibo	21.4	80	55	0.69
Arecibo	11.4	85	70	0.82
Haystack	3.81	100	92	0.92
Haystack	1.93	100	95	0.95
Haystack	1.38	99	97	0.98
La Posta	0.86	36.5	36	0.99
Haystack	0.69	85	85	1.00

Of particular interest are the Haystack observations. The region in the northern hemisphere corresponding most closely to the coronal hole, as determined from the 10330 Å Helium maps and the Arecibo radio maps, is a region of distinctly lower brightness than the quiet sun level. However, at the northeastern boundary of the coronal hole region the 3.81 cm map shows the suggestion of an enhancement. Furthermore, at 1.93 cm and 1.38 cm these regions appear as very distinct enhancements approximately

2-3 % brighter than the expected quiet sun level. This enhancement is consistent with that previously reported by Wefer, et al. (1976) and Wefer and Papagiannis (1977) for coronal holes around 2 cm. Since the spatial resolution of the La Posta telescope used by Wefer et al. is much poorer than the Haystack telescope, it is conceivable that what was being observed were similar small enhancements near the coronal hole boundaries. Although no plage area can be seen in the neighborhood of this enhancement, it is quite possible that near the boundaries of a coronal hole, closed magnetic field lines lead to higher densities and hence in some cases to regions of slightly enhanced emission.

#### The Spectrum of the Northern Coronal Hole - July 17, 1973

On July 17, we have an additional map from Culgoora, Australia, but we are missing the 0.69 cm map from the Haystack observatory. The Culgoora 160 MHz map is complicated by sidelobe problems, which make it impossible to locate the coronal holes unambiguously and to determine a relative brightness temperature for them.

Table 7 presents the results for July 17. The spectrum is quite consistent with the results of July 16. The contrast appears to be slightly greater at 11.5, 3.81, and 1.38 cm, but the error bars for these measurements are about 2-3% so these differences are not serious. We note again that the coronal hole appears as a depression at 1.93 cm and again there are two small enhancements (about 2-3%) near the northeastern boundary of the coronal hole.

TABLE 7

Spectrum of the Northern Coronal Hole - July 17

<u>Observatory</u>	<u><math>\lambda</math>(cm)</u>	<u><math>T_q</math></u>	<u><math>T_h</math></u>	<u><math>T_h/T_q</math></u>
Culgoora	375	337	289	0.86
Arecibo	21.4	80	55	0.69
Arecibo	11.5	85	65	0.76
Haystack	3.81	100	87	0.87
Haystack	1.93	100	95	0.95
Haystack	1.38	100	95	0.95
La Posta	0.86	36	35.5	0.99
Itapetinga	0.70	96	95	0.99

Figure 45 shows the spectra for the northern coronal hole for both days. The solid line is the spectrum for July 16, while the dashed line is the spectrum for July 17. The error bars were estimated directly from the maps.

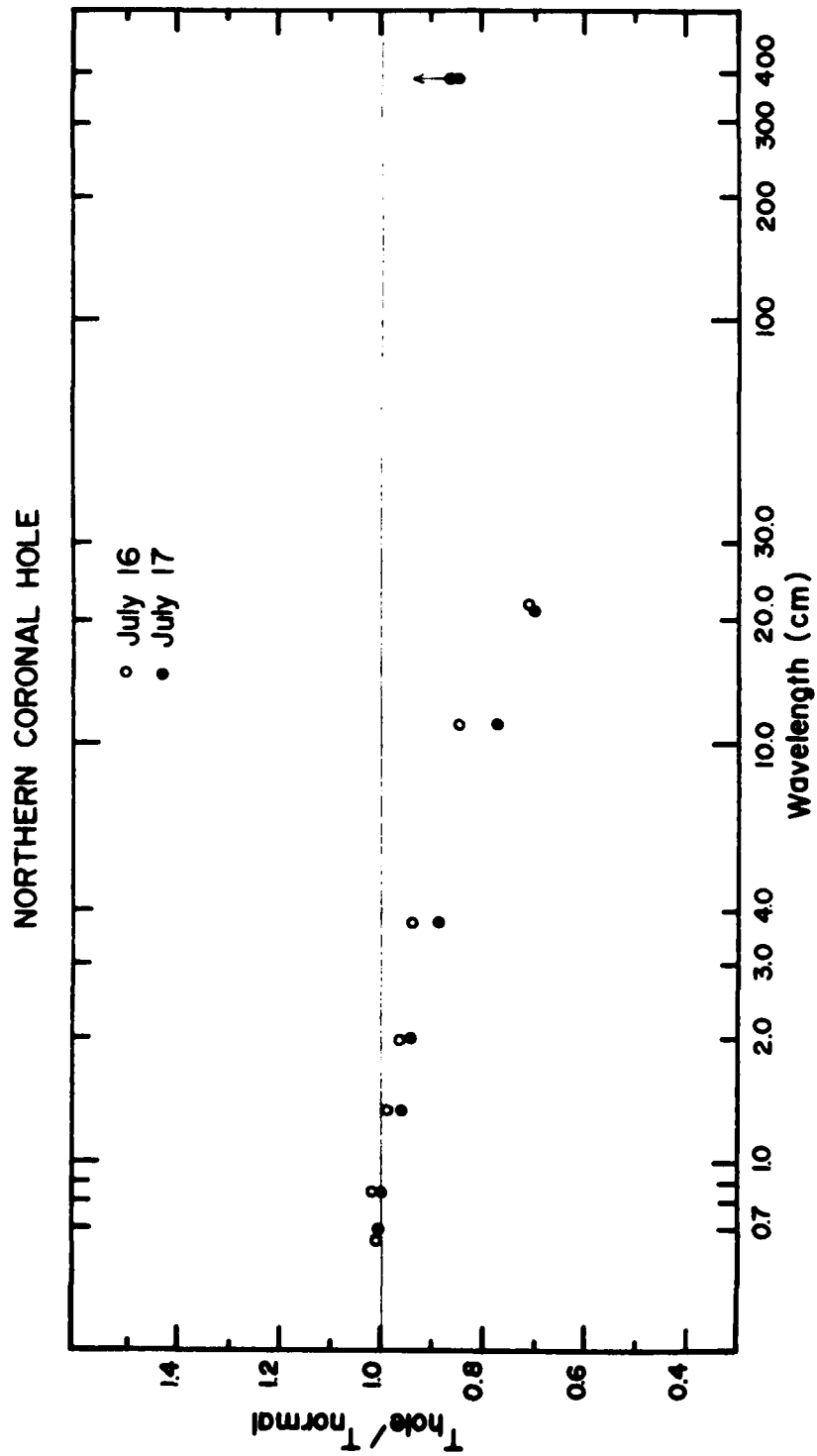


FIGURE 45

The Spectra of the Southern Coronal Hole - July 16

The southern coronal hole consists of two parts. The primary hole is an extension of the polar coronal hole, which reaches a latitude of approximately  $30^{\circ}$  S. The other part is a small coronal hole northeast of the main extension at about  $10^{\circ}$  S latitude.

TABLE 3

Spectra for the Southern Coronal Hole - July 16

Obs.	$\lambda(\text{cm})$	<u>Disk</u>			<u>Limb</u>		
		$T_q$	$T_h$	$T_h/T_q$	$T_q$	$T_h$	$T_h/T_q$
Culgoora	375	330	300	0.91	200	180	0.90
Arecibo	21.4	100	65	0.65	100	85	0.35
Arecibo	11.5	110	75	0.68	90	70	0.78
Haystack	3.81	100	92	0.92	96	90	0.94
Haystack	1.93	100	94	0.94	80	80	1.00
Haystack	1.38	100	97	0.97	70	70	1.00
La Posta	0.86	38.0	37.5	0.99	33	33	1.00
Haystack	0.69	95	95	1.00	70	70	1.00

This small region lies very near a filament, which makes interpreting the maps rather difficult. In order to avoid this difficulty, we will concentrate on the main coronal hole. Since this coronal hole covers a large range of latitudes, we can gain some additional information by determining the coronal hole spectrum not only at the position of greatest contrast, but also at a larger aiming parameter near the limb.

Table 8 presents the data for two different positions



in the coronal hole. The first is at the region of greatest contrast (about  $40^{\circ}$  S) and the second is near the photospheric limb. In general, near the limb the brightness contrast is much less. However, it is interesting that the Haystack map at 0.69 cm and the Itapetinga map at 0.70 cm suggest a slightly increased contrast between the coronal hole and the normal brightness near the limb. The Haystack map at 1.93 cm shows very little contrast near the limb, except for two small regions near the coronal hole. The one on the left shows a depression of about 2%, while the one on the right shows an enhancement of about 1-2%. This slightly enhanced region (which is almost directly on the central meridian) may not be within the area of the coronal hole and may, therefore be a region similar to the slight enhancements near the northern coronal hole. If, however, this region is within the coronal hole, the result would be consistent with the earlier results discussed in Chapter 3.

#### The Spectra of the Southern Coronal Hole - July 17

Table 9 gives the coronal hole spectra at the points of highest contrast and near the limb for July 17. The Culgoora 160 MHz map is sufficiently clear in the southern hemisphere (as opposed to the northern hemisphere - see above) to allow us to include it in the determination of the spectrum. As with the northern coronal hole, the results are similar enough to the results for July 16 to be considered consistent. Figure 46 shows the spectra for the southern coronal hole for both days and both positions.

TABLE 9

Spectra of the Southern Coronal Hole - July 17

Obs.	$\lambda$ (cm)	Disk			Limb		
		$T_q$	$T_h$	$T_h/T_q$	$T_q$	$T_h$	$T_h/T_q$
Culgoora	375	335	290	0.86	170	145	0.86
Culgoora	187	305	245	0.80	215	135	0.86
Arecibo	21.4	130	88	0.67	100	80	0.30
Arecibo	11.5	155	105	0.68	125	100	0.30
Haystack	3.81	100	87	0.87	94	90	0.96
Haystack	1.93	100	97	0.97	92	90	0.98
Haystack	1.33	100	97	0.97	90	90	1.00
La Posta	0.86	38.0	37.5	0.99	34	34	1.00
Itapetinga	0.70	99	98	0.99	85	85	1.00

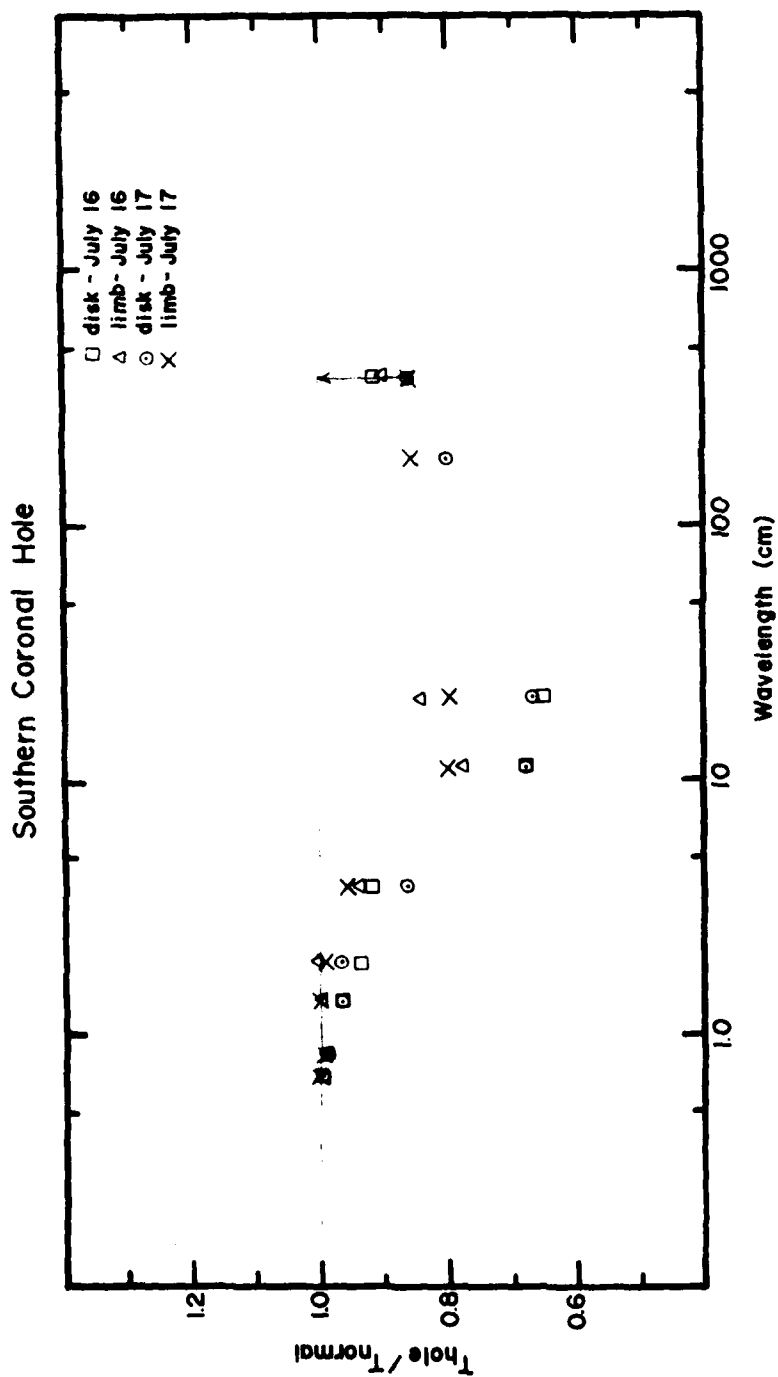


FIGURE 46

Chapter 5

SPECTRA AND CORONAL HOLE MODELS

5.1. The Spectra of Coronal Holes

Over the period covered by this contract we have been able to determine radio spectra for four different coronal holes. In one case, the southern coronal hole in July, 1973, we were even able to determine the spectrum at two different positions inside the hole, one near the polar limb and the other at the point of highest contrast at about  $40^{\circ}\text{S}$  latitude.

Although the individual spectra are discussed in the previous chapters, it is instructive to compare all of them here to see if there are any significant differences among the different coronal holes. Overall, the results are quite consistent, and the differences between coronal holes seem to be within the error bars of our observations and analysis. The greatest area of disagreement occurs around 2.0 cm. The spectrum for CH1 of 1973 and the spectrum for the coronal hole of September, 1977 both show a slight enhancement of approximately 2% around this wavelength. On the other hand, neither of the two coronal holes in the July, 1973 data show this enhancement, although in one case there was a region near and possibly inside the coronal hole that does show an enhancement. As was pointed out in the previous chapter, the Haystack data for July, 1978 do show a region of enhanced emission near the northern coronal hole but not inside the hole, while the southern coronal hole shows a slight enhancement near the limb which may or may

not be inside the coronal hole.

It is interesting to note that the data for CH1 indicate a depression of about 3% at 2.8 cm (Furst and Hirth, 1975) and a depression of about 2% at 3.8 cm. This rather odd dip in the spectrum is suspicious and may indicate that the errors in determining the relative brightness temperatures were greater than estimated. If so, the data are consistent with no detectable difference in brightness temperature around 2 cm between a coronal hole and the quiet solar background.

Finally, it must be pointed out that the spectrum near the limb for the July, 1978 southern coronal hole shows much less contrast when compared with the spectrum of the same coronal hole on the disk. This, however, is to be expected, since near the limb we do not reach as deep into the solar atmosphere, where the effects are more pronounced, as we do near the center of the solar disk.

## 5.2. Modeling - Procedures

Having determined the radio spectrum of a given coronal hole, we now want to use it to obtain the changes that occur in the electron density, temperature, and neutral particle density profiles inside the coronal hole. The brightness temperature at any given wavelength is a function of the temperatures, electron densities, and neutral particle densities along the ray path to the observer. At shorter wavelengths the emission originates deeper inside the solar

atmosphere, while at longer wavelengths it originates higher up. With observations available from 0.7 cm to 375 cm, i.e. over more than 9 octaves, we are able to gain information from as deep as the lower chromosphere, through the important transition zone and all the way to the outer corona.

The process of analyzing the data consists essentially of using a ray tracing procedure to compute the brightness temperature of the sun at a given wavelength and radial distance (aiming parameter) from the center of the solar disk. This is done first for the quiet sun and then for a sequence of modified solar atmospheres. The ratios of the computed brightness temperatures for the modified and the quiet solar atmosphere at a series of wavelengths are used to construct the radio spectrum for a particular modified model of the solar atmosphere. This is then compared with the actual radio spectrum of coronal holes deduced from our observations in an effort to determine the modified model that most closely matches the observed spectral characteristics of coronal holes.

This procedure requires a standard atmosphere for the quiet sun which can then be modified to find the changes inside the coronal holes. The model we have used for the quiet sun atmosphere is the Boston University Solar Model (Papagiannis and Kogut; 1975, 1976) which follows the Vernazza, et al. (1973) model for the chromosphere up to a height of 2400 km above the photosphere, and is then connected using the method described by Withbroe (1970) to a

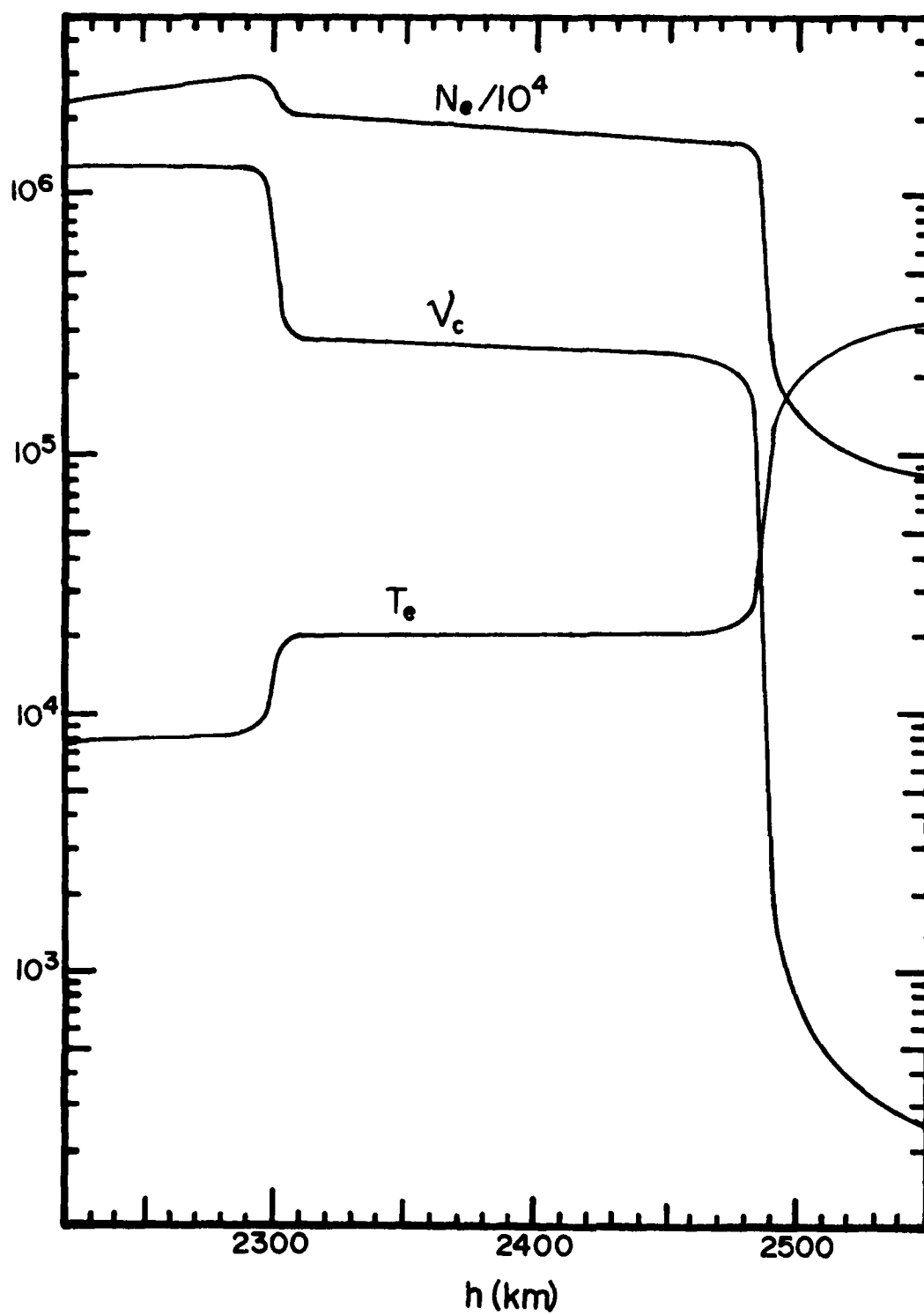


FIGURE 47

Dupree-Goldberg (1967) model for the transition zone and the corona. The electron density,  $N_e$ , the temperature,  $T$ , and the collision frequency,  $\nu_c$ , of the model near the critical transition zone are shown in Figure 47, while the complete listing of the different parameters of the model is given in Appendix I.

The brightness temperature,  $T_b$ , is given by the integral along the ray path

$$T_b = \int_{\text{path}} T e^{-\tau} d\tau \quad (1)$$

where  $T$  is the plasma temperature and  $\tau$  is the optical depth. Since this is actually calculated in discrete steps, the brightness temperature is approximated by the expression

$$T_b \approx \sum_m T_m e^{-\tau_m} \Delta\tau_m \quad (2)$$

where  $\tau_m$  is the optical depth to layer  $m$  and is given by the sum

$$\tau_m = \sum_{k=1}^{m-1} \Delta\tau_k \quad (3)$$

The equation for a ray trajectory is (Pawsey and Smerd; 1953)

$$\theta = a \int_r^{\infty} \frac{dr}{r \sqrt{\mu^2 r^2 - a^2}} \quad (4)$$



where  $r$  and  $\theta$  are sun centered polar co-ordinates,  $a$  is the aiming parameter (i.e. the radial distance of the observation point from the center of the solar disk), and  $\mu$  is the real part of the complex index of refraction. Both  $r$  and  $a$  are measured in terms of the photospheric radius,  $R_0$ . The optical depth is related to the absorption coefficient,  $\kappa$ , by the expression

$$\Delta\tau_m = \kappa_m \Delta s_m = \frac{\kappa_m \Delta r_m}{\cos \theta_m} \quad (5)$$

where  $\Delta s_m$  is the path length through layer  $m$ .

The absorption coefficient,  $\kappa_m$ , in layer  $m$ , is a function of the plasma frequency,  $f_{p,m}$  and the collision frequency,  $\nu_{c,m}$ , in this layer, and the radio frequency,  $f$ , of the observations. When the imaginary component of the refractive index is much less than 1 and the real component,  $\mu$ , is close to 1, the absorption coefficient can be approximated by the expression

$$\kappa_m \approx \frac{2}{c} \frac{f_{p,m}^2}{f^2} \nu_{c,m} \quad (6)$$

The collision frequency is the sum of the collision frequency of electrons with neutral particles,  $\nu_{n,m}$  and the collision frequency of electrons with ions,  $\nu_{i,m}$ :

$$\nu_{c,m} = \nu_{n,m} + \nu_{i,m} = C_n N_{n,m} T_m^{1/2} + C_i N_{e,m} T_m^{-3/2} \quad (7)$$

BOSTON UNIV MA DEPT OF ASTRONOMY  
RADIO STUDIES OF CORONAL HOLES. (U)  
MAR 81 M D PAPAGIANNIS, K B BAKER

F19628-77-C-0189

NL

40  
41  
42

END  
DATE  
FILMED  
9 8  
DTIC

where  $N_{n,m}$  is the density of neutral particles,  $N_{e,m}$  the electron density, which is assumed to be essentially equal to the ion density, and  $T$  is the plasma temperature. Nicolet (1973) gives for  $C_n$  the value  $C_n = 5.4 \times 10^{-10}$ , while Ginzburg (1961) gives an expression for  $C_i$  in the range of 30-50 with only a logarithmic dependence on  $N_e$  and  $T$ . In general the absorption coefficient also depends in a highly complex way on the magnetic field, but for the frequencies of interest here and the magnetic field strengths characteristic of coronal holes, the magnetic field effects are essentially negligible, and can therefore be neglected.

Once the temperature and particle density profiles are known, the ray tracing procedure (equation 4) can be used to follow the path of the ray and the brightness temperature of the emerging ray will be given by equation 2. In order to account for different changes of the quiet atmosphere model in different height ranges inside the coronal hole, we have divided the standard atmospheric model into five regions: the photosphere (0 - 600 km), the inner chromosphere (600-2300 km), the outer chromosphere (2300 - 2465 km), the transition zone (2465 - 2520 km), and the corona (2520 - 700,000 km). Since our radio data provide no information about the photosphere, this region played no role in our analysis and therefore was left unmodified. The upper four regions were given the numerical designations: lower chromosphere (0), upper chromosphere (1), transition zone (2), and corona (3).

In each of these upper four regions, the electron

density can be modified by multiplying the density of each layer in a region by a numerical factor  $\alpha_i$  ( $i=0,1,2,3$ ). Similarly, the temperature of each region can be modified by multiplying the temperatures by a factor  $\beta_i$ . For the modification of the neutral particle density we use a single factor,  $\gamma$ , for all the regions because their effects are important at only the lower regions which are reached only by the shorter wavelengths. A different form of modification is achieved by changing the thickness of each of the upper four regions. The thicknesses are changed by multiplying them with the factors  $\zeta_i$  ( $i=0-3$ ), which in effect change the gradients of all quantities in each region. If the modifications in two adjacent regions are different, the corresponding physical quantities are interpolated near the boundary so as to assure a smooth transition from one region to the next. When all the numerical factors mentioned above are equal to unity we simply have the standard solar model.

The entire procedure of modifying the standard atmospheric model, tracing ray paths and obtaining brightness temperatures at several wavelengths, normalizing the brightness temperatures to the corresponding values for the unmodified atmosphere, and finally plotting the entire radio spectrum for a particular modification of the standard model is accomplished by a single computer program. This program is listed in Appendix II along with a sample input and output.

Although it is possible to determine the effect of changing a single parameter, in general these parameters

interact with each other in non-linear ways, as is the case between electron density and temperature. A particular example is the relation between the electron density and the depth of the transition zone. The total number of electrons in the transition zone does not appear to change very significantly as it expands in a coronal hole. Thus when the transition zone expands by a factor of about 5 or 6, as was suggested by XUV data from Skylab (Bohlin, et al., 1975; Huber, et al., 1974; Withbroe, 1977), the electron number density decreases to about 20% of the normal value. The effect of the different modifications on the observed brightness depends also on the aiming parameter,  $\alpha$ , since at different values of the aiming parameter the rays follow different paths through the solar atmosphere. Near the limb, for example, at longer wavelengths we have the phenomenon of limb brightening, which tends to obscure the effects of coronal holes.

It must be mentioned that the entire modeling procedure we have followed assumes a spherically symmetric solar atmosphere and neglects changes toward the polar regions, which are actually present. We are mostly interested, however, in the modifications of a given profile of the solar atmosphere inside a coronal hole. The use of a somewhat different profile in the polar regions would simply produce somewhat different modifications more appropriate for this model, but overall the changes are likely to be in the same direction as in the case of the standard model.

### 5.3. Modeling - Results

To obtain a model for the solar atmosphere inside a coronal hole, we begin by determining the effects on the spectrum of changing each parameter of the standard model separately. These effects, of course, will be somewhat different for different values of the aiming parameter,  $\alpha$ . If changing a single parameter, such as  $N_e$  or  $T$ , doesn't produce the desired results we try combinations of the two parameters forming a grid of different numerical values for  $\alpha$  and  $\beta$ . The fitting of the coronal hole spectrum proceeds from the longer wavelength end because this corresponds to the outer most layers and is not affected by changes in the lower regions. We then proceed to the shorter wavelengths and the deeper layers of the atmosphere. Once a reasonably good fit is found for the entire spectrum, the parameters can be further modified by small amounts to improve the fit.

To demonstrate how this procedure works we will consider in detail the process as it applied to one particular coronal hole, the southern coronal hole of July 1973. Figure 44 shows the computed brightness temperature ratios and the observed ratios for the southern coronal hole of July 17, 1973. The preliminary estimates for the parameters are given in Table 10.

# PRELIMINARY MODEL FOR SOUTHERN CORONAL HOLE

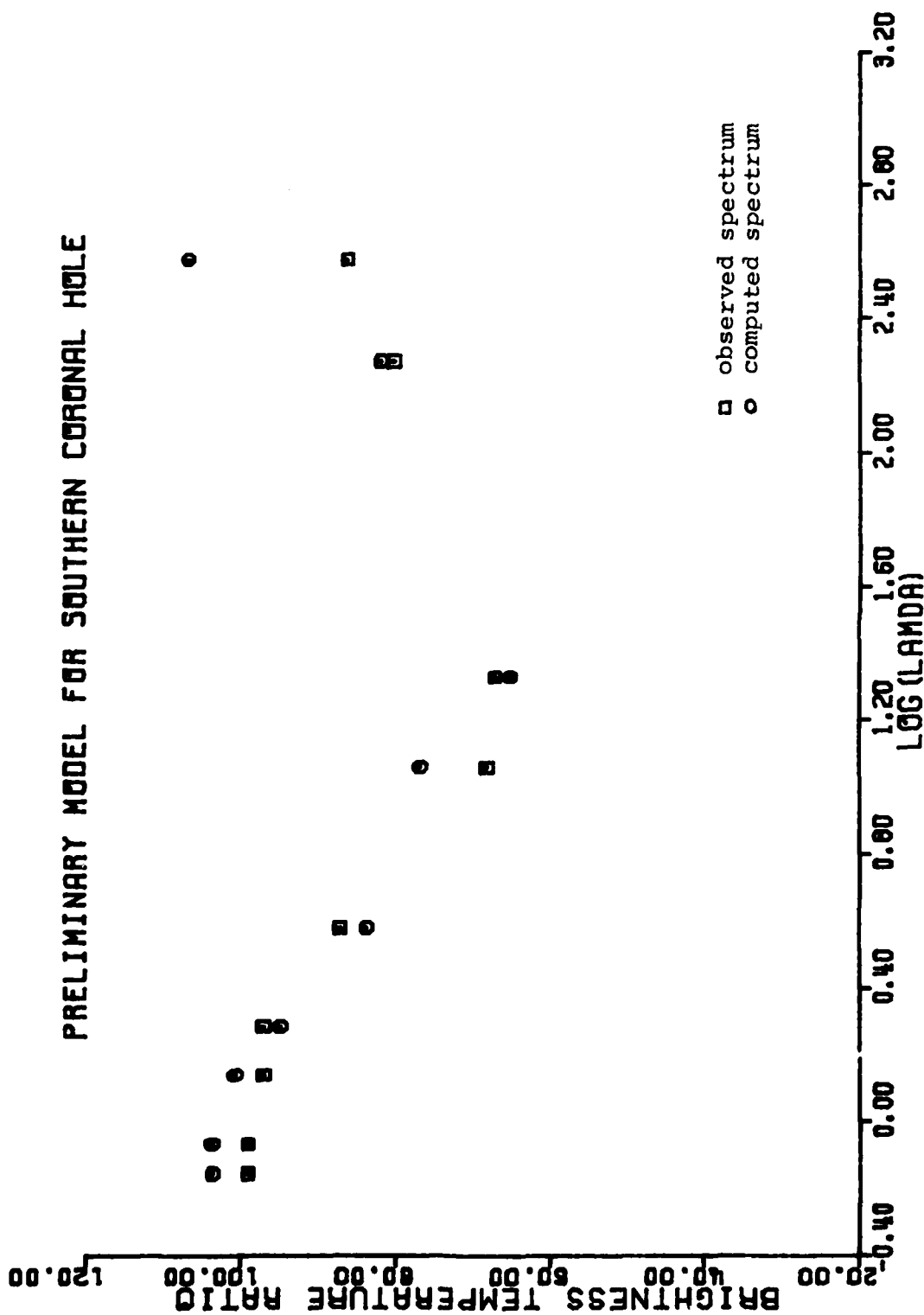


FIGURE 48

TABLE 10

Preliminary Parameter Estimates  
Southern Coronal Hole Disk Spectrum - July 17, 1978

	$\alpha$	$\beta$	$\gamma$	$\zeta$
0	0.8	0.9	0.8	2.5
1	0.8	0.3	0.8	2.0
2	0.15	0.45	0.8	6.0
3	0.3	0.3	0.8	1.0

In Figures 49 - 56 we show the procedure used to refine the original estimates. Each graph contains 4 curves plus the measured spectrum. In each case, two parameters in one region (e.g.  $\alpha_1$  and  $\beta_1$ ) have been modified around the initial estimates. From this set of graphs the effects of varying the different parameters around the initial estimates can be determined. The dominant effect of changing parameters in the chromosphere (regions 0 and 1) is observed at wavelengths shorter than about 5 cm. Varying the parameters in the transition zone (region 2) primarily affects the wavelength range from about 5 cm to 50 cm, while changing the corona (region 3) affects primarily the wavelengths longer than 50 cm but of course also has some affect on wavelengths in the 5 cm to 50 cm range.

One significant effect is that of changing the thickness of a region (parameter  $\zeta$ ). Increasing the thickness of a region while keeping the density and temperature unchanged results in an enhanced brightness temperature at wavelengths which emanate primarily from the modified region. However, if at the same time the density is decreased so as to maintain a constant number of particles in the region, the two effects tend to cancel out, and only a small change in brightness results.



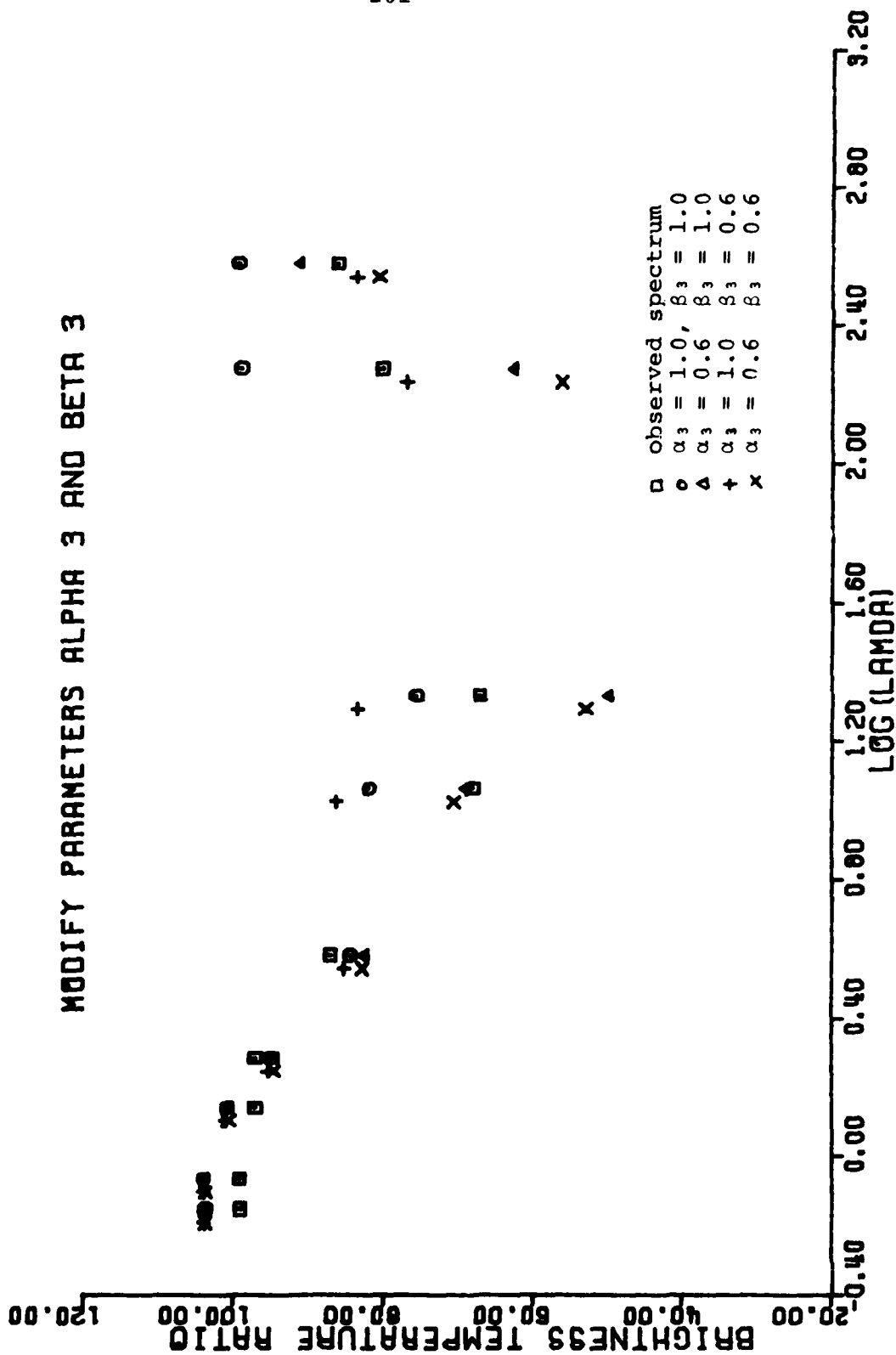


FIGURE 49

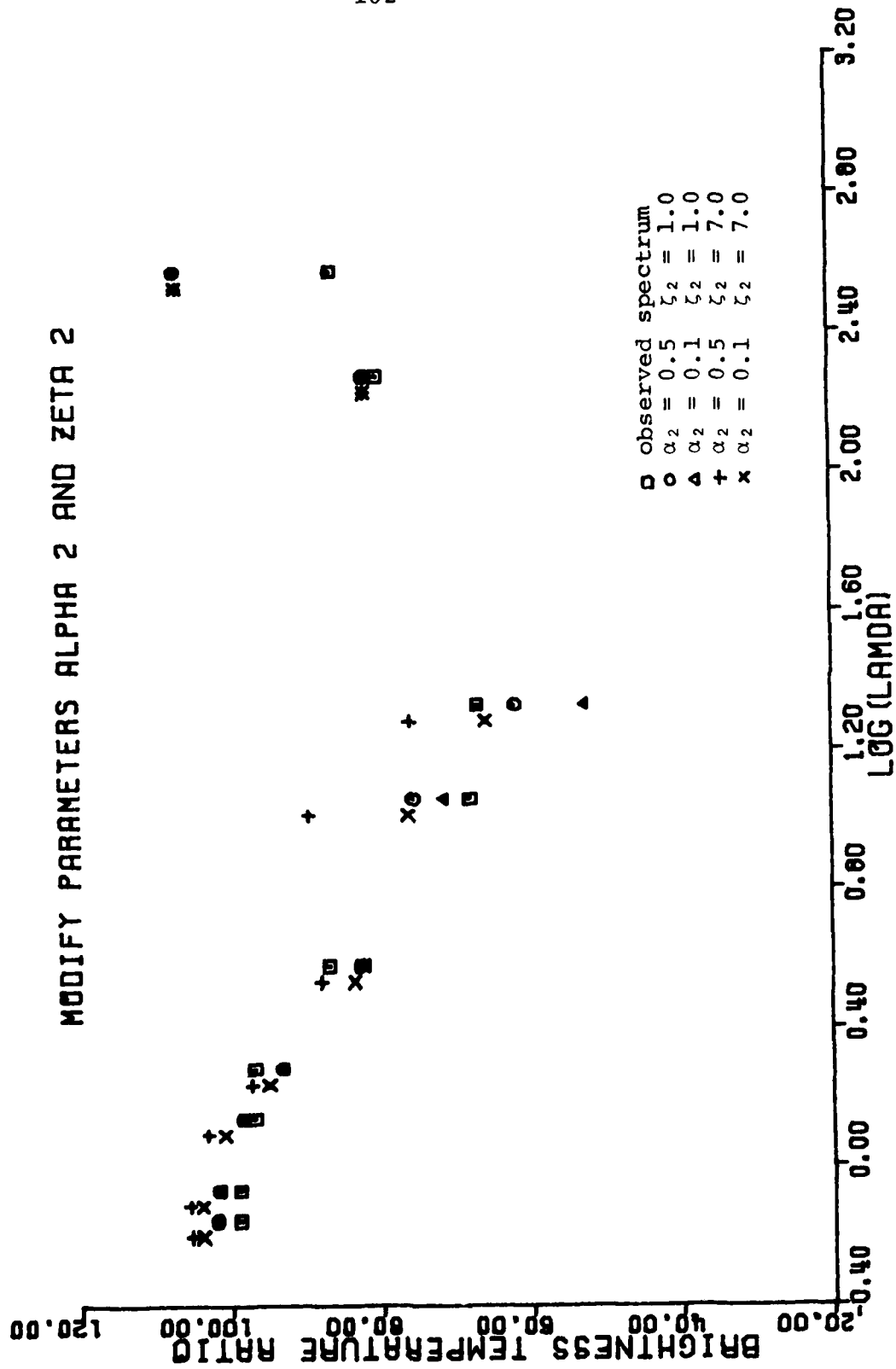


FIGURE 50

# MODIFY PARAMETERS ALPHA 2 AND BETA 2

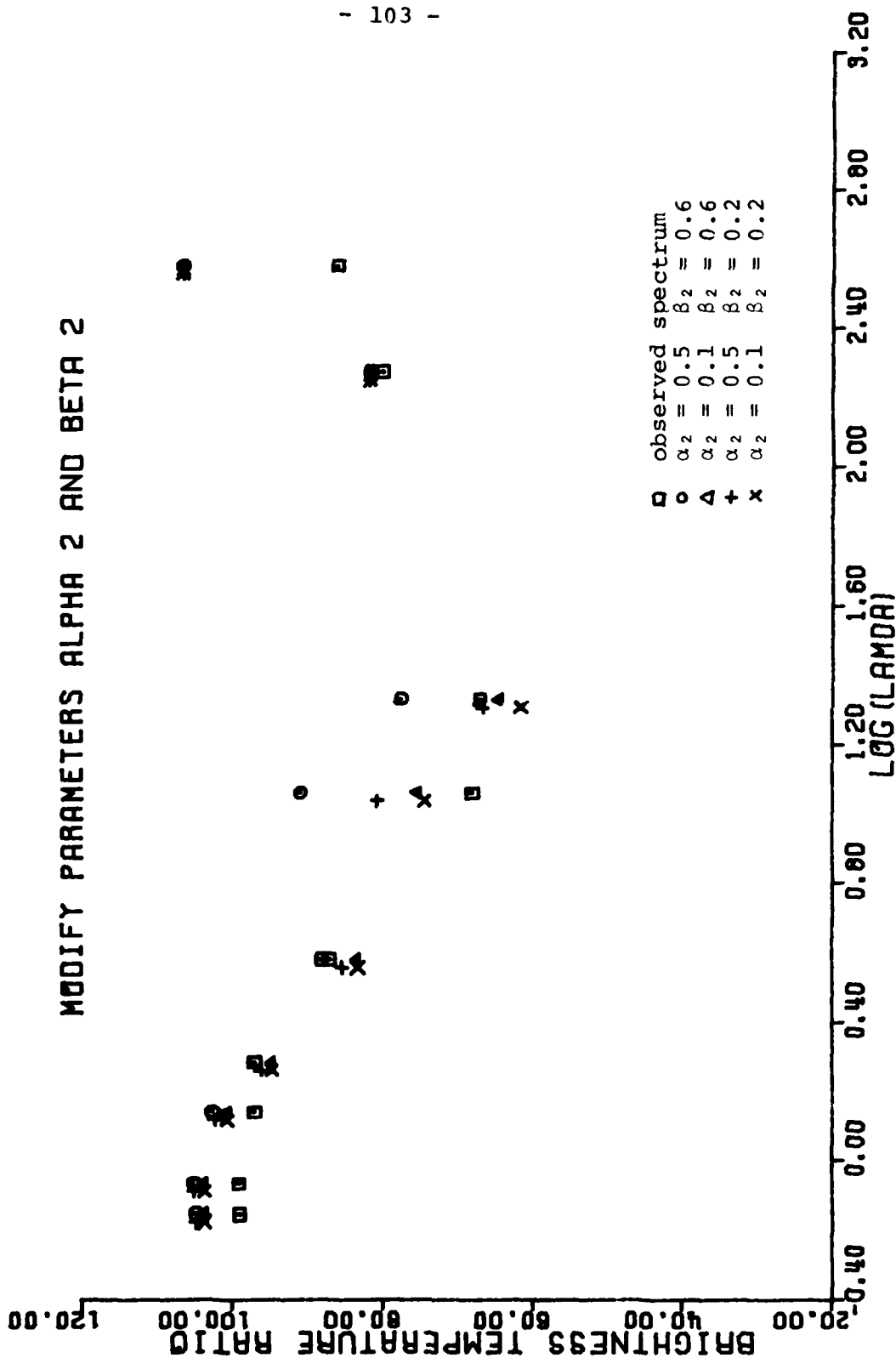


FIGURE 51

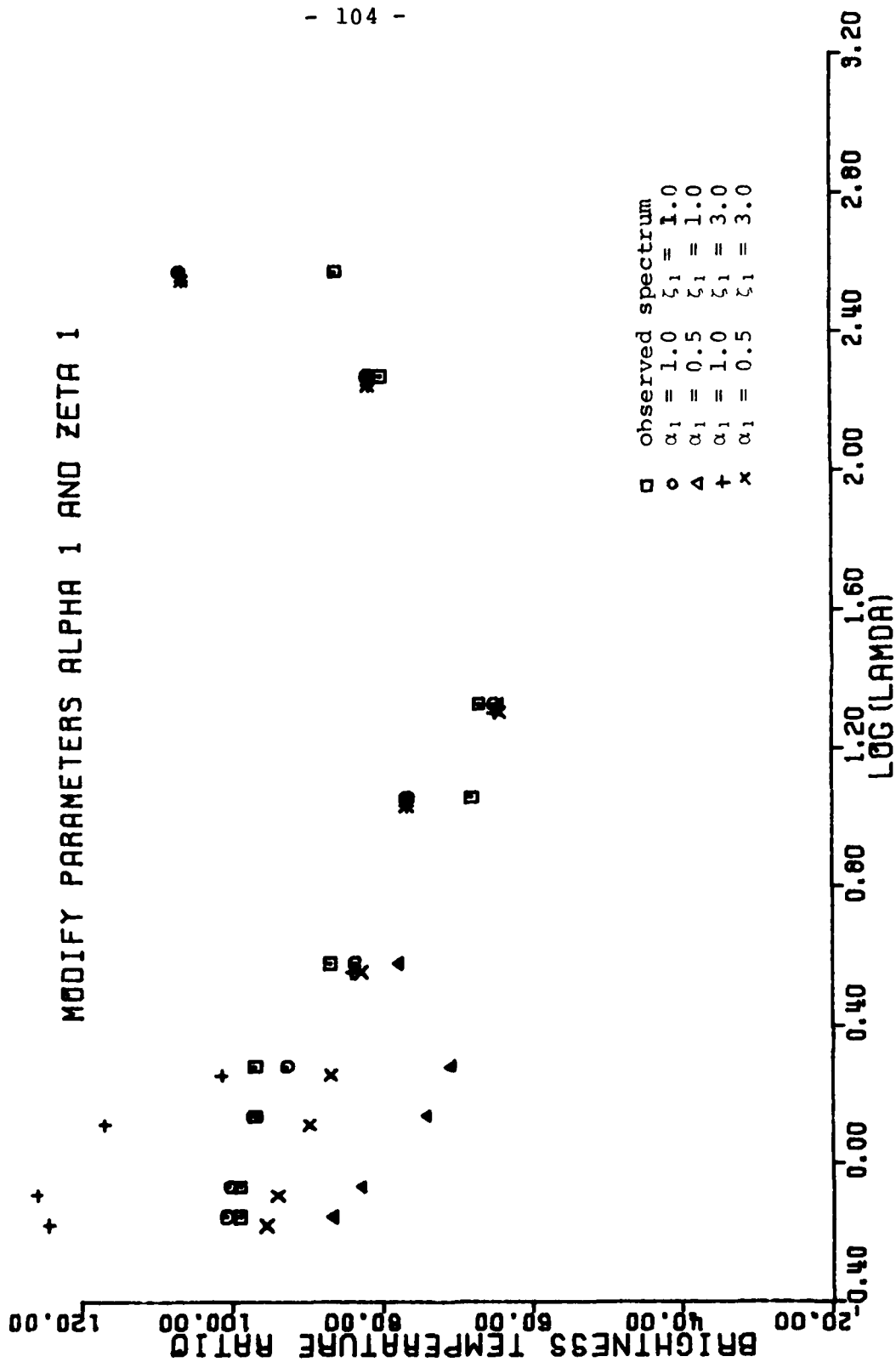


FIGURE 52

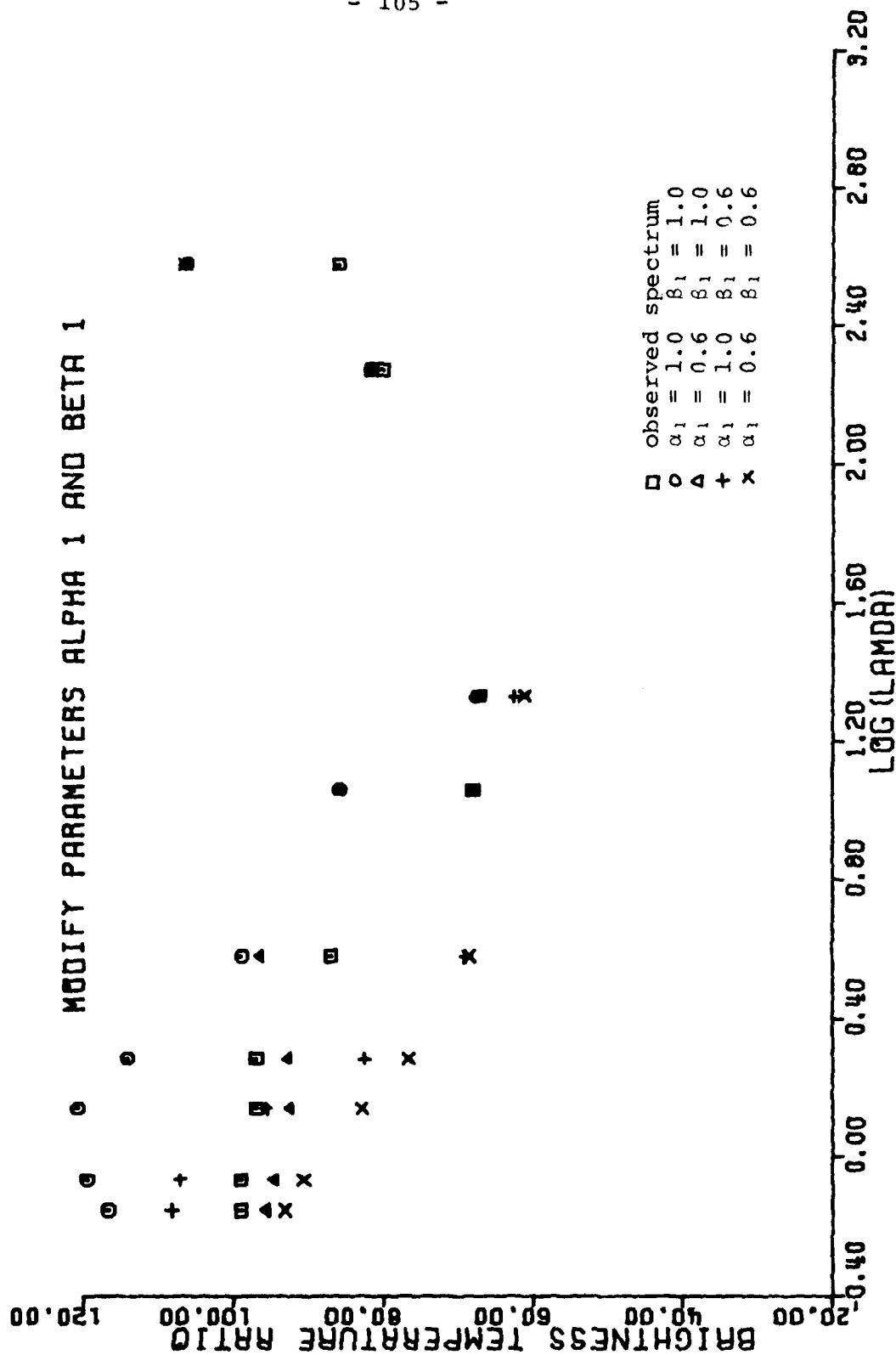


FIGURE 53

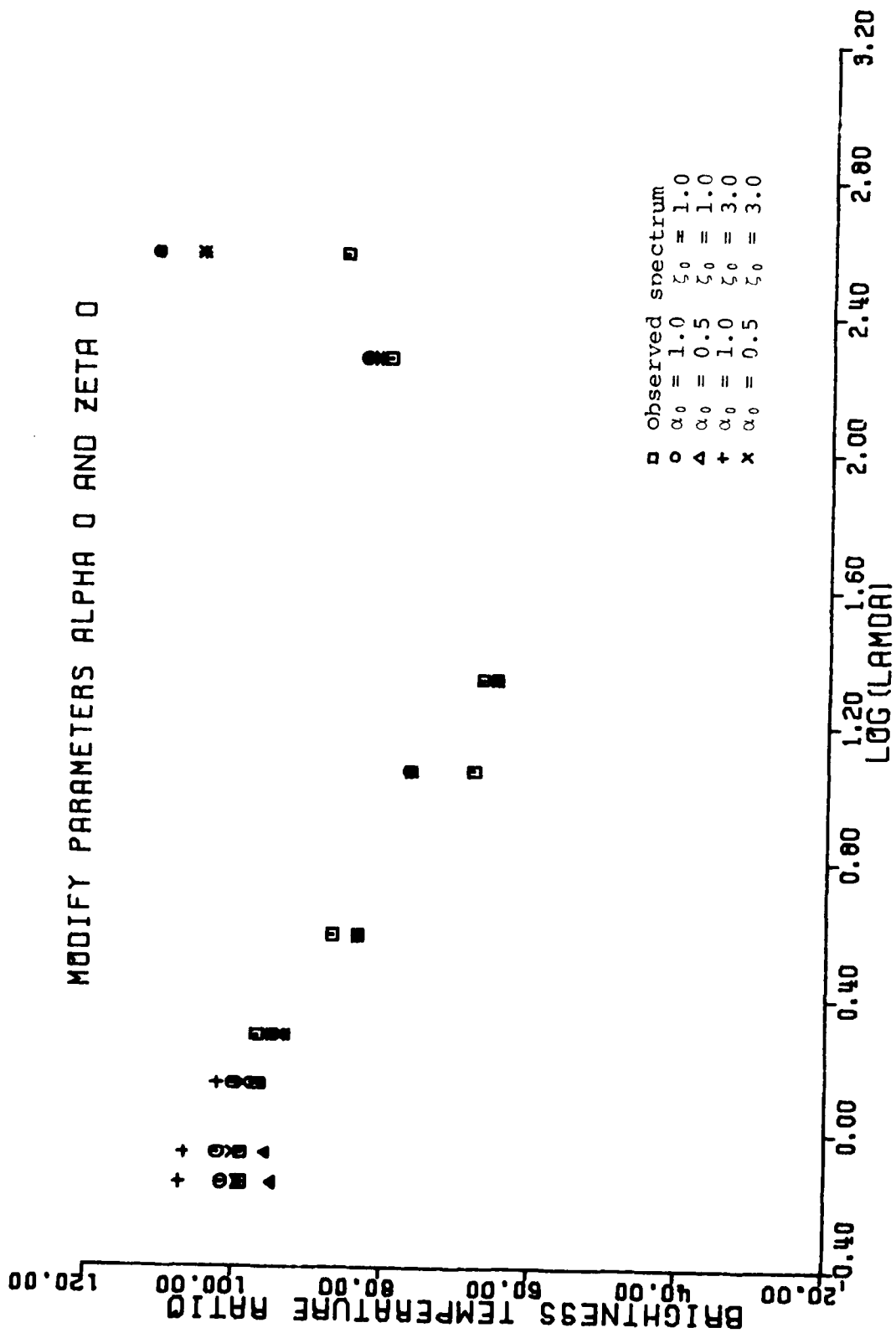


FIGURE 54

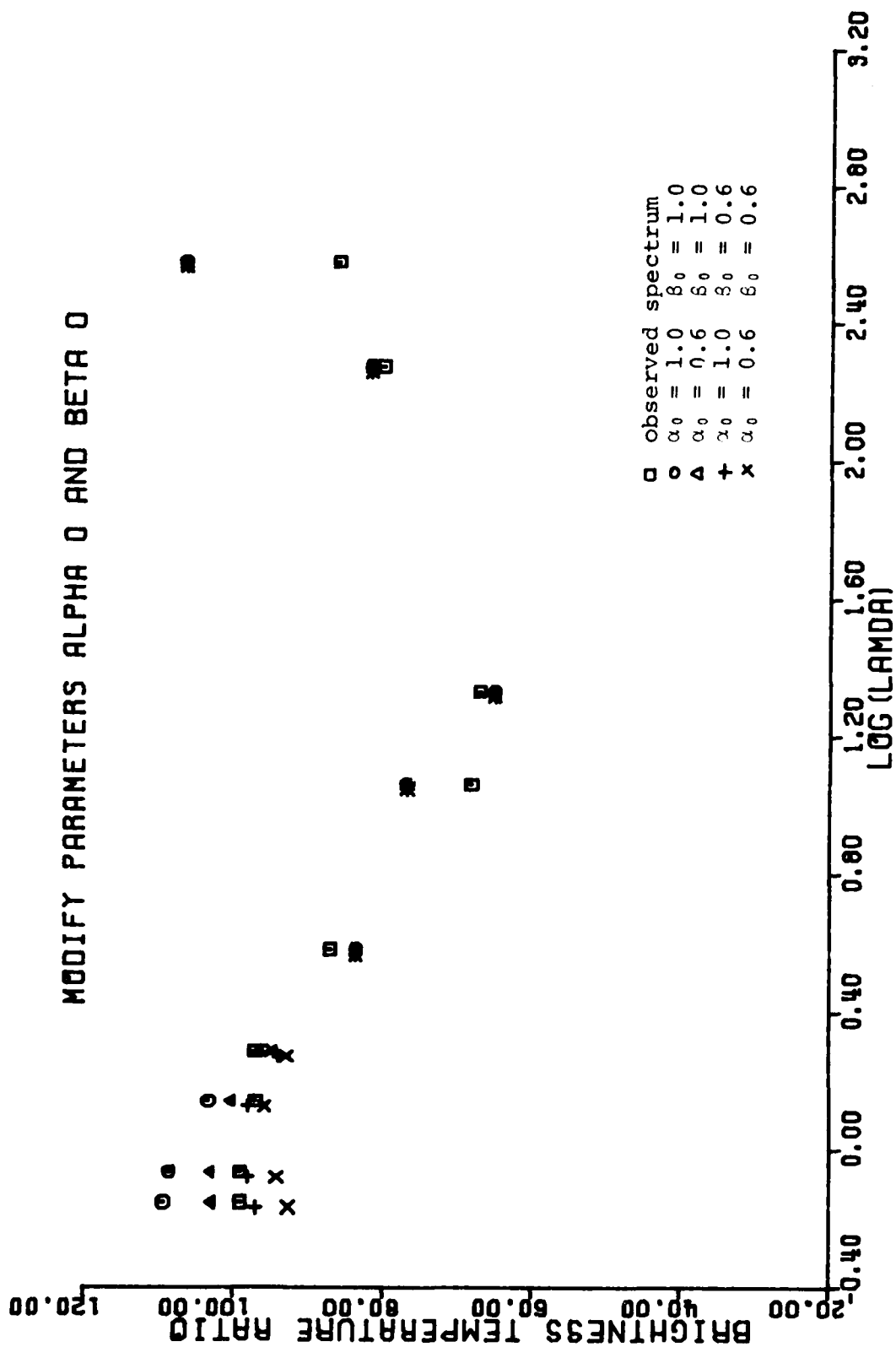


FIGURE 55

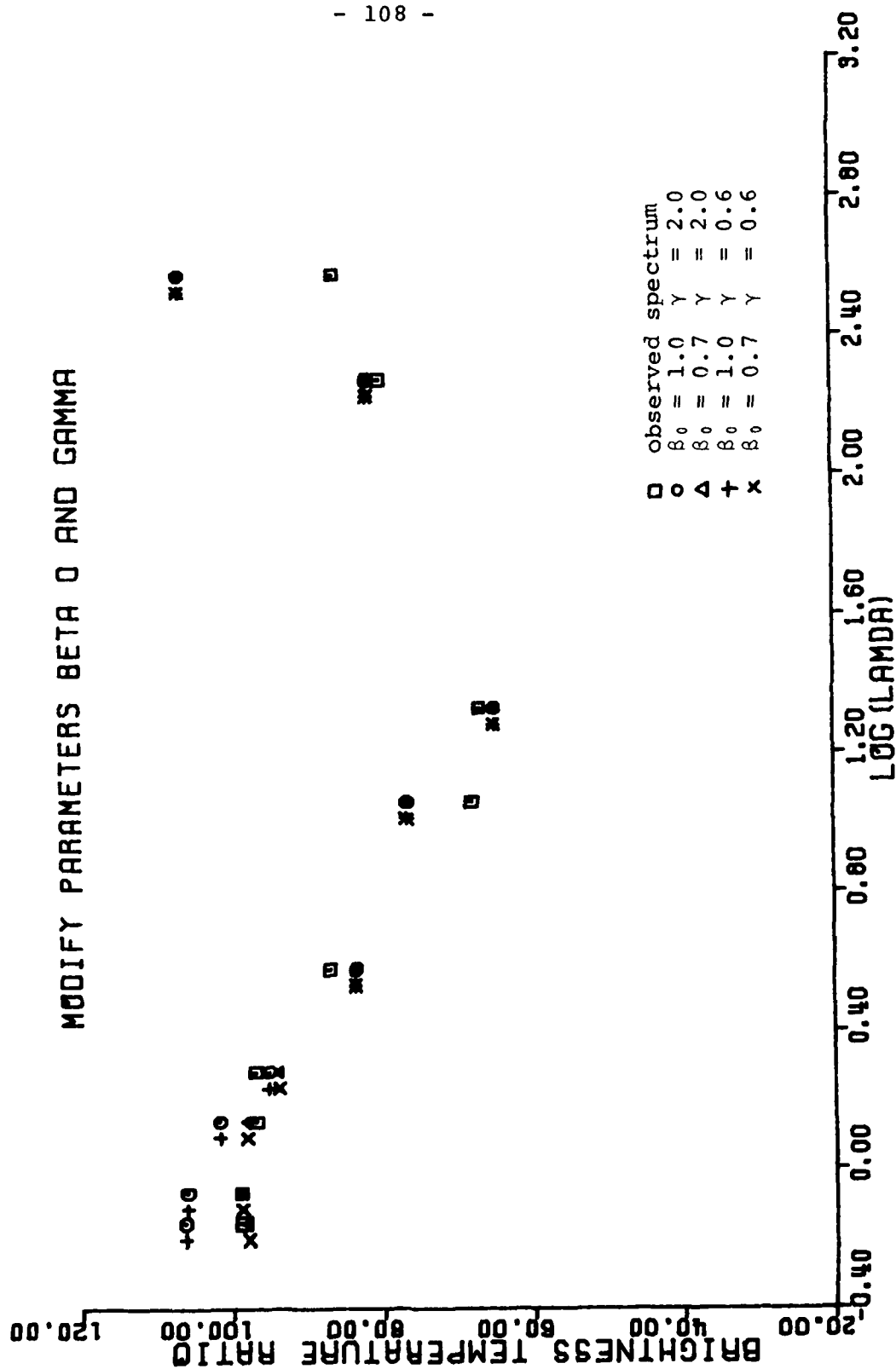


FIGURE 56



After observing the effects produced by changing different pairs of parameters, improved fits to the observed spectrum can be made by varying all the parameters over a limited range. The result of this final refinement of the parameters is shown in Figure 57 and the values of the parameters are given in Table 11.

TABLE 11  
Final Parameter Estimates  
Southern Coronal Hole Disk Spectrum - July 17, 1978

	$\alpha$	$\beta$	$\gamma$	$\zeta$
0	0.8	0.8	0.8	2.0
1	0.7	0.8	0.8	2.5
2	0.16	0.45	0.8	6.0
3	0.8	0.7	0.8	1.0

Our best results for the coronal hole modeling come from the July, 1978 observations. We have used these data to produce models of both the southern coronal hole and the northern coronal hole for both July 16 and July 17. In addition, we have produced separate models for the two different aiming parameters for the southern coronal hole. These results are summarized in Figures 57 - 62. In each figure the observed spectrum is shown as open boxes, while the theoretical spectrum is shown as open circles. As can be seen, the models fit the observations quite well. The values of the parameters for each model are listed in Table 12. We note that the parameters are quite consistent both for the two different days and for the two coronal holes.

TABLE 12

SOUTHERN CORONAL HOLE DISK SPECTRUM

	July 16				July 17			
	$\alpha$	$\beta$	$\gamma$	$\zeta$	$\alpha$	$\beta$	$\gamma$	$\zeta$
0	.73	.3	.3	1.5	.8	.8	.3	2.0
1	.77	.3	.3	2.3	.7	.3	.3	2.5
2	.16	.45	.8	6.0	.16	.45	.3	6.0
3	.75	.7	.8	1.0	.8	.7	.8	1.0

Southern Coronal Hole Limb Spectrum

	July 16				July 17			
	$\alpha$	$\beta$	$\gamma$	$\zeta$	$\alpha$	$\beta$	$\gamma$	$\zeta$
0	.35	.35	.35	1.0	.35	.35	.35	1.0
1	.30	.35	.35	2.1	.80	.35	.35	2.1
2	.16	.45	.85	6.0	.16	.45	.35	6.0
3	.36	.90	.85	1.0	.35	.33	.35	1.0

Northern Coronal Hole

	July 16				July 17			
	$\alpha$	$\beta$	$\gamma$	$\zeta$	$\alpha$	$\beta$	$\gamma$	$\zeta$
0	.3	.3	.3	2.0	.8	.8	.3	2.0
1	.7	.3	.3	2.5	.7	.8	.3	2.5
2	.16	.45	.3	6.0	.16	.45	.8	6.0
3	.5	.7	.8	1.0	.8	.7	.3	1.0

The layers of the solar atmosphere which contribute the largest fraction of the radio flux observed, vary from wavelength to wavelength. Figures 63 and 64 show the contribution to the flux as a function of height for different wavelengths. These figures are derived from the model of the southern coronal hole, but using a slightly different modification for a different coronal hole does not significantly alter the contribution profiles.

# SOUTHERN CORONAL HOLE DISK SPECTRUM - JULY 17

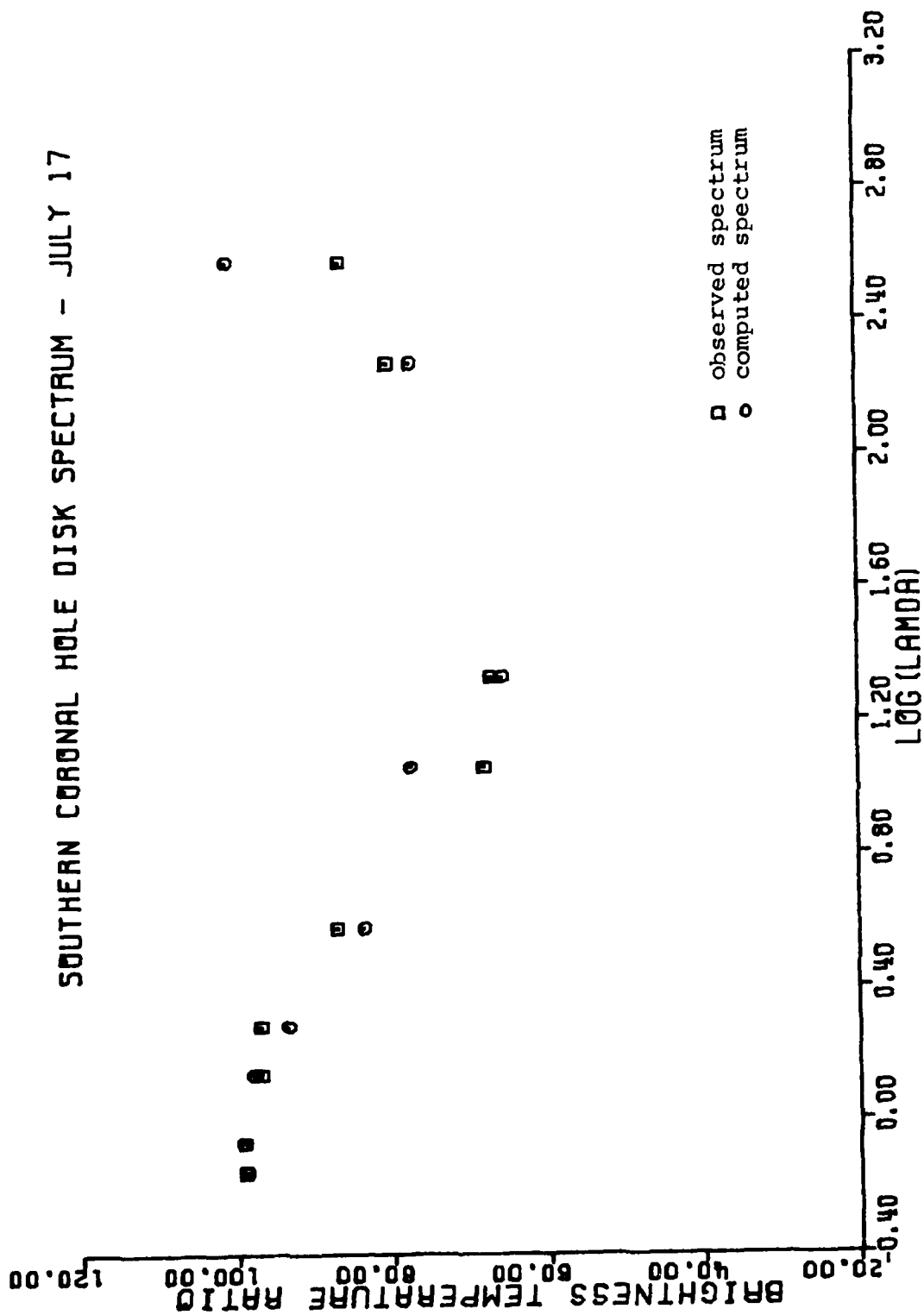


FIGURE 57

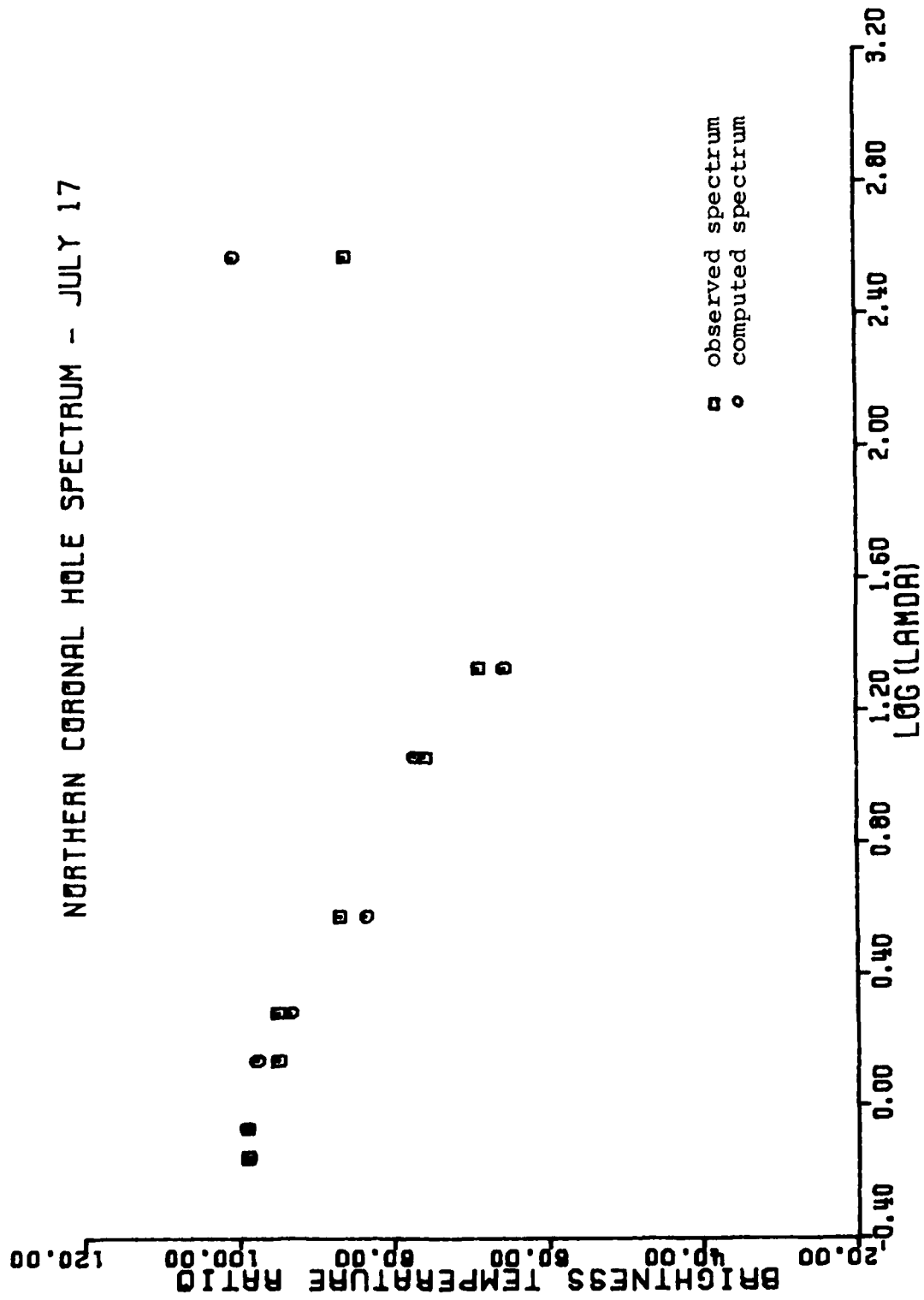


FIGURE 58

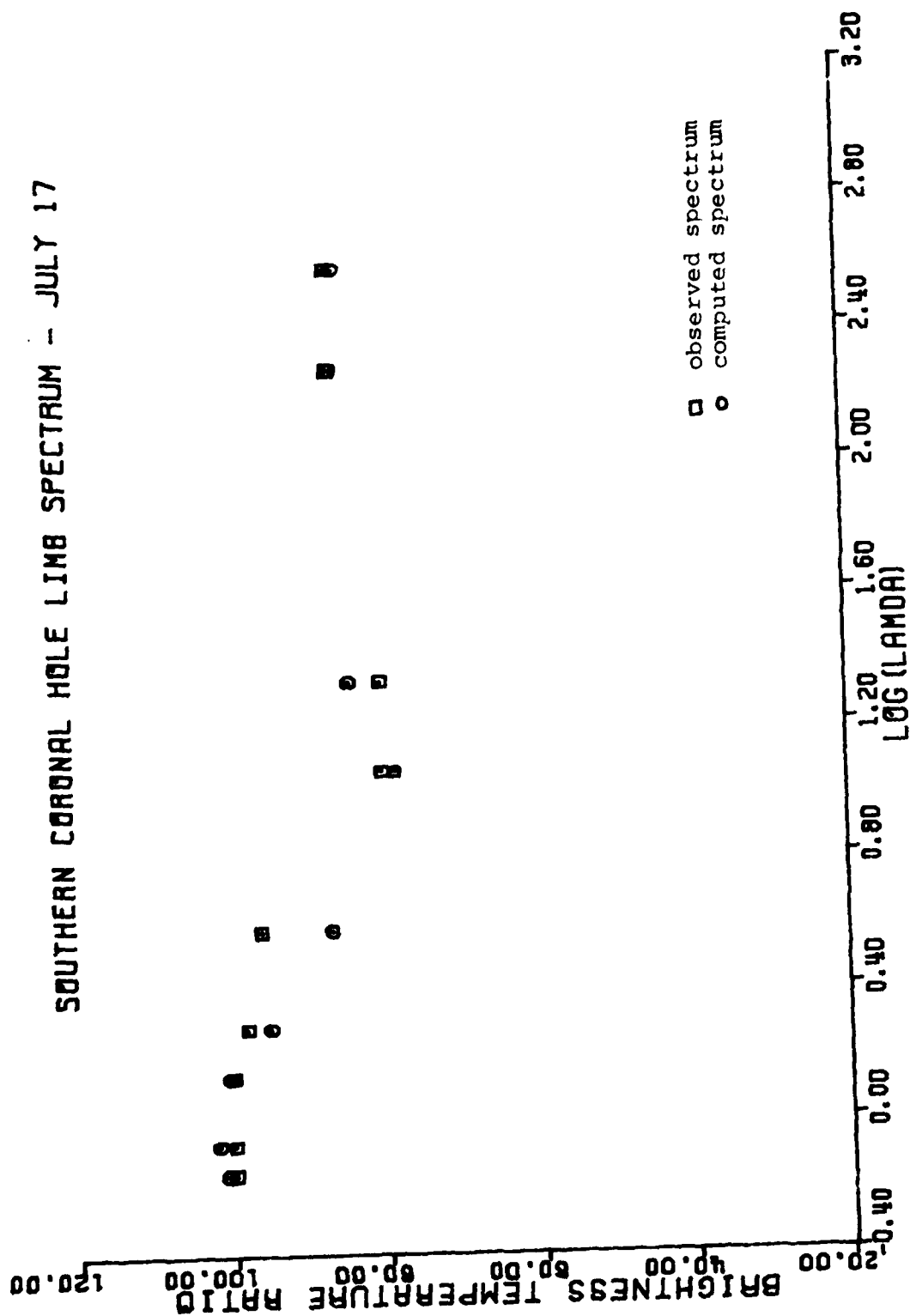


FIGURE 59

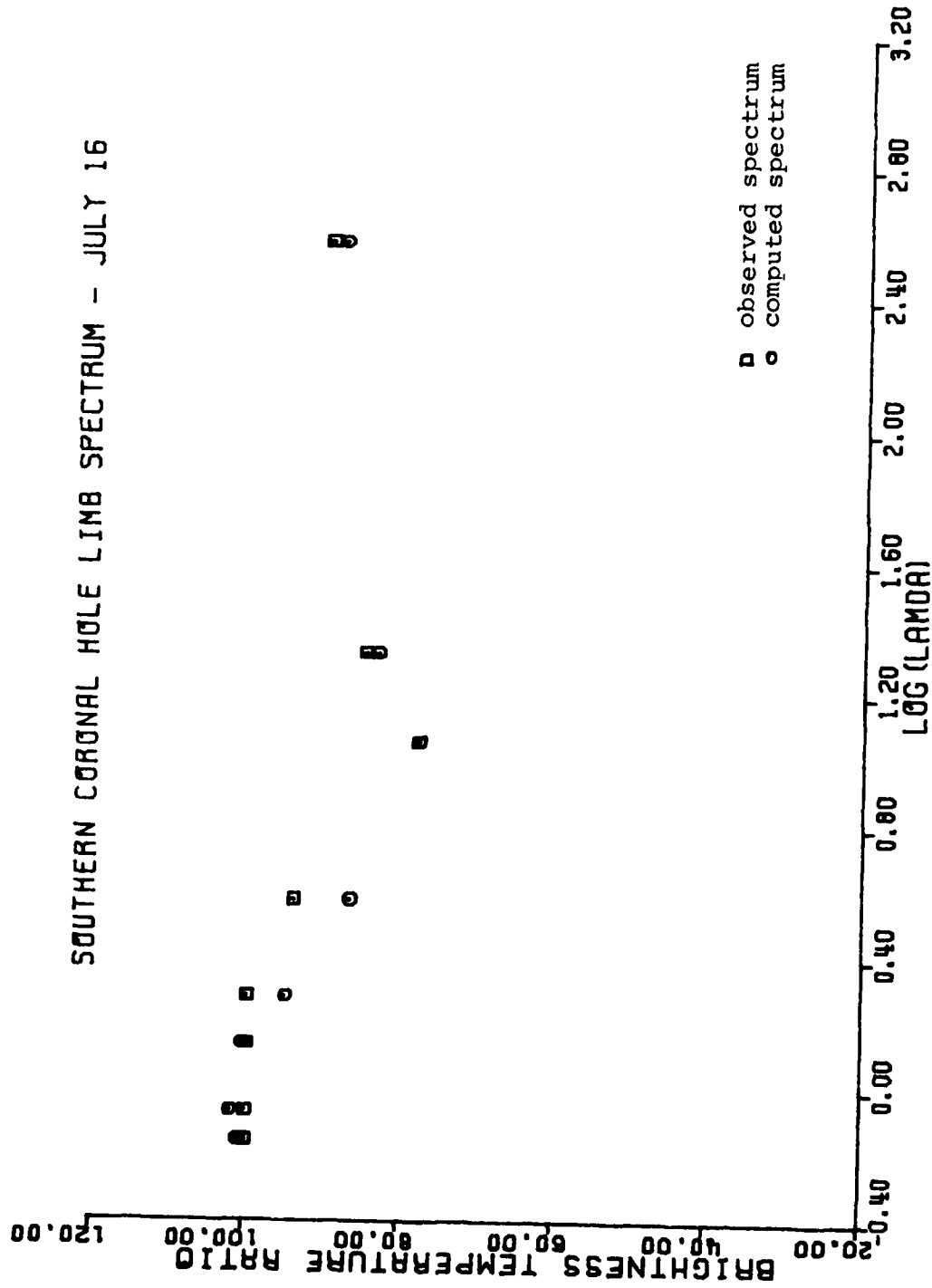


FIGURE 60

# SOUTHERN CORONAL HOLE DISK SPECTRUM - JULY 16

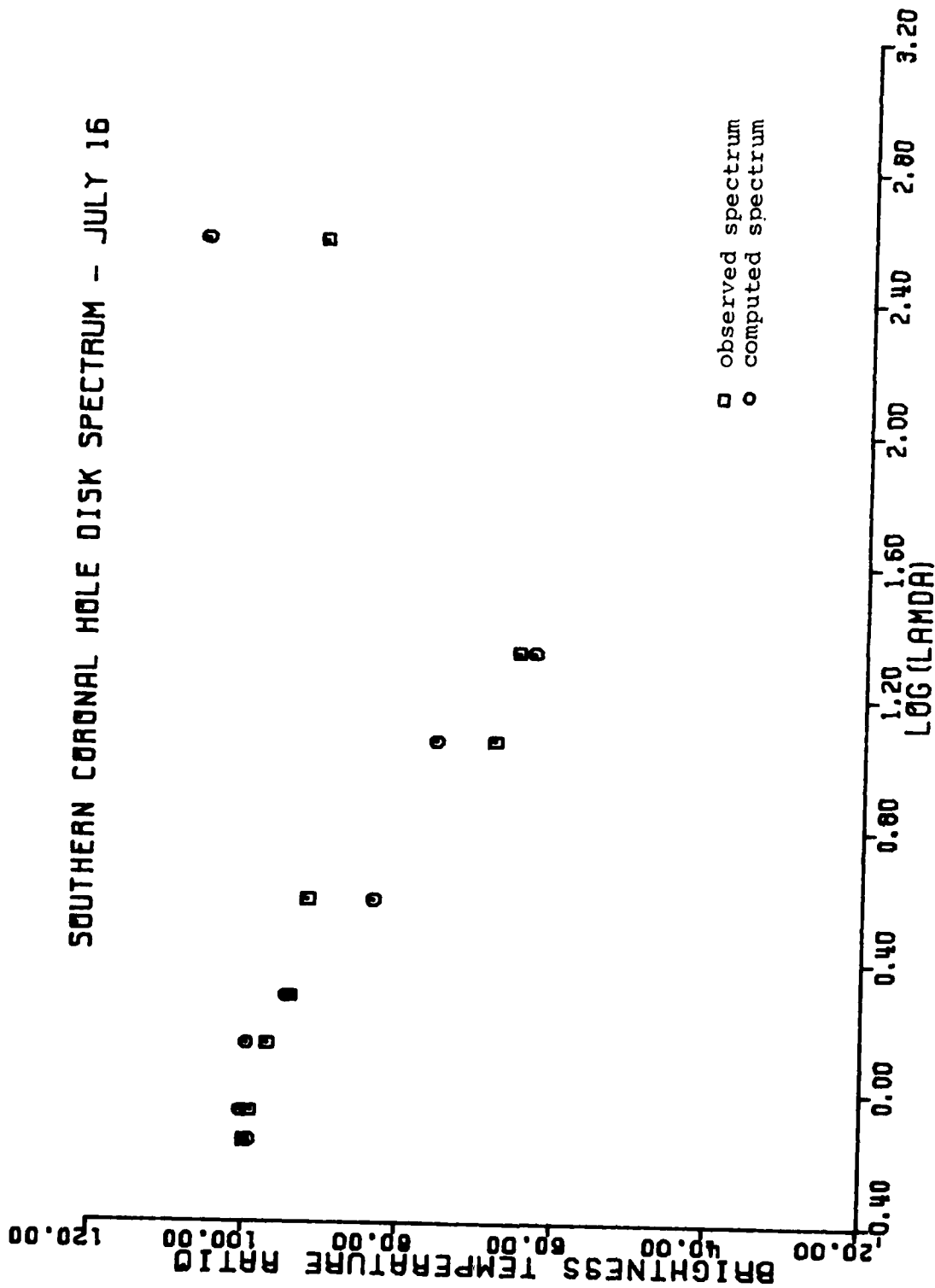


FIGURE 61

# NORTHERN CORONAL HOLE SPECTRUM - JULY 16

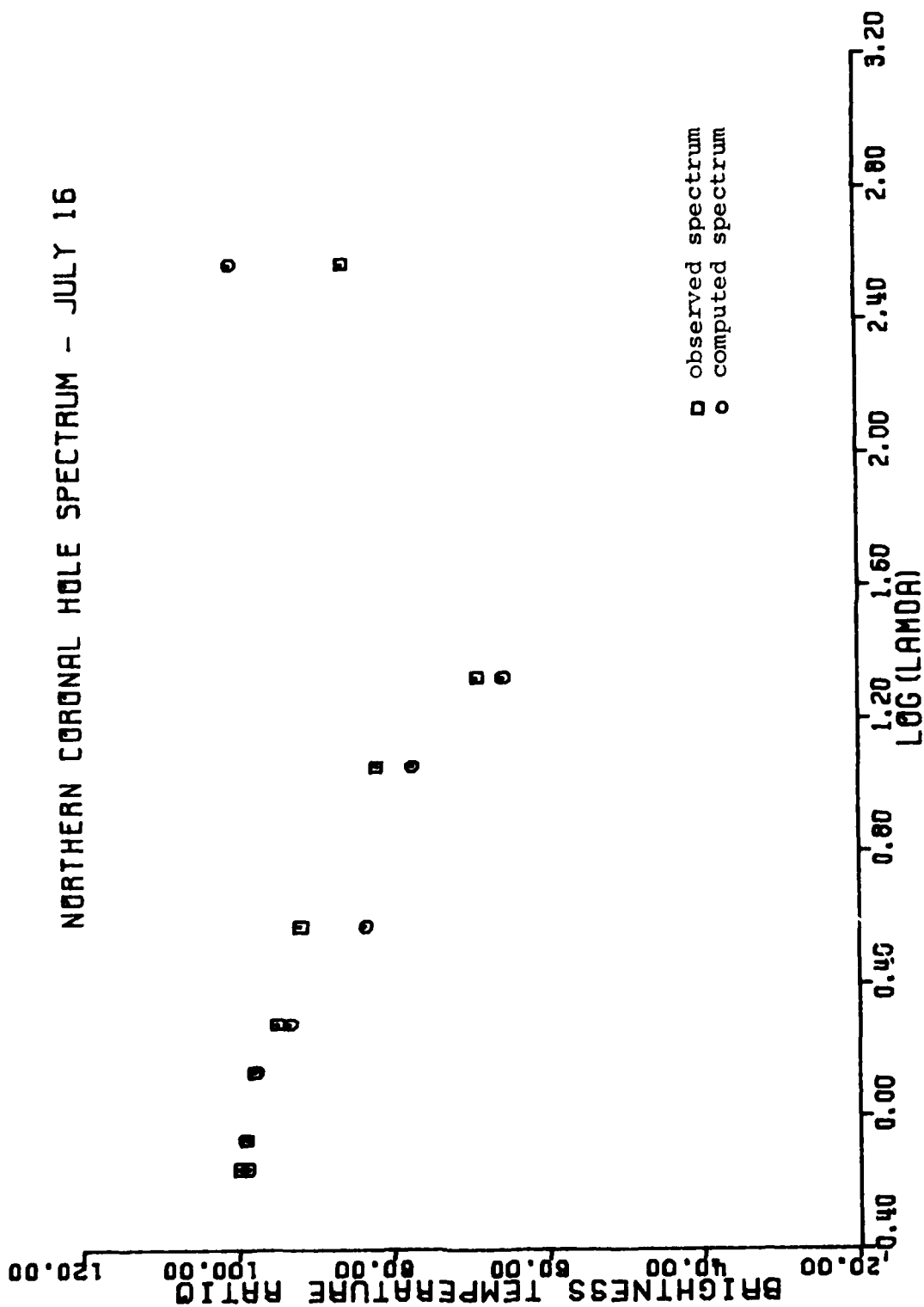


FIGURE 62



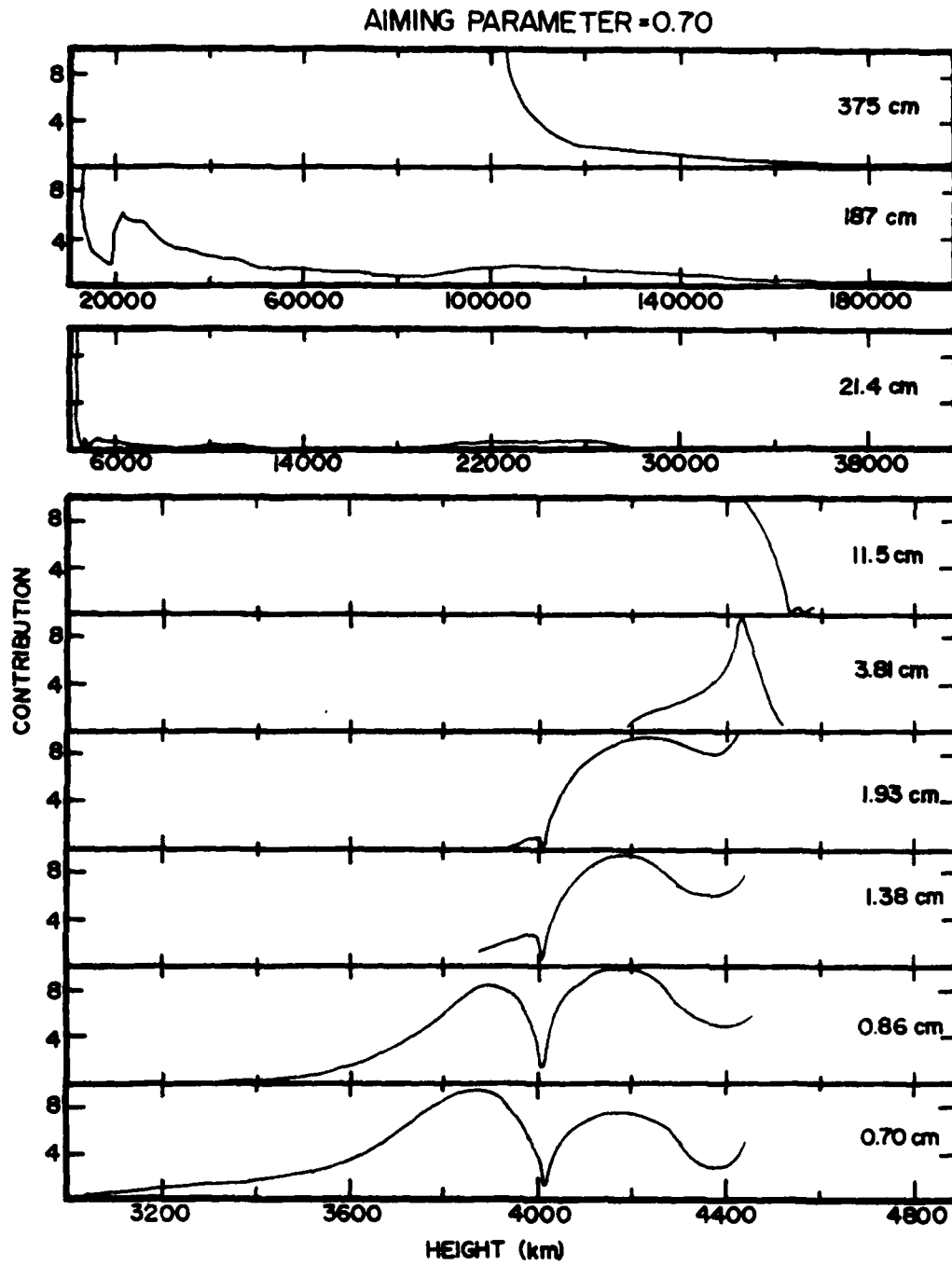


FIGURE 63

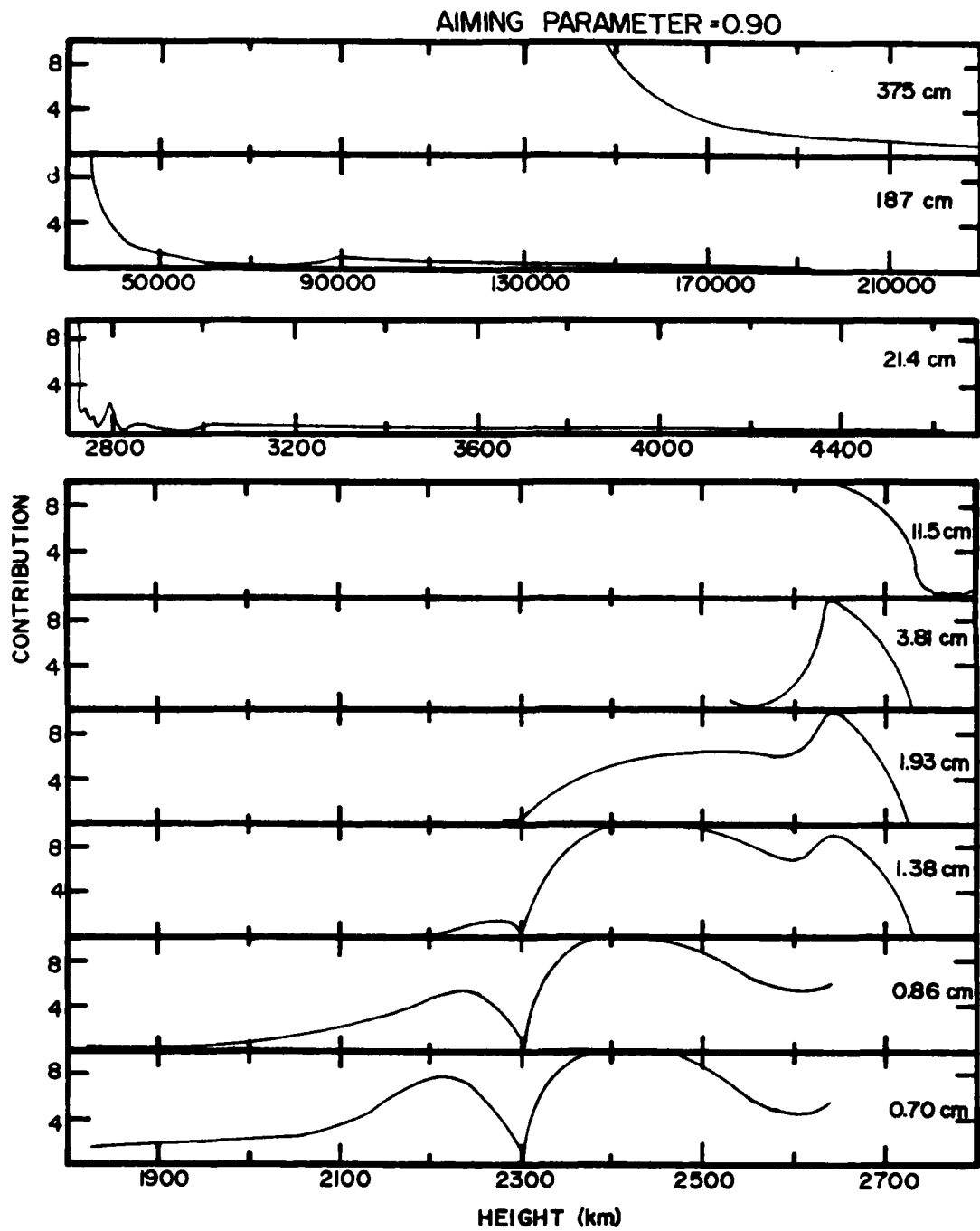


FIGURE 64

#### 5.4. Conclusions

The models we have computed for coronal holes are quite consistent from one hole to another and from one viewing angle (aiming parameter) to another. The general features are:

- 1) The chromosphere expands in thickness by about a factor of 2, but apparently fills in with material from the photosphere, since the values for  $N_n$  and  $N_e$  both decrease by only about 20%. The controversial enhancement near 2 cm can be obtained through a significant increase of the neutral particle density in this region.
- 2) The transition zone expands in thickness by about a factor of 5 to 6 and the electron density drops by a similar factor.
- 3) The corona itself does not appear to expand, but is depleted in particle density.
- 4) The temperatures are typically reduced by about 20%, except in the transition zone, where the reduction is around 50%. This indicates continued heating of these regions despite their expansion.

The coronal hole models obtained, together with other relevant information, such as solar wind speeds, etc., can now be used to develop a quantitative understanding of the physical processes operating inside coronal holes and to bring theory and observations into full agreement. This is a task that was beyond the goals of this project, but we hope to be able to undertake it in the near future.

ACKNOWLEDGEMENTS

We would like to thank Dr. Fred L. Wefer, now of Megatek Corporation, for his many important contributions in the progress achieved in this research contract, and Dr. Donald Guidice of AFGL for his valuable assistance and advice throughout this contract. We also want to thank the students of Boston University, Terry Varner, Michael Van Steenberg, Michele De La Pena and David Adler for their help in various aspects of the work performed under this contract.

We are grateful to Drs. Bracewell and Graf of Stanford University for providing us with the computer tapes of their 9.1 cm maps, to Drs. Coles and Rickett of UCSD and Drs. Watanabe and Kakinuma of the Toyokawa Observatory for their interplanetary scintillation data, to American Science and Engineering for the coronal hole x-ray data from Skylab and to Dr. Jack Harvey of the Kitt Peak National Observatory for his He 10830 A spectroheliograms and synoptic maps.

We want to express our appreciation to the staff and in particular to Dr. Michael Davis of the Arecibo Observatory and to the staff and in particular Mr. Bruce Lesley of the NEROC Haystack Observatory for their help and support during our 1977 and 1978 solar observations at these two major observatories.

Finally we want to thank the radio observatories of the University of British Columbia - Canada, La Posta - USA, Itapetinga - Brazil, Toyokawa - Japan, and Culgoora - Australia for participating in our 1978 international effort

- 121 -

to map the radio spectrum of coronal holes and for  
generously sharing their data with us.

REFERENCES

- Baker, K.B. and Papagiannis, M.D.: 1980, Air Force Geophysics Laboratory Report AFGL-TR-80-0123.
- Bohlin, J.D., Sheeley, N.R. Jr., and Tousey, R.: 1975, Space Res., XV, 651.
- Broussard, R.M., Sheeley, N.D., Jr., Tousey, R., and Underwood, J.H.: 1978, Solar Physics, 56, 161.
- Chiuderi-Drago, F.: 1974, Skylab Solar Workshop, ed. G. Righini, Oss. e Mem. Arcetri, No. 164.
- Chiuderi-Drago, F., Avignon, Y. and Thomas, R.S.: 1977, Solar Physics, 51, 143.
- Chiuderi-Drago, F. and Poletto, G.: 1977, Astronomy and Astrophysics, 50, 277.
- Chiuderi-Drago, F.: 1980, Solar Physics, 65, 237.
- Coles, W.A. and Rickett, B.J.: 1976, J. Geophys. Res., 81, 4797.
- Coles, W.A., Rickett, B.J., Rumsey, K.H., Kaufmann, J.J., Furley, D.G., Ananthakrishnan, S., Armstrong, J.W., Harmons, J.K., Scott, S.L., and Sime, D.G.: 1980, Nature, 286, 239.
- Covington, A.E.: 1976, AAS Bulletin, 8, 339.
- Dulk, G.A. and Sheridan, K.V.: 1974, Solar Physics, 36, 191.
- Dulk, G.A., Sheridan, K.V., Smerd, S.F. and Withbroe, G.L.: 1977, Solar Physics, 52, 349.
- Dupree, A.K. and Goldberg, L.: 1967, Solar Physics, 1, 229.
- Furst, E. and Hirth, W.: 1975, Solar Physics, 42, 157.
- Ginzburg, V.L.: 1961, Propagation of Electromagnetic Waves in Plasma, Gordon and Breach, New York.
- Graf, W. and Bracewell, R.N.: 1975, Report UAG-44, World Data Center A for Solar-Terrestrial Physics, Boulder, Colorado.
- Huber, M.C., Foukal, P.V., Noyes, R.W., Reeves, E.M., Schmahl, E.J., Timothy, J.G., Vernazza, J.E., and Withbroe, G.L.: 1974, Astrophys. J. Lett., 194, L115.

- Hundhausen, A.J.: 1977, Coronal Holes and High Speed Wind Streams, ed. J.B. Zirker, p. 225-330, Colorado Assoc. Univ. Press., Boulder, Colorado.
- Kopp, R.A. and Orral, F.Q.: 1977, Coronal Holes and High Speed Wind Streams, ed. J.B. Zirker, p. 179-224, Colorado Assoc. Univ. Press, Boulder, Colorado.
- Krieger, A.S., Timothy, A.F. and Roelof, E.C.: 1973, Solar Physics, 29, 505.
- Kundu, M.R. and Liu, X.Y.: 1976, Solar Physics, 49, 267.
- Lantos, P. and Avignon, Y.: 1975, Astron. and Astrophys., 41, 137.
- Mariska, J.T.: 1978, Astrophys. J., 225, 352.
- Mariska, J.T. and Withbroe, G.L.: 1978, Solar Physics, 60, 67.
- Newpert, W.M. and Pizzo, V.: 1974, J. Geophys. Res., 79, 3701.
- Nicolet, M.: 1953, J. Atm. Terr. Phys., 53, 451.
- Nolte, J.T., Krieger, A.S., Timothy, A.F., Gold, R.E., Roelof E.C., Vaiana, B., Lazarus, A.J., Sullivan, J. D., and McIntosh, P.S.: 1976a, Solar Physics, 46, 303.
- Nolte, J.T., Krieger, A.S., Timothy, A.F., Vaiana, G.S. and Zombeck, M.V.: 1976b, Solar Physics, 46, 291.
- Nolte, J.T., Davis, J.M. and Sullivan, J.D.: 1978, Solar Physics, 60, 207.
- Papagiannis, M.D. and Kogut, J.A.: 1975, Air Force Geophysics Laboratory Report, AFCRL-TR-75-0430.
- Papagiannis, M.D. and Kogut, J.A.: 1976, Solar Physics, 48, 49.
- Papagiannis, M.D. and Wefer, F.L.: 1977, AAS Bulletin, 9, 617.
- Papagiannis, M.D. and Wefer, F.L.: 1978a, EOS, 59, 367.
- Papagiannis, M.D. and Wefer, F.L.: 1978b, Nature, 273, 5663.
- Papagiannis, M.D. and Baker, K.B.: 1980, EOS, 61, 1095.
- Rickett, B.J., Sime, D.G., Sheeley, N.R. Jr., Crockett, W.R., and Tousey, R.: 1976, J. Geophys. Res., 81, 3845.

- Sime, D.G. and Rickett, B.J.: 1978, J. Geophys. Res., 83, 5757.
- Straka, R.M., Papagiannis, M.D. and Kogut, J.A.: 1975, Solar Physics, 45, 131.
- Vernazza, J.E., Avrett, E.H. and Loeser, R.: 1973, Astrophys. J., 184, 605.
- Wefer, F.L., Bleiweiss, M.P., and Hurst, M.D.: 1976, Megatek Corporation Report R2005-031-F01.
- Wefer, F.L. and Bleiweiss, M.P.: 1976, AAS Bulletin, 8, 338.
- Wefer, F.L. and Papagiannis, M.D.: 1977a, Air Force Geophysics Laboratory Report, AFGL-TR-77-0292.
- Wefer, F.L. and Papagiannis, M.D.: 1977b, AAS Bulletin, 9, 617.
- Wefer, F.L., Papagiannis, M.D., Van Steenberg, M.E. and Varner, T.M.: 1978, AAS Bulletin, 10, 684.
- Wefer, F.L., Papagiannis, M.D., Van Steenberg, M.E. and Varner, T.M.: 1979, Air Force Geophysics Laboratory Report, AFGL-TR-78-0284.
- Wefer, F.L. and Papagiannis, M.D.: 1980, Solar Physics, 67, 13.
- Withbroe, G.L.: 1970, Solar Physics, 11, 208.
- Withbroe, G.L. and Wang, Y.M.: Solar Physics, 27, 1972.
- Withbroe, G.L.: 1977, Coronal Holes and High Speed Wind Streams, ed. J.B. Zirker, p. 145-177, Colorado Assoc. Univ. Press, Boulder, Colorado.
- Withbroe, G.L.: 1978, Air Force Geophysics Laboratory Report, AFGL-TR-78-0217.



APPENDIX I  
STANDARD SOLAR ATMOSPHERE MODEL

HT(km)	T(°K)	N(e1/cm <sup>3</sup> )	N <sub>p</sub> (part/cm <sup>3</sup> )
487720.0	1718400.0	0.76684e 07	0.00000e 00
437720.0	1739800.0	0.93640e 07	0.00000e 00
387720.0	1762300.0	0.11620e 08	0.00000e 00
357720.0	1776500.0	0.13341e 08	0.00000e 00
327720.0	1791200.0	0.15426e 08	0.00000e 00
297720.0	1806500.0	0.17975e 08	0.00000e 00
267720.0	1822400.0	0.21118e 08	0.00000e 00
237720.0	1839000.0	0.25037e 08	0.00000e 00
207720.0	1856200.0	0.29977e 08	0.00000e 00
177720.0	1874200.0	0.36282e 08	0.00000e 00
147720.0	1893000.0	0.44434e 08	0.00000e 00
117720.0	1912700.0	0.55130e 08	0.00000e 00
87720.0	1933300.0	0.69391e 08	0.00000e 00
77720.0	1940400.0	0.75181e 08	0.00000e 00
67720.0	1947600.0	0.81603e 08	0.00000e 00
57720.0	1955000.0	0.88743e 08	0.00000e 00
47720.0	1962500.0	0.96696e 08	0.00000e 00
37720.0	1970100.0	0.15000e 09	0.00000e 00
27720.0	1959700.0	0.15309e 09	0.00000e 00
17720.0	1692900.0	0.17721e 09	0.00000e 00
16720.0	1659900.0	0.18074e 09	0.00000e 00
15720.0	1625200.0	0.18460e 09	0.00000e 00
14720.0	1588600.0	0.18385e 09	0.00000e 00
13720.0	1549700.0	0.19358e 09	0.00000e 00
12720.0	1508400.0	0.19889e 09	0.00000e 00
11720.0	1464100.0	0.20491e 09	0.00000e 00
10720.0	1416200.0	0.21183e 09	0.00000e 00
9720.0	1364000.0	0.21994e 09	0.00000e 00
8720.0	1306400.0	0.22964e 09	0.00000e 00
7720.0	1241800.0	0.24158e 09	0.00000e 00
6720.0	1167700.0	0.25691e 09	0.00000e 00
5720.0	1080000.0	0.27779e 09	0.00000e 00
4720.0	970070.0	0.30926e 09	0.00000e 00
3720.0	816610.0	0.36737e 09	0.00000e 00
2720.0	503800.0	0.59548e 09	0.00000e 00
2620.0	428270.0	0.70049e 09	0.00000e 00
2520.0	286250.0	0.10480e 10	0.00000e 00
2510.0	257990.0	0.11628e 10	0.00000e 00
2500.0	219070.0	0.13694e 10	0.00000e 00
2495.0	190820.0	0.15722e 10	0.00000e 00
2490.0	145250.0	0.20654e 10	0.00000e 00
2489.0	130290.0	0.23025e 10	0.00000e 00
2488.0	109290.0	0.27450e 10	0.00000e 00
2487.0	65000.0	0.69420e 10	0.99942e 06
2485.0	45000.0	0.97000e 10	0.59965e 07
2484.0	34000.0	0.12390e 11	0.39997e 08
2483.0	27000.0	0.14920e 11	0.21000e 09
2482.0	24000.0	0.15770e 11	0.52000e 09
2481.0	22500.0	0.15790e 11	0.83000e 09

MODEL SOLAR ATMOSPHERE USED IN OUR COMPUTATIONS

HT(km)	T(°K)	N(e1/cm <sup>3</sup> )	N <sub>n</sub> (part/cm <sup>3</sup> )
2480.0	22000.0	0.15820e 11	0.96000e 09
2465.0	21000.0	0.16420e 11	0.10200e 10
2445.0	20600.0	0.17090e 11	0.97000e 09
2415.0	20400.0	0.17830e 11	0.94000e 09
2375.0	20300.0	0.18660e 11	0.97000e 09
2315.0	20200.0	0.19670e 11	0.11600e 10
2305.0	19800.0	0.20110e 11	0.13900e 10
2302.0	16000.0	0.22670e 11	0.33700e 10
2298.0	13000.0	0.25020e 11	0.63600e 10
2295.0	8800.0	0.28990e 11	0.13930e 11
2282.0	8550.0	0.28360e 11	0.17760e 11
2268.0	8300.0	0.27600e 11	0.21880e 11
2235.0	7800.0	0.26260e 11	0.32230e 11
2170.0	7300.0	0.24590e 11	0.52880e 11
2095.0	6940.0	0.22970e 11	0.84160e 11
2030.0	6720.0	0.21840e 11	0.12207e 12
1945.0	6620.0	0.22210e 11	0.18554e 12
1810.0	6560.0	0.25280e 11	0.35890e 12
1690.0	6500.0	0.29320e 11	0.66508e 12
1560.0	6440.0	0.37480e 11	0.13526e 13
1430.0	6390.0	0.51500e 11	0.28774e 13
1280.0	6330.0	0.79380e 11	0.72643e 13
1170.0	6230.0	0.10550e 12	0.14850e 14
1030.0	5930.0	0.12690e 12	0.39885e 14
980.0	5760.0	0.12180e 12	0.58694e 14
930.0	5560.0	0.11060e 12	0.88170e 14
880.0	5360.0	0.97280e 11	0.13413e 15
830.0	5150.0	0.85560e 11	0.20715e 15
780.0	4890.0	0.77910e 11	0.32997e 15
730.0	4600.0	0.84240e 11	0.54269e 15
680.0	4350.0	0.11220e 12	0.91350e 15
630.0	4170.0	0.16150e 12	0.15560e 16
605.0	4150.0	0.19610e 12	0.20060e 16
580.0	4150.0	0.24100e 12	0.25760e 16
530.0	4200.0	0.37540e 12	0.41870e 16
480.0	4350.0	0.61510e 12	0.65730e 16
430.0	4500.0	0.99040e 12	0.10160e 17
380.0	4640.0	0.15620e 13	0.15540e 17
330.0	4780.0	0.24310e 13	0.23460e 17
280.0	4930.0	0.37610e 13	0.34940e 17
230.0	5100.0	0.58460e 13	0.51170e 17
180.0	5370.0	0.96450e 13	0.72439e 17
130.0	5750.0	0.18980e 14	0.98574e 17
100.0	6070.0	0.34850e 14	0.11548e 18
80.0	6300.0	0.55110e 14	0.12736e 18
65.0	6600.0	0.95490e 14	0.13403e 18
50.0	7100.0	0.22090e 15	0.13641e 18
30.0	8000.0	0.80400e 15	0.13433e 18
0.0	9000.0	0.26010e 16	0.13495e 18

APPENDIX II  
RAY TRACING PROGRAM

```

/load fortgl,nsegs=6
/parm deck
/job nogo
c
cccc program "solmfw" cccccccccccccccccccccccccccccccccccccccccccccc
c
dimension dh(200),h(200),t(200),cr(200),dtau(200),crm(21),
1 ar(200),br(200),dr(200),bt(21),btq(21),spec(21)
integer r,rmml,s,com(40),rcrm(21),rm,ocr(51),r1,r2,r3,r1pl,
1 r2pl,r3pl,p,q,rmpl,pp1,pp2,rml,rt,r3ml,r4,r4ml,r0,
2 r0pl,rlm3
real l(21),nu(21),nn(200),mu2(200),lnu,ne(200),htel(21),
1 hcr1(21),hcr2(21),nue(200),nuep(200),nuen(200),
2 tq(200),neq(200),ro2(200),hr(21),tauref(21),the(200),
3 theinf(21),er(200),xr(200),nnq(200),hq(200)
logical qflag/.false./,aflg/.false./
integer*4 gtitl(15)
c
rm=181
c
rm = no. of levels in the solar atmosphere.
rmpl=rm+1
rmml=rm-1
xc=2.9979e10
c
xc= speed of light (cm/s).
rsun=6.9599e5
c
rsun = radius of the sun (km).
pi=3.1415927
c
pi = that's right, pi.
crd=180.0/pi
c
crd = conversion of radians to degrees.
x5=1.0e5
c
x5 = number of cm/km.
xkfc=1.1e-6
c
xkfc = constant for computing conductive flux.
xb3=3.18260e9
c
xb3 = constant for computing the plasma frequency.
c
do 14 i=1,51
14 ocr(i)=0
do 71 i=4,36,4
71 ocr(i+1)=i/4
ocr(41)=1
x9=1.0e-9
c
c
cccc input wavelengths, aimpar, spectrum, and region limits ccccccccccc
read (5,*) im
c
c
c im is the number of wavelengths that are to be processed
c
do 16 i=1,im

```

```

16      read (5,617) l(i)
617     format (3f10.0)
c      l(i) = wavelength (cm).
c      im = number of wavelengths to process.
301     read (5,602,end=998) aimpar,spec
602     format (f7.0,21f3.2)
       read (5,851)gtitl
851     format(15a4)
       aflg=.false.
c      spec(i) = coronal hole spectrum.
       d2=aimpar*aimpar
       read (5,611) r0,r1,r2,r3,lp,alfa0,alfal,alfa2,alfa3,beta0,
1         betal,beta2,beta3,gamma
611     format(5i5,9f6.0)
c
cccc   input the quiet sun model  cccccccccccccccccccccccccccccccccccccccccc
c
       if(qflag)go to 302
       read (5,601) (com(i),i=1,40)
       qflag=.true.
601     format (40a2)
c
       do 1 r=1,rm
       read (5,600,end=998) hq(r),tq(r),neq(r),nnq(r)
600     format (f8.0,f10.0,e12.0,e11.0)
c      hq(r) = altitude of layer r (km).
c      tq(r) = temperature in layer r (k).
c      neq(r)= # electrons per cm**3
c      nnq(r)= # neutral atoms per cm**3.
1       continue
c
302     alfa0=1.0
       alfa1=1.0
       alfa2=1.0
       alfa3=1.0
       beta0=1.0
       betal=1.0
       beta2=1.0
       beta3=1.0
       zeta0=1.0
       zetal=1.0
       zeta2=1.0
       zeta3=1.0
       gamma=1.0
       lcount=0
       the(rmpl)=crd*arsin(aimpar*rsun/(h(rmpl)+rsun))
c
cccc   modify the quiet sun model  cccccccccccccccccccccccccccccccccccccccccc
c
7       r0pl=r0+1
       r1pl=r1+1
       r2pl=r2+1
       r3pl=r3+1
       r3ml=r3-1
       r4=r3-2

```

```

r4m1=r4-1
r1m3=r1-3
do 9 r=1,r0
  t(r)=tq(r)
  ne(r)=neq(r)
c
  tp=tq(r0)
  do 6 r=r0p1,r1
    t(r)=tp+beta0*(tq(r)-tp)
    ne(r)=neq(r)*alfa0
c
  tp=tq(r0)
  do 8 r=r1p1,r2
    t(r)=tp+beta1*(tq(r)-tp)
    if (t(r).gt.tq(r2)) t(r)=tq(r2)
    ne(r)=neq(r)*alfa1
c
  tp=t(r2)
  do 19 r=r3,rm
    t(r)=tp+beta3*(tq(r)-tp)
    ne(r)=neq(r)*alfa3
    t(rmpl)=t(rm)
c
  tp=t(r2)
  do 17 r=r2p1,r3m1
    t(r)=tp+beta2*(tq(r)-tp)
    ne(r)=neq(r)*alfa2
c
c
c   recompute the altitude of each level
c   this also changes the gradients in each region
c
do 900 r=1,r0
900 h(r)=hq(r)
   h1=hq(r0)
   do 901 r=r0p1,r1
     h(r)=h1+zeta0*(hq(r)-hq(r-1))
901 h1=h(r)
   do 902 r=r1p1,r2
     h(r)=h1+zeta1*(hq(r)-hq(r-1))
902 h1=h(r)
   do 903 r=r2p1,r3m1
     h(r)=h1+zeta2*(hq(r)-hq(r-1))
903 h1=h(r)
   do 904 r=r3,rm
     h(r)=h1+zeta3*(hq(r)-hq(r-1))
904 h1=h(r)
   do 905 r=1,rm
     x=(rsun+h(r))/rsun
     ro2(r)=x*x
905 continue
c
do 2 r=2,rmml
2 dh(r)=(h(r+1)-h(r-1))*0.5
  dh(1)=h(2)-h(1)
```

```

c      dh(rm)=h(rm)-h(rmml)
c      dh(r)= shell thickness (km).
c      h(rmpl)=h(rm)+0.5*dh(rm)
c
c      match the electron density at r4==>r3.
c      s3=(ne(r3pl)-ne(r3))/(h(r3pl)-h(r3))
c      do 23 r=r2pl,r3
c      nep=ne(r3)+s3*(h(r)-h(r3))
c      if (ne(r).ge.nep) go to 23
c      ne(r)=nep
23    continue
c
c      match the temperature at r4==>r3.
c      s4=(t(r3)-t(r4))/(h(r3)-h(r4))
c      do 29 r=r4,r3
29    t(r)=t(r4)+s4*(h(r)-h(r4))
c
c      match the electron density at r=rlm3==>rl+1.
c      s1=(ne(rlpl)-ne(rlm3))/(h(rlpl)-h(rlm3))
c      do 26 r=rlm3,rlpl
26    ne(r)=ne(rlm3)+s1*(h(r)-h(rlm3))
c
c      do 11 r=1,rm
c      gam=gamma
c      if (gam.eq.1.00) go to 11
c      if (nnq(r).le.0.0) go to 11
c      alfae=ne(r)/neq(r)
c      betae=tq(r)/t(r)
c      betae is inverted!
c      gammax=betae+(2.0*neq(r)/nnq(r))*(betae-alfae)
c      if (gamma.gt.gammax) gam=gammax
11    nn(r)=nnq(r)*gam
c
cccc electron collision frequencies cccccccccccccccccccccccccccccccccccccc
c
c      nicolet, m. (1953), "the collision frequency of electrons in the
c      ionosphere", journal of atmospheric and terrestrial physics,
c      vol. 3, pp. 200-211.
c
c      constants for collisions with neutrals.
21    xkn=2.6022e6
c      sig=2.0e-8
c      sig = collision distance for electrons with neutrals (cm).
c      sig2=sig*sig
c      constants for collisions with positive ions.
c      x32=(-3.0/2.0)
c      x23=(-2.0/3.0)
c      xbl=1.81668
c      xk4=5.72965e6
c
c      do 15 r=1,rm
c      nuen(r)=xkn*nn(r)*sig2*sqrt(t(r))
c      nuen(r) = collision frequency between electrons and neutrals.
c
c      al2=alog(1.0+(xk4*t(r)*t(r)*(2.0*ne(r))**x23))

```

```

nuep(r)=xbl*al2*ne(r)*(t(r)**x32)
c   nuep(r) = collision frequency between electrons and protons.
c
15  nue(r)=nuep(r)+nuen(r)
c   nue(r) = electron collision frequency.
c
cccc output the model ccccccccccccccccccccccccccccccccccccccccccccccccccccccc
c
    if(lp.eq.-1)go to 311
    write(11,616)(com(j),j=1,40),r0,alfa0,beta0,zeta0,r1,alfal,
1   betal,zetal,r2,alfa2,beta2,zeta2,r3,alfa3,beta3,zeta3,
2   gamma,aimpar
    write(11,603)
603  format (          105h      r      h      dh      t      ne
1   nn      nue      nuep      nuen      ratio      f      p*p/f/3x
2,102h (-)      (km)      (km)      (k)      (cm**-3)      (cm**-3)      (hz)
3 (hz)      (hz)      c/s*cm*cm      /)
c
311  do 22 r=2,rm
    ratio=nuen(r)/nuep(r)
    fcond=xkfc*t(r)*t(r)*sqrt(t(r))*(t(r+1)-t(r-1))/(h(r+1)-h(r-1))
    fcond=1.00
    p2of=ne(r)*t(r)*ne(r)*t(r)/fcond
    alfae=ne(r)/neq(r)
    betae=t(r)/tq(r)
    if(lp.eq.-1)go to 22
    write(11,604) r,h(r),dh(r),t(r),ne(r),nn(r),nue(r),nuep(r),
1   nuen(r),ratio,fcond,p2of,alfae,betae
604  format (i6,f8.0,f8.1,f9.0,1p5e10.3,5e9.2)
    if (r.eq.rl.or.r.eq.r2.or.r.eq.r3.or.r.eq.r0) write(11,615)
615  format (1x,13(10h. . . . .))
    22  continue
c
cccc optical depth and contribution function routines ccccccccccccccccccc
c
cccc initialize variables.
    do 5 i=1,im
    nu(i)=xc/l(i)
c   nu(i) = frequency corresponding to l(i) (hz).
    bt(i)=0.0
    htel(i)=0.0
    hcr1(i)=0.0
    hcr2(i)=0.0
    rcrm(i)=1
    5   crm(i)=0.0
c
cc
cccc wavelength loop.
cc
c
    do 999 i=1,im
    lnu=alog(nu(i))
c
    if (l(i).ge.0.050) go to 13

```

```

write (6,607) (com(j),j=1,40),1(i)
write (6,613)
613 format (5x, 57hthe reyleigh-jeans approximation is used in this p
rogram./5x, 72hthis makes computations at wavelengths less than 0.
2050 cm inappropriate.)
go to 999
c
cccc compute dtau for each layer and locate the turning-point level.
13 ltl=1(i)*1(i)
om=2.0*pi*nu(i)
om2=om*om
mu2(rmpl)=1.00
p=0
c
do 10 j=1,rm
r=rmpl-j
omo2=xb3*ne(r)
yp=om2+nue(r)*nue(r)
xmf=1.00-(omo2/yp)
xnf=nue(r)*omo2/(om*yp)
ypp=(xnf*xnf)/(xmf*xmf)
chi2=0.25*xnf*ypp*(1.0-0.25*ypp)
mu2(r)=xmf+chi2
if (mu2(r).le.0.00) go to 60
c if (mu**2.le.0.00) the wave is reflected.
zi=1.00-(d2/(mu2(r)*ro2(r)))
if (zi.le.0.00) go to 60
c if (zi.le.0.00) the turning-point has been reached.
dtau(r)=2.0*sqrt(chi2)*om*x5*dh(r)/(xc*sqrt(zi))
if (dtau(r)-175.0) 25,24,24
24 ar(r)=1.00
go to 10
25 ar(r)=1.00-exp(-dtau(r))
10 continue
go to 61
60 p=r
c p = pointer to the level which reflects the radio wave.
c
cccc compute optical depths of direct and reflected rays.
61 ppl=p+1
dr(rmpl)=0.00
dtau(rmpl)=0.00
jt=rmpl-p
do 30 j=1,jt
r=rmpl-j
rpl=r+1
30 dr(r)=dr(rpl)+dtau(rpl)
c dr(r) = optical depth of level r (direct ray).
62 pp2=p+2
do 27 r=pp2,rm
er(r)=dr(p)
rml=r-1
do 27 q=ppl,rml
27 er(r)=er(r)+dtau(q)
c er(r) = optical depth of level r (reflected ray).

```



```

er(ppl)=dr(p)
tauref(i)=dr(p)
c   tauref(i) = optical depth of turning-point.
c
cccc compute contribution from each level.
do 32 r=ppl,rm
  br(r)=0.0
  if (dr(r)-175.0) 31,28,28
31  br(r)=br(r)+exp(-dr(r))
28  if (er(r)-175.0) 36,32,32
36  br(r)=br(r)+exp(-er(r))
32  xr(r)=t(r)*ar(r)*br(r)
c   xr(r) = contribution from level r (k).
c
cccc find the brig. temp., the peak of the cont. fn. and its location.
do 40 r=ppl,rm
  cr(r)=xr(r)/dh(r)
c   cr(r) = contribution function (k/km at level r).
  if (crm(i)-cr(r)) 33,40,40
33  crm(i)=cr(r)
c   crm(i) = maximum value of cr(r).
  rcrm(i)=r
c   rcrm(i) = location of the peak value of cr(r).
40  bt(i)=bt(i)+xr(r)
c   bt(i) = brightness temperature at wavelength l(i) (k).
c
cccc normalize the contribution and the contribution function.
c
  if (crm(i).eq.0.00) go to 72
  xa=1.0/crm(i)
  do 41 r=ppl,rm
41  cr(r)=cr(r)*xa
c   cr(r) is now the normalized contribution function.
c
72  xa=0.0
  do 69 r=ppl,rm
  if (xa-xr(r)) 63,69,69
63  xa=xr(r)
69  continue
c
  if (xa.eq.0.00) go to 73
  xa=1.0/xa
  do 67 r=ppl,rm
67  xr(r)=xr(r)*xa
c
cccc define variables for output.
73  ar(rmpl)=0.00
    br(rmpl)=1.00
    cr(rmpl)=0.00
    er(rmpl)=0.00
    xr(rmpl)=0.00
    dtau(p)=0.0
    ar(p)=0.00
    br(p)=0.00
    cr(p)=0.00

```

```

      cr(p)=0.00
      xr(p)=0.00
      the(p)=0.0
      hr(i)=h(p)
c      hr(i) = height of reflection level.
c
cccc  compute theta at each layer.
      y=a1mpar*crd/rsun
      rt=rm+ppl
      do 70 j=ppl,rm
      r=rt-j
      x=y*dh(r)/sqrt(ro2(r)*(mu2(r)*ro2(r)-d2))
      the(r)=the(r+1)+x
70    continue
c      the(rapl) was defined above.
      theinf(i)=the(ppl)
c
cccc  determine the altitudes of the half power points of cr(r).
      if (crn(i).eq.0.00) go to 74
      j=rerm(i)
      jml=j-1
      do 46 r=p,jml
      s=j+p-1-r
      if (cr(s)-0.5) 43,47,46
46    continue
      her2(i)=(-999.0)
c      her2(i)=-999.0 means that the model does not go deep enough.
      go to 50
      74  her2(i)=(-388.0)
      herl(i)=(-388.0)
c      her2(i) = -388.0 means there is no contribution at this wavelength.
      go to 56
      47  her2(i)=h(s)
      go to 50
      43  r=s+1
      her2(i)=((0.5-cr(r))*(h(s)-h(r))/(cr(s)-cr(r)))+h(r)
c      her2(i) = lower half-power point of the cont. fn.
c
      50  if (j-rmml) 52,51,51
      51  herl(i)=(-999.0)
c      herl(i)=-999.0 means that the model does not go high enough.
      go to 56
      52  do 53 r=j,rmpl
      s=r
      if (cr(s)-0.5) 55,54,53
      53  continue
      herl(i)=(-999.0)
      go to 56
      54  herl(i)=h(s)
      go to 56
      55  r=s-1
      herl(i)=((0.5-cr(r))*(h(s)-h(r))/(cr(s)-cr(r)))+h(r)
c      herl(i) = upper half-power point of the cont. fn.
c
cccc  output contribution function for wavelength l(i)  ccccccccccccccccccc

```

```

c
56  if (lp.ne.1) go to 44
37  write(11,616)(com(j),j=1,40),r0,alfa0,beta0,zeta0,r1,alfal,
1  betal,zetal,r2,alfa2,beta2,zeta2,r3,alfa3,beta3,zeta3,
2  gamma,aimpar
   write (11,607) 1(i)
607  format (5x/16h wavelength =,f9.3,5h (cm),64x,25hcontribution f
      from level r//
1 130h r h crn mu**2 dtau ar dr er
2 br theta 0.0 0.2 0.4 0.6 0.8 1.
30 /
4 130h (-) (km) (k/km) (---) (--) (--) (--) (--)
5) (--) (deg) ^-----^-----^-----^-----^-----^-----^
6 /)

c
do 34 r=p,rmpl
kmax=xr(r)*40.0+1.001
if (kmax.gt.41) kmax=41
write (11,608) r,h(r),cr(r),mu2(r),dtau(r),ar(r),dr(r),er(r),
1 br(r),the(r),(ocr(k),k=1,kmax)
603 format (i5,f3.0,f7.4,f7.4,5e10.3,f7.2,2x,41i1)
if (r.eq.rl.or.r.eq.r2.or.r.eq.r3.or.r.eq.r0) write (11,615)
34 continue

c
cccc find the height at which tau equals unity.
44 rt=rm-p
do 39 r=1,rt
s=rm-r
if (dr(s)-1.0) 39,42,43
39 continue
htel(i)=(-999.0)
c htel(i) = -999.0 means tau=1 not reached above turning-point.
go to 999
42 htel(i)=h(s)
go to 999
43 r=s+1
htel(i)=((1.0-dr(r))*(h(s)-h(r))/(dr(s)-dr(r)))+h(r)
c htel(i) = height at tau=1 at wavelength 1(i) (km).
999 continue

c
cccc wavelength dependent parameters cccccccccccccccccccccccccccccccccccccccccc
c
if(lp.eq.-1)go to 312
write(11,616)(com(j),j=1,40),r0,alfa0,beta0,zeta0,r1,alfal,
1 betal,zetal,r2,alfa2,beta2,zeta2,r3,alfa3,beta3,zeta3,
2 gamma,aimpar
312 do 997 i=1,im
nu(i)=nu(i)*x9
s=rcrm(i)
lnu=alog10(1(i))
if(lp.eq.-1)go to 310
997 write (11,610) 1(i),nu(i),bt(i),lnu,h(s),htel(i),crm(i),hcr2(i),
1 hcr1(i),hr(i),tauref(i),theinf(i)
610 format (5x,14hwavelength =,0pf10.3,26h cm * frequency
1=, f9.3,25h ghz * brigt. temp. =, f10.0,7h k */

```

[illegible]

```

993 stop
    end
/inc spck
/data
/inc schspec

```

```

subroutine spectr(bt, btq, spec, xl, aflag, im, title)
integer title(15)
real*4 bt(21), btq(21), spec(21), xl(21)
real*4 qbt(23), llmda(23), pspec(23)
integer char/0/
logical aflag
write(6,99)
99 format('0      llmda', 5x, 'ratio')
do 10 i=1, im
  if(btq(i).eq.0.0) btq(i)=bt(i)
  qbt(i)=bt(i)/btq(i)*100.0
  llmda(i)=alog10(xl(i))
  write(6,100) llmda(i), qbt(i)
100 format(' ', 2f10.4)
  10 continue
  char=char+1
  if (char.le.13) go to 15
  aflag=.false.
  write(6,101)
101 format(' change plotter paper')
  15 call plots(0,0,15)
  call plot(1.0,1.0,-3)
  if(aflag) go to 50
  char=1
  call symbol(1.5,5.0,0.14,title,0.0,60)
  qbt(im+1)=20.0
  qbt(im+2)=20.0
  do 11 i=1, im
    pspec(i)=spec(i)*100.0
  11 if(pspec(i).eq.0.0) pspec(i)=100.
    pspec(im+1)=20.0
    pspec(im+2)=20.0
    call scale(llmda,9.0,im,1)
    call axis(0.0,0.0,10hlog(lmda),-10,9.0,0.0,llmda(im+1),
    llmda(im+2))
    call axis(0.0,0.0,28hbrightness temperature ratio,23,5.0,90.0,
    lpspec(im+1),pspec(im+2))
    call line(llmda,pspec,im,1,-1,0)
50 call line(llmda,qbt,im,1,-1,char)
    call plotf(0.0,0.0)
    return
end

```

Sample Input and Output at Computer Terminal

INPUT NEW PARAMETERS. TO ENTER A NEW SPECTRUM  
OK AIMING PARAMETER ENTER -1 FOR RO  
THE OLD PARAMETERS ARE: 31 43 48 60 -1 1.00 1.00 1.00 1.00  
1.00 1.00 1.00 1.00 1.00 1.00  
.15 43 48 60 -1 .8 .8 .16 .8 .7 .8 .45 .8 2.5 2 6 1 .8

RUSH BY PAPAGIANNIS & KUGUT (1975), AFGL-TR-75-0430, SEPT. 1975, PP. 18-19.

RO = 10, ALFA0 = 0.80, BETA0 = 0.90, ZETA0 = 2.50  
R1 = 43, ALFA1 = 0.80, BETA1 = 0.80, ZETA1 = 2.00  
R2 = 48, ALFA2 = 0.16, BETA2 = 0.45, ZETA2 = 6.00  
R3 = 60, ALFA3 = 0.80, BETA3 = 0.80, ZETA3 = 1.00  
GAMA = 0.8, AIM PAR = 0.700

LLMHA	RATIO
-0.1549	103.6982
-0.0655	103.7238
0.1399	100.6921
0.2856	94.8047
0.5309	83.6311
1.0507	76.6905
1.3304	65.0573
2.2718	81.6600
2.5740	103.4626

7 0 START OF TAPE

OPTIONSP.C

111E/V5VCTJPJN1V8(CSCHRPJPHCH1JJSWFPUPSPWS1414)DNOM5MKN5W5W1Z5~3~8\*EIG5GFI9X5Q5I  
, 0

INPUT NEW PARAMETERS. TO ENTER A NEW SPECTRUM

OK AIMING PARAMETER ENTER -1 FOR RO  
THE OLD PARAMETERS ARE: 16 43 48 60 -1 0.80 0.80 0.16 0.80  
0.90 0.80 0.45 0.80  
2.50 2.00 6.00 1.00 0.80

.-1 0 0 0 0 0 0 0 0 0 0 0 0 0 0  
\*60

END

DATE  
FILMED

9-81

DTIC